

## **General Disclaimer**

### **One or more of the Following Statements may affect this Document**

- This document has been reproduced from the best copy furnished by the organizational source. It is being released in the interest of making available as much information as possible.
- This document may contain data, which exceeds the sheet parameters. It was furnished in this condition by the organizational source and is the best copy available.
- This document may contain tone-on-tone or color graphs, charts and/or pictures, which have been reproduced in black and white.
- This document is paginated as submitted by the original source.
- Portions of this document are not fully legible due to the historical nature of some of the material. However, it is the best reproduction available from the original submission.

Nasa - CR - 168098

MRDC41054.59FR

Copy No. 93

# PREPARATION OF HIGH PURITY LOW DISLOCATION GaAs SINGLE CRYSTALS

FINAL REPORT FOR THE PERIOD  
December 29, 1980 through September 29, 1981

CONTRACT NO. NAS3-22224  
CONTRACT REPORT NUMBER 158098

Prepared for

USA-ETDL (ERADCOM)  
Fort Monmouth, N.J. 07703

and

NASA-Lewis Research Center  
Cleveland, Ohio 44135

D.E. Holmes  
Principal Investigator



FEBRUARY 1983



Rockwell International

(NASA-CR-168098) HIGH PURITY, LOW  
DISLOCATION GaAs SINGLE CRYSTALS Final  
Report, 29 Dec. 1980 - 29 Sep. 1981  
(Rockwell International Corp., Thousand  
Oaks) 113 p HC A06/MF A01

N83-19622

CSCL 20B H2/76

Unclas  
02960

ORIGINAL PAGE IS  
OF POOR QUALITY

Technical Report Documentation Page

1. Report No.	2. Government Accession No.	3. Recipient's Catalog No.	
4. Title and Subtitle  High Purity, Low Dislocation GaAs Single Crystals		5. Report Date February 1983	
		6. Performing Organization Code	
7. Author(s) R.T. Chen, D.E. Holmes, C.G. Kirkpatrick		8. Performing Organization Report No. MRDC41054.59FR	
9. Performing Organization Name and Address Rockwell International Microelectronics Research & Development Center 1049 Camino Dos Rios, Thousand Oaks, CA 91360		10. Work Unit No. (TRAIS)	
		11. Contract or Grant No. NAS3-22224	
12. Sponsoring Agency Name and Address Lewis Research Center Cleveland, Ohio 44135		13. Type of Report and Period Covered Final Report for the period 12/29/80 through 9/29/81	
		14. Sponsoring Agency Code 4231	
15. Supplementary Notes			
16. Abstract  Progress in LEC (liquid encapsulated Czochralski) crystal growth techniques for producing undoped, high resistivity, low dislocation material suitable for device applications is described. Technique development resulted in reduction of dislocation densities in 3-inch GaAs crystals. Control over the melt stoichiometry was determined to be of critical importance for the reduction of twinning and polycrystallinity during growth.			
17. Key Words  LEC, GaAs, Czochralski, high purity, dislocation density		18. Distribution Statement  Approved for public release; distribution unlimited.	
19. Security Classif. (of this report) Unclassified	20. Security Classif. (of this page) Unclassified	21. No. of Pages 108	22. Price

## TABLE OF CONTENTS

	<u>Page</u>
1.0 INTRODUCTION.....	1
2.0 MATERIALS SYNTHESIS AND GROWTH TECHNIQUES.....	4
2.1 Growth Configuration.....	4
2.2 Growth Process.....	4
3.0 CHARACTERIZATION TECHNIQUES.....	10
4.0 COMPENSATION MECHANISM OF SEMI-INSULATING LEC GaAs.....	11
4.1 Importance of Melt Stoichiometry.....	11
4.2 Chemical Impurities and Electrically Active Centers.....	17
5.0 REDUCTION OF DISLOCATION DENSITY.....	22
5.1 Cone Angle.....	22
5.2 B <sub>2</sub> O <sub>3</sub> Thickness.....	24
5.3 Ambient Pressure.....	27
6.0 REDUCED INCIDENCE OF TWINNING.....	28
7.0 APPLICATION OF LEC GaAs IN DEVICE FABRICATION.....	30
8.0 SUMMARY.....	36
9.0 APPENDICES.....	37
9.1 Appendix I	
9.2 Appendix II	
9.3 Appendix III	
9.4 Appendix IV	





# LIST OF FIGURES

	<u>Page</u>
Fig. 1 Photographs of undoped LEC GaAs Crystals grown as part of the Add-on program: (a) R21/M, (b) R24/M, (c) R30/M, (d) R33/M, (e) R34/M, and (f) R39/M.....	3
Fig. 2 Cross section of the crucible for the LEC Growth system, showing the location of the B <sub>2</sub> O <sub>3</sub> during growth.....	5
Fig. 3 Cross section of the LEC crucible before growth showing the charge of elemental Ga and As and the preformed B <sub>2</sub> O <sub>3</sub> disc.....	6
Fig. 4 Dependence of electrical resistivity of LEC GaAs on melt stoichiometry. Semi-insulating material is obtained above, and p-type (low resistivity) material below a critical melt composition of about 0.475 atom fraction.....	12
Fig. 5 Resistivity profiles for LEC GaAs crystals grown from Ga-rich and As-rich melts.....	15
Fig. 6 Typical optical absorption spectrum of GaAs containing EL2.....	19
Fig. 7 Temperature-corrected electron concentration - temperature curve of undoped semi-insulating GaAs giving activation energy of the free carriers.....	20
Fig. 8 Dependence of EL2 concentration as determined by optical absorption on the melt stoichiometry. The concentration of EL2 increases from $5 \times 10^{15} \text{ cm}^{-3}$ to $1.7 \times 10^{16} \text{ cm}^{-3}$ as the As atom fraction increases from about 0.48 to 0.51, and appears to saturate as the As concentration increases further to 0.53.....	21
Fig. 9 Radial dislocation density profiles across wafers obtained from the front, middle, and tail of a crystal. The radial profiles are "W"-shaped and the average EPD increases from the front to the tail.....	25
Fig. 10 Photograph of RAM processed on LEC GaAs.....	31
Fig. 11 (a-d) Depletion voltage maps of NASA-Army crystals for 320 keV Se implanted through 750A Si <sub>3</sub> N <sub>4</sub> to a dose of $2.5 \text{ E12/cm}^2$ .....	32
Fig. 12 Pinchoff voltage maps of FET arrays fabricated on NASA-Army crystal R34.....	33



LIST OF TABLES

	<u>Page</u>
Table 1 Growth Parameters and Physical Properties of NASA-Army Crystals.....	7
Table 2 Dependence of As Weight Loss on Heating Rate During Heat-up Cycle.....	9
Table 3 Summary of Techniques Used to Characterize LEC GaAs.....	10
Table 4 Electrical Characteristics of NASA-Army Crystals.....	13
Table 5 Melt Stoichiometry Corresponding to the Growth of Front and Tail of NASA-Army Crystals.....	14
Table 6 Detailed Resistivity Profiles and Stoichiometry of NASA-Army Crystals R21 and R24.....	16
Table 7 Impurity Analysis of NASA-Army Crystals.....	18
Table 8 Dislocation Density and Distribution in NASA-Army Crystals.....	23
Table 9 Effect of B <sub>2</sub> O <sub>3</sub> Height on Dislocation Density.....	26
Table 10 Incidence of Twinning in Large-Diameter (100) LEC GaAs Crystals.....	29
Table 11 Summary of Studies of Depletion Voltage Uniformity Across 3-Inch Wafers (C-V).....	34
Table 12 Pinchoff Voltage of FET Arrays on Simultaneously Processed 1-Inch Wafers from NASA-Army Crystal R34.....	34
Table 13 Yield of Five 9-Stage Ring Oscillators Fabricated on NASA-Army Crystal R34.....	35



## 1.0 INTRODUCTION

This report summarizes the results obtained on the NASA-ARMY Add-on to the "Preparation of High Purity Low Dislocation Density GaAs Single Crystals" program (NAS3-22224). The primary goal of the add-on program was to increase the scope of the original program to determine the materials synthesis and growth conditions necessary to produce high purity low dislocation GaAs by the liquid encapsulated Czochralski (LEC) technique. Attention was focussed on two principal areas. First, the initial study of crystal growth parameters that control the dislocation density in large-diameter (3-inch) crystals was expanded. Low dislocation densities are particularly important for solar cell applications requiring high performance and radiation hardness. Second, the predominant chemical impurities and electrically active centers in undoped LEC material and their influence on the electrical compensation were evaluated.

Three important accomplishments have been achieved in our laboratory as a result of research conducted through the NASA-Army and our IR&D programs. First, and most important, a crystal growth process was developed for producing semi-insulating GaAs with a demonstrated high yield of device-quality material. This process involves the control of the melt stoichiometry on the As side of the stoichiometric composition. Evaluation of the material grown by this process showed that the semi-insulating properties are uniform, and thermally stable during device processing. LEC GaAs wafers have been successfully used at Rockwell-MRDC to fabricate integrated circuit devices such as RAMs, multipliers, and synthesizers. The implementation of this crystal growth process and the use of the resulting GaAs has had considerable impact on the development of GaAs integrated circuit technology. Rockwell-MRDC is the first laboratory to upgrade the device fabrication line to process 3-inch GaAs wafers as a result of this work.

Second, studies of the structural perfection of LEC GaAs crystals in this program have led to an additional 10% reduction in the dislocation density compared to the results achieved during the first phase of the program. Reduced dislocation densities were found to be favored by the use of

thick  $B_2O_3$  layers, low ambient pressures, and controlled melt stoichiometry. By controlling the appropriate crystal growth parameters, the most structurally perfect 3-inch-diameter LEC GaAs crystals yet reported were produced in this laboratory.

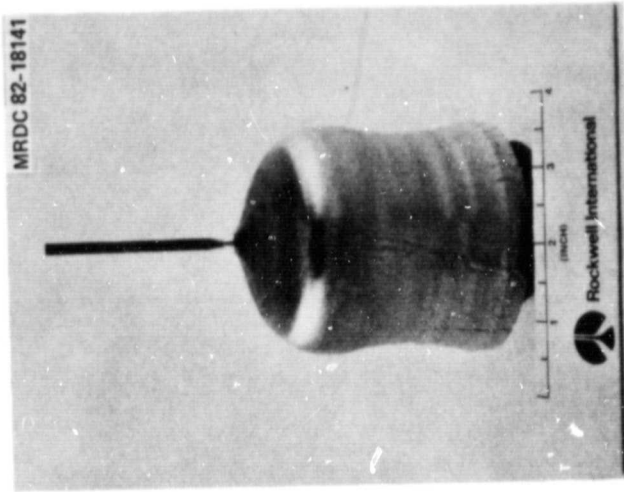
Finally, it was found that the control over the melt stoichiometry is also essential in reducing the frequency of twinning and polycrystallinity during crystal growth. This understanding dramatically increased the yield of single (100) GaAs crystals required for device fabrication.

Six crystals were grown as a part of the NASA-Army program (Fig. 1). Two of these crystals (R30 and R39) were delivered as whole single crystals to Mr. Thomas AuCoin in fulfillment of the contract obligations. The four remaining crystals (R21, R24, R33, and R34) were sliced into wafers. Four polished wafers each from the front and tail of each of these four crystals were also delivered to Mr. AuCoin. Other wafers were characterized using various destructive and nondestructive techniques such as secondary ion mass spectrometry, Hall effect measurements, and preferential etching. In addition, a number of these semi-insulating substrates were processed into IC devices for the experimental evaluation of cause-effect relationships between substrate properties, device processing, and device performance.

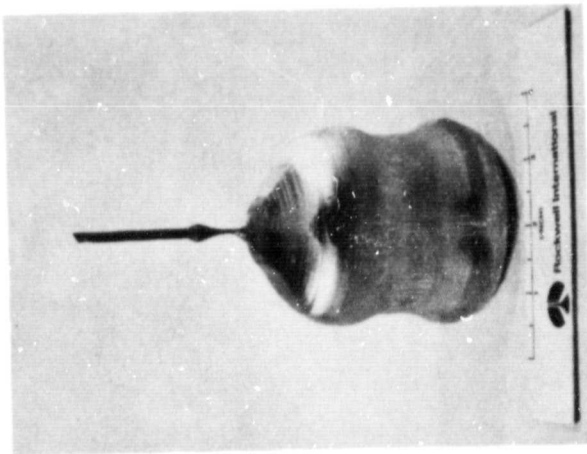
The organization of the report is as follows. In the second section, the materials synthesis and growth techniques used to produce the crystals are described, with emphasis on new procedures used and new knowledge gained since the original program. Various techniques used to characterize the material are described in the third section. The central results concerning the compensation mechanism and dislocation studies, are described in the fourth, and fifth sections, respectively. The sixth section describes the use of these semi-insulating materials in device fabrication.



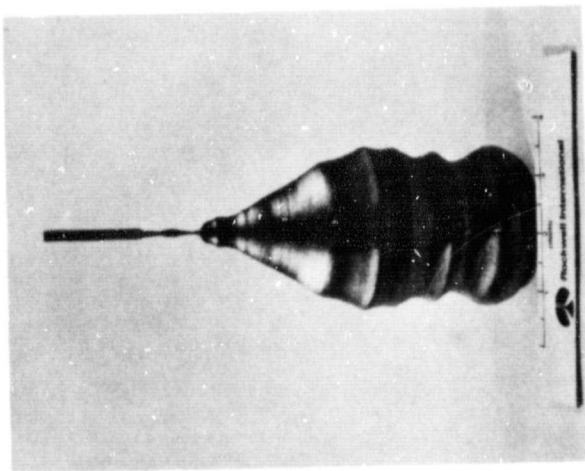
ORIGINAL PAGE  
BLACK AND WHITE PHOTOGRAPH



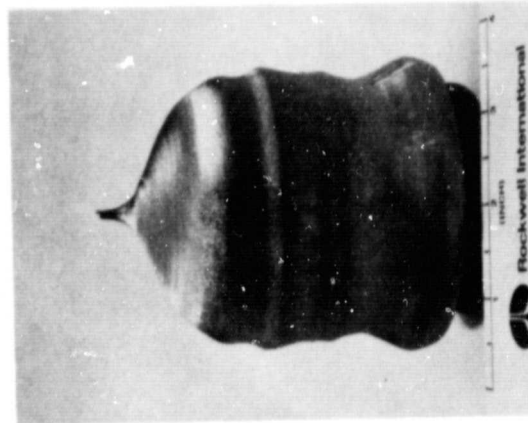
(a)



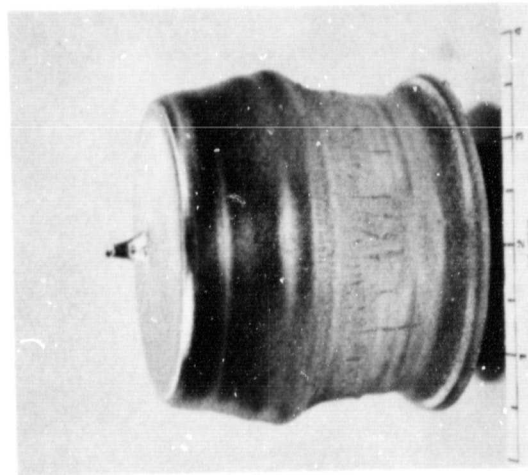
(b)



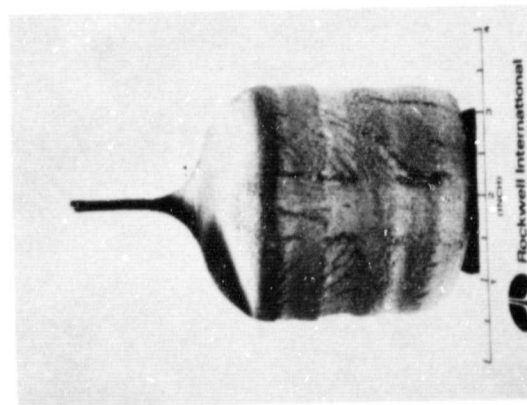
(c)



(d)



(e)



(f)

Fig. 1 Photographs of undoped LEC GaAs crystals grown as part of the Add-on program: (a) R21/M, (b) R24/M, (c) R30/M, (d) R33/M, (e) R34/M, and (f) R39/M.



## 2.0 MATERIALS SYNTHESIS AND GROWTH TECHNIQUES

In this section, the processes involved in materials synthesis and growth of LEC GaAs are described.

### 2.1 Growth Configuration

All crystals were grown in Rockwell International's Melbourn high-pressure LEC system at the Thousand Oaks MRDC laboratory. The configuration of the LEC system, shown schematically in Fig. 2, consisted of a GaAs melt contained in a high purity pyrolytic boron nitride (Union Carbide) crucible. The boric oxide ( $B_2O_3$ ) encapsulant floats on the top surface of the melt. In addition, a thin film of  $B_2O_3$  coats the entire surface of the crucible due to the high temperature wetting characteristics of this material. The  $B_2O_3$  also wets the growing crystal. Thus, the GaAs melt is completely sealed, suppressing As evaporation and shielding the melt against contamination from the crucible and the growth ambient.

### 2.2 Growth Process

The major steps in the crystal growth operation included loading of the charge, heat up, synthesis, equilibration, seeding, necking, cone growth, and pulling of the full diameter ingot. The crucible was loaded with approximately 1400 g 6-9's Ga (Ingal International), 1500 g 6-9's As (Cominco), and a 500 g pre-formed  $B_2O_3$  disk (Puratronic) with a known moisture content, as shown in Fig. 3. Solid Ga, which is solid to just above room temperature, was loaded on top of the As so that the liquid Ga served to encapsulate the As. Starting with a chamber pressure of 600 psi, the crucible was heated to between 450 and 500°C, at which point the  $B_2O_3$  melted, flowed over the charge of Ga and As, and sealed at the crucible wall. The synthesis reaction ( $Ga_{liquid} + As_{solid} = GaAs_{solid}$ ) occurred at about 800°C. The presence of the  $B_2O_3$  and the use of high overpressures (~1000 psi) prevented significant loss of As due to sublimation and evaporation during and subsequent to synthesis. The melt was then equilibrated at the starting temperature and the growth procedure begun.



ORIGINAL PAGE IS  
OF POOR QUALITY

MRDC81-11822

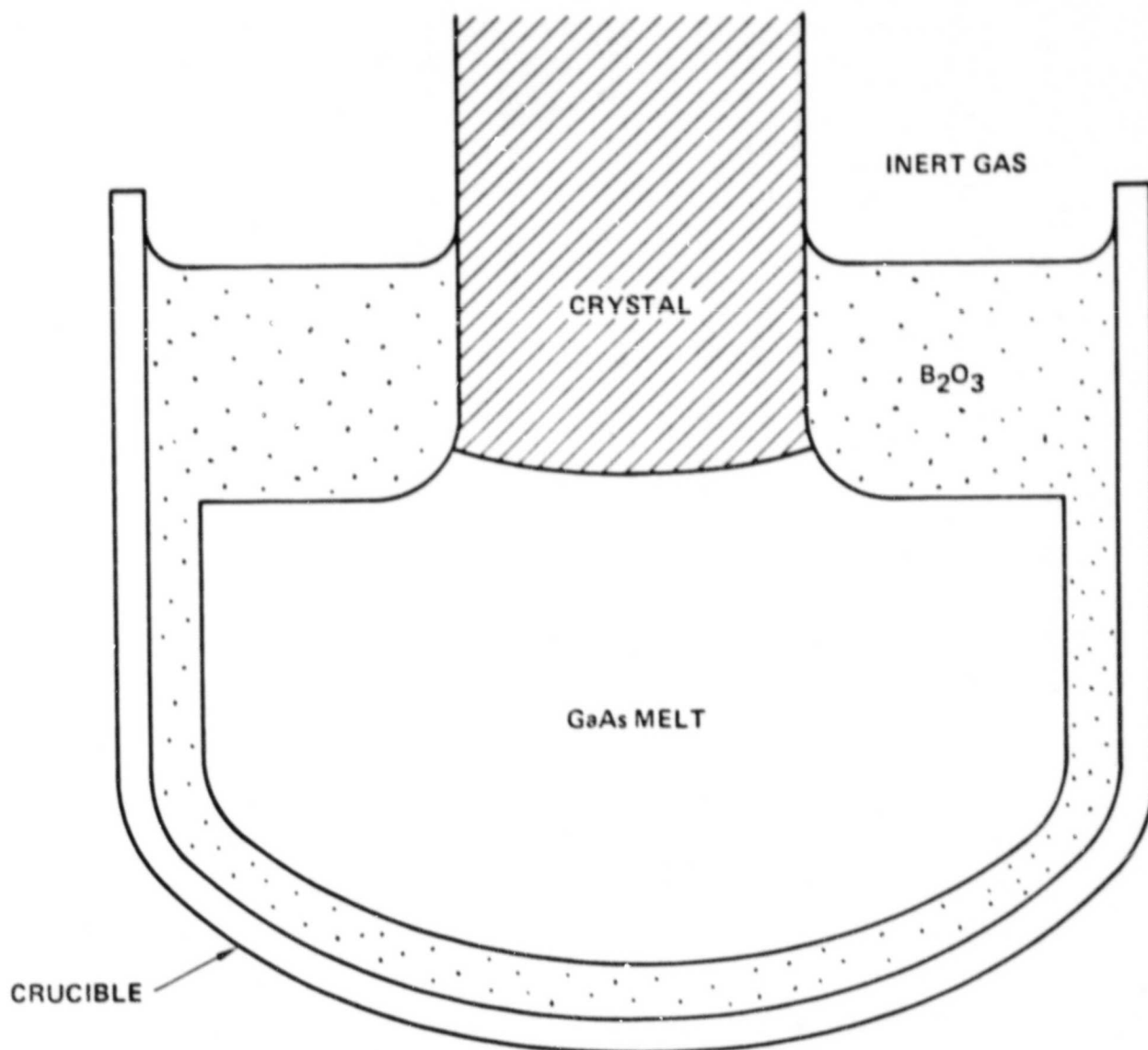


Fig. 2 Cross section of the crucible for the LEC Growth system, showing the location of the B<sub>2</sub>O<sub>3</sub> during growth.



ORIGINAL PAGE IS  
OF POOR QUALITY

MRDC 81-14942

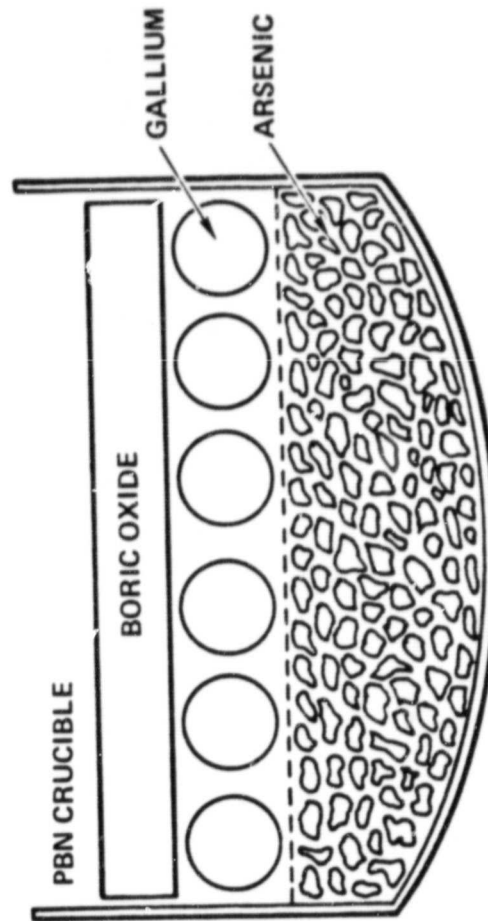


Fig. 3 Cross section of the LEC crucible before growth showing the charge of elemental Ga and As and the preformed  $B_2O_3$  at  $2000^\circ C$ .



Growth was initiated by dipping the seed, which was held on the pull shaft, through the  $B_2O_3$  and into the melt. The crystal was grown by gradually withdrawing the seed from the melt. The diameter was gradually and controllably increased to full dimension. The seed and the crucible were rotated in the same direction at 6 and 15 rpm, respectively.

The growth parameters and physical properties of the NASA-Army crystals are given in Table 1.

Table 1. Growth Parameters and Physical Properties of NASA-Army Crystals

Crystal No.	Crucible Material	$B_2O_3$ Water Content, ppm	Growth Direction	Weight (kg)	Diameter (mm)
R21	PBN	495	<100>	2.2	$71.1 \pm 7.1$
R24	"	170	"	2.3	$82.4 \pm 5.5$
R30	"	170	"	2.4	$81.3 \pm 3.0$
R33	"	160	"	2.1	See text
R34	"	304	"	2.4	$87.5 \pm 6.3$
R39	"	335	"	2.5	$84.5 \pm 2.6$

As will be discussed later in this report, control over the melt stoichiometry is essential to achieve reproducible growth of undoped semi-insulating LEC GaAs. An important element of the pre-growth process is method by which the charge of elemental Ga and As is heated from room temperature to the melting point of GaAs. In the earlier experiments with PBN crucibles it was found that significantly more As was lost from PBN crucibles compared to quartz crucibles during the heat up cycle. The typical weight loss from a 3000 gram charge contained in a quartz crucible ranged from 10 to 20 grams, or less than 1%. The composition of the charge could effectively be controlled under these circumstances. On the other hand, the As weight loss from PBN crucibles could be several times the loss factor of quartz crucibles, leading



to significant variations in melt stoichiometry as a crystal was pulled from the melt. (The weight loss was determined by comparing the weight of the initial charge to the weight of the crystal and the charge remaining in the crucible after growth.)

Initially, the difference in behavior between the two crucibles was believed to be a result of the different heat-transfer characteristics of the two materials; the higher heat transfer of the PBN at lower temperatures (<600°C) would lead to premature heating of the As before the  $B_2O_3$  had completely melted. For this reason, a number of experiments were conducted at the beginning of this program in which the heating rate was reduced to allow sufficient time for the  $B_2O_3$  to melt. The dependence of the weight loss on heating rate in experiments 21, 24 and 30 are given in Table 2. The results show that the weight loss increases as the heating rate decreases, which is opposite to the expected behavior based on the original model for the weight loss. Therefore, it was concluded that the difference between the crucibles is not the heat-transfer characteristics, but rather, the wetting characteristics of the  $B_2O_3$ . Since quartz is an (ionic) oxide, whereas PBN is a (covalent) semiconductor, different wetting characteristics for  $B_2O_3$  the two materials are to be expected. The weight loss decreases as the heating rate increases because the wetting to the PBN is improved at higher temperatures, allowing the  $B_2O_3$  to seal before significant amounts of As are lost. Using high heating rates in combination with additions of either excess As or Ga in the initial charge, we can now routinely produce near-stoichiometric 3 kg melts with the desired composition offset (either As-rich or Ga-rich) with respect to the stoichiometric composition.

**Table 2. Dependence of As Weight Loss on Heating Rate During Heat-up cycle**

Crystal No.	Average Heating Rate, ( $^{\circ}\text{C hr}^{-1}$ )	Weight Loss (grams)
R21	145	140
R24	109	232
R30	800	91



ORIGINAL PAGE IS  
OF POOR QUALITY

### 3.0 CHARACTERIZATION TECHNIQUES

The techniques used to characterize the crystalline perfection, chemical impurities, and electrically active centers in the LEC GaAs are summarized in Table 3.

Table 3. Summary of Techniques Used to Characterize LEC GaAs

Material Parameter	Characterization Technique	Comments
Dislocation Density	Preferential Etching	1) For (100) wafers 2) 25 min in KOH at 400°C
Chemical Impurities	Secondary Ion Mass Spectrometry (SIMS)	1) Charles Evans and Assoc. San Mateo, CA 2) Good for metals and donor impurities in GaAs
Carbon	Localized Vibrational Mode Far-Infrared Absorption (LVM)	1) Measurements made at 77K 2) Reference - M. R. Brozel, J. B. Clegg, and R. C. Newman (1978) J. Phys. D11, 1331
Deep Levels	Photoluminescence	Made by Phil Yu, Wright State University, Dayton, Ohio
EL2 (deep donor)	Optical Absorption in 1.0-1.4 $\mu$ m range	Reference - G. M. Martin (1981), Appl. Phys. Lett. <u>39</u> , 747
Resistivity, Free Carrier Concentration, Hall Mobility	Hall Effect Measurements	1) 300K 2) Dark 3) AuGe:Ni Contacts
Activation Energy of Electron Concentration	High-temperature Hall measurements	300-420K



ORIGINAL PAGE IS  
OF POOR QUALITY

#### 4.0 COMPENSATION MECHANISM OF SEMI-INSULATING LEC GaAs

Results from the NASA-Army and Rockwell IR&D programs indicated that the key to the reproducible growth of undoped semi-insulating GaAs by the liquid encapsulated Czochralski technique is the control over the melt stoichiometry. Studies in the crystal growth IR&D program revealed that the electrical compensation in the semi-insulating material is controlled by the balance between EL2 deep donors and carbon acceptors. Furthermore, the incorporation of EL2 depends on the melt stoichiometry, increasing as the As atom fraction in the melt increases. As a result, semi-insulating material is obtained only above a critical As fraction in the melt. Below the critical composition, the material is p-type. The results of this work, including the identification of the predominant chemical impurities and defects, the development of the compensation model, and the evaluation of the material in terms of the model, are discussed in detail in the two publications given in Appendices I and II. A summary of these results is given in the following section.

##### 4.1 Importance of Melt Stoichiometry

The resistivity of the LEC GaAs is controlled by the melt stoichiometry (Fig. 4). The material is semi-insulating above, and p-type below, a critical melt composition. For example, referring to the electrical properties of the NASA-Army crystals in Table 4, and the melt stoichiometry corresponding to the front and tail of these crystals in Table 5, it can be seen that the resistivity of the crystals grown from As-rich melts (R33 and R34) are semi-insulating from front to tail. However, crystals grown from Ga-rich melts either undergo a transition from semi-insulating to p-type at some point along the crystal, as was the case with R21 and R24, or are p-type throughout (Fig. 5). These results show that the transition to p-type conduction is controlled by the melt stoichiometry and is not related to the normal segregation of a background acceptor impurity toward the tail of the crystal. Otherwise, the tail of the As-rich-grown crystals would be p-type as well. Detailed resistivity profiles of R21 and R24, shown in Table 6, pinpoint the



ORIGINAL PAGE IS  
OF POOR QUALITY

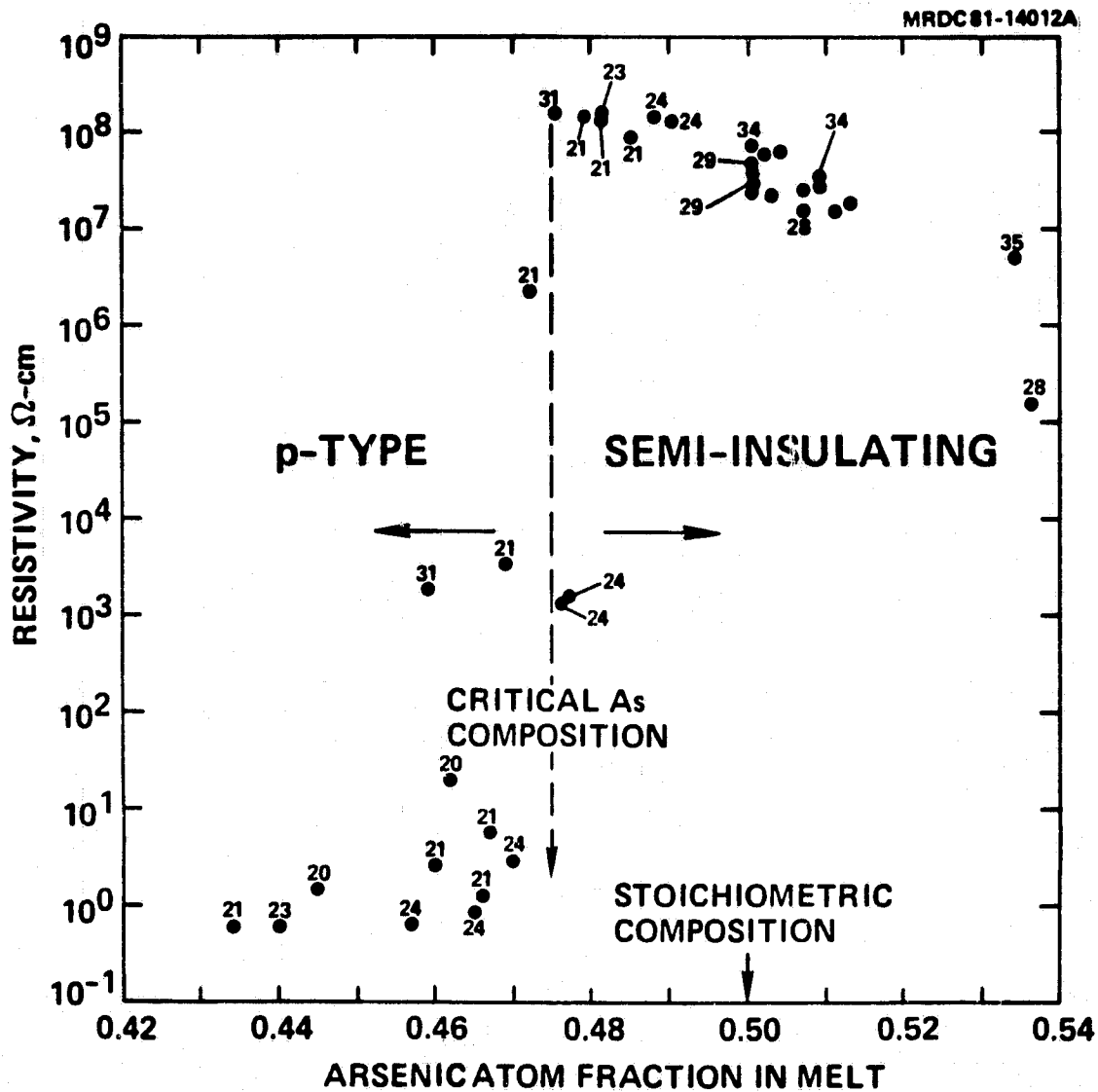


Fig. 4 Dependence of electrical resistivity of LEC GaAs on melt stoichiometry. Semi-insulating material is obtained above, and p-type (low resistivity) material below a critical melt composition of about 0.475 atom fraction.



Table 4. Electrical Characteristics of NASA-ARMY Crystals

Sample No.*	Resistivity $\Omega\text{-cm}$	Type	Free Carrier Concentration $\text{cm}^{-3}$	Hall Mobility $\text{cm}^2 \text{V}^{-1} \text{s}^{-1}$	Sheet Resistivity $\Omega/\square$
R21T	$1.5 \times 10^8$	n	$2.1 \times 10^7$	1962	$2.5 \times 10^9$
R21F	0.60	p	$3.9 \times 10^{16}$	278	-
R24F	$1.3 \times 10^7$	n	$1.8 \times 10^7$	2774	$2.5 \times 10^9$
R24T	0.65	p	$2.9 \times 10^{16}$	328	-
R30	Delivered whole				
R33F	$4.2 \times 10^7$	n	$3.4 \times 10^7$	4433	$1.3 \times 10^9$
R33T	$7.3 \times 10^6$	n	$1.9 \times 10^8$	4614	$1.0 \times 10^8$
R34F	$6.1 \times 10^7$	n	$2.5 \times 10^7$	4189	$1.0 \times 10^9$
R34T	$3.4 \times 10^7$	n	$3.8 \times 10^7$	4812	$7.7 \times 10^8$
R39	Delivered whole				

\* F = Front of ingot  
T = Tail of ingot



Table 5. Melt Stoichiometry Corresponding to the Growth  
of Front and Tail of NASA-Army Crystals

Sample No.	R21F	R21T	R24F	R24T	R30F	R30T	R33F	R33T	R34F	R34T	R39F	R39T
Melt Composition, As Atom Fraction	0.481	0.434	0.490	0.457	Deliverable	*	*	*	0.502	0.509	Deliverable	

\* Significant thermal degradation occurred on the surface of crystal R33 due to the low ambient pressure used for this particular experiment. The degradation was so extensive that we could not separate contributions to the total weight loss of the As weight loss from the crucible during the heat-up cycle (before the experiment) and the weight loss due to the degradation (after the experiment). The initial melt composition therefore could not be determined (see text). However, the presence of excess As in the charge remaining in the crucible after the run indicated that the crystal was indeed grown under As-rich conditions.





ORIGINAL PAGE IS  
OF POOR QUALITY

MRDC81-14013

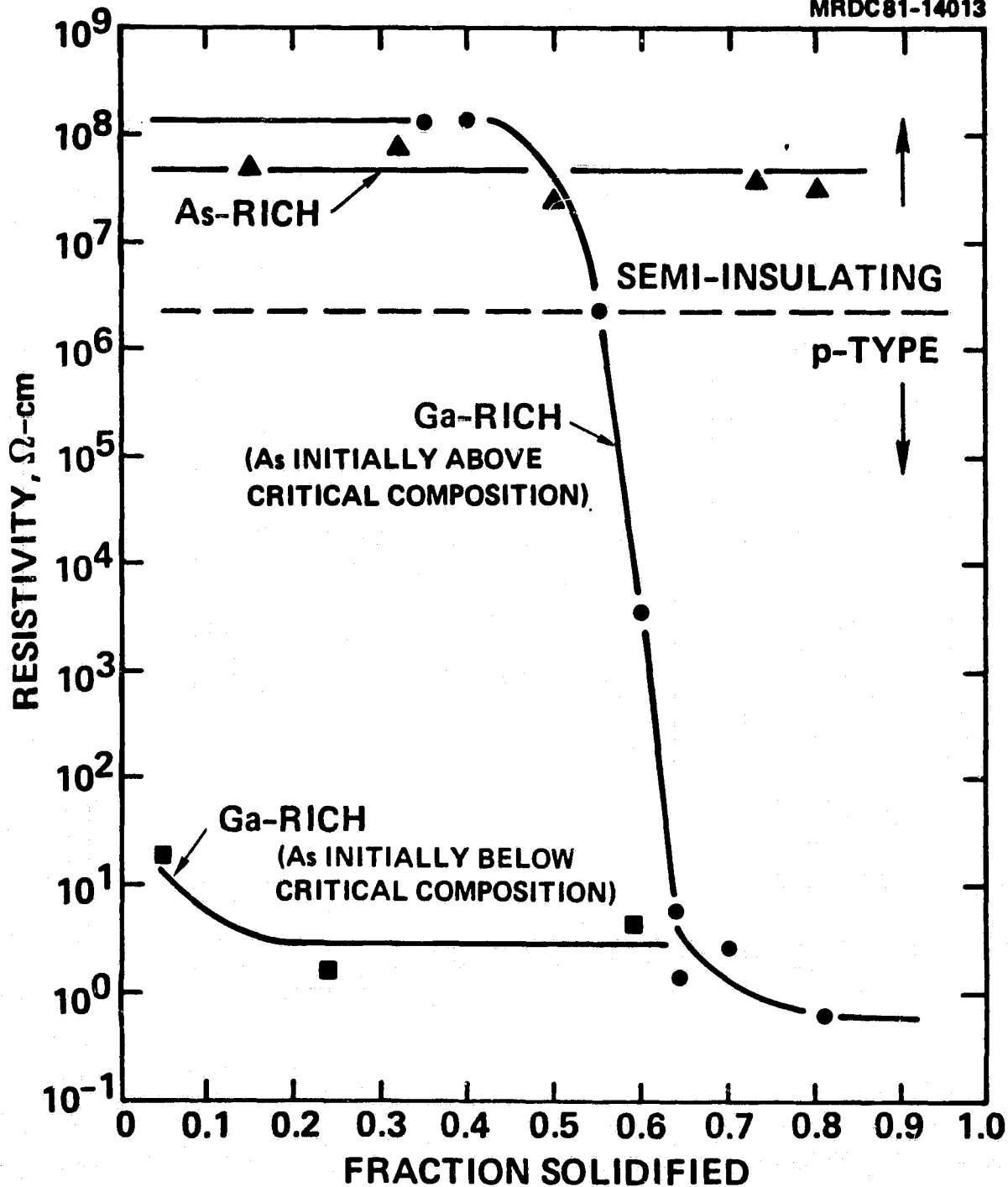


Fig. 5 Resistivity profiles for LEC GaAs crystals grown from Ga-rich and As-rich melts.



ORIGINAL PAGE IS  
OF POOR QUALITY

Table 6. Detailed Resistivity Profiles and Stoichiometry  
of NASA-Army Crystals R21 and R24\*

Crystal No.	Wafer No.**	Resistivity $\Omega\text{-cm}$	Type	Carrier Concentration $\text{cm}^{-3}$	Hall Mobility $\text{cm}^2 \text{V}^{-1} \text{s}^{-1}$	As Atom Fraction in Melt
R21	F-1	$1.2 \times 10^8$	n	$4.4 \times 10^7$	1237	0.481
R21	F-6	$1.5 \times 10^8$	n	$2.1 \times 10^7$	1962	0.479
R21	14	$2.3 \times 10^6$	p	$2.6 \times 10^{10}$	106	0.472
R21	21	$3.7 \times 10^3$	p	$1.2 \times 10^{14}$	15	0.469
R21	23	5.8	p	$9.7 \times 10^{15}$	115	0.467
R21	T-1	1.2	p	$2.1 \times 10^{16}$	243	0.466
R21	T-6	2.7	p	$1.1 \times 10^{16}$	215	0.460
R21	Real Tail	0.6	p	$3.9 \times 10^{16}$	278	0.434
R24	F-2	$1.3 \times 10^8$	n	$1.8 \times 10^7$	2774	0.490
R24	F-7	$1.4 \times 10^8$	n	$1.4 \times 10^7$	3257	0.488
R24	13	$9.4 \times 10^7$	n	$1.9 \times 10^7$	3451	0.485
R24	23	$1.6 \times 10^3$	p	$1.7 \times 10^{14}$	23	0.477
R24	26	$1.4 \times 10^3$	p	$1.8 \times 10^{14}$	25	0.476
R24	T-1	3.00	p	$8.0 \times 10^{15}$	260	0.470
R24	T-5	0.84	p	$2.4 \times 10^{16}$	309	0.465
R24	Real Tail	0.65	p	$2.9 \times 10^{16}$	328	0.457

\*Hall measurements made at room temperature.

\*\*Wafers are listed in consecutive order from front to tail.



critical melt composition of the semi-insulating-to-p-type transition at 0.475 As atom fraction in our material.

#### 4.2 Chemical Impurities and Electrically Active Centers

To gain a better understanding of the compensation mechanism in the semi-insulating material, the predominant chemical impurities and electrically active centers were identified. The concentration of background impurities in the NASA-Army crystals, shown in Table 7, are consistent with SIMS and LVM studies of approximately 20 crystals grown in this crystal puller. Boron is the predominant chemical impurity in the material ( $6 \times 10^{15}$  to  $2 \times 10^{17}$   $\text{cm}^{-3}$ ). However, boron is isoelectronic with Ga and is not electrically active in this concentration range. Carbon is the predominant electrically active chemical impurity ( $3 \times 10^{15}$  to  $1.5 \times 10^{16}$   $\text{cm}^{-3}$ ). Note that the Si concentration is typically below the  $1 \times 10^{15}$   $\text{cm}^{-3}$  level, more than a factor of about 10 lower than in Bridgman material analyzed.

The predominant deep center in the semi-insulating material, studied as a part of the IR&D work, is the deep donor commonly referred to as EL2. This center was identified by optical absorption in the 1.0 to 1.4  $\mu\text{m}$  range (Fig. 6) and by the activation energy of the electron concentration (Fig. 7), which was found to be  $0.75 \pm 0.02$  V. For the first time, it was shown that the EL2 concentration in the bulk material depends on the composition of the melt (Fig. 8).



Table 7. Impurity Analysis of MASA-Army Crystals\*

Sample No.	Si	S	Se	Te	Mg	Cr	Mn	Fe**	B	C
R21F***	1e16	5e15	<e14	<e14	4e14	2e14	1e15	1e15	6e15	6.8e15
R21T***	2e16	1e16	1e14	<e14	2e14	2e14	8e14	2e15	8e16	1.1e16
R24F	2e14	1e15	<e14	<e14	4e14	2e14	1e15	2e15	4e16	9.0e15
R24T	2e14	3e15	3e14	<e14	2e14	4e14	1e15	2e15	2e17	5.2e15
R30	Deliverable									
R33F	8e13	2e14	<e14	<e14	2e14	3e14	4e14	2e15	3e16	1.0e16
R33T	3e14	2e15	3e14	<e14	2e14	2e14	4e14	2e15	2e17	6.1e15
R34F	3e13	2e14	<e14	<e14	2e14	2e14	4e14	2e15	1e16	1.2e16
R34T	4e13	1e15	<e14	<e14	2e14	2e14	4e14	2e15	2e16	9.9e15
R39	Deliverable									

\* Concentration in units of  $\text{cm}^{-3}$ . Carbon measured by LVM. Other impurities measured by SIMS.

\*\* Represents upper limit to actual concentration because of background sensitivity of SIMS.

\*\*\* The concentration of Si and S in R21 is a factor of 5-20 higher than the typical measured values in our PBN-grown LEC GaAs. Because of this discrepancy, and because the material could not be semi-insulating with such a high donor concentration, we believe that the S and Si measurements are in error.



MRDC 82-15904

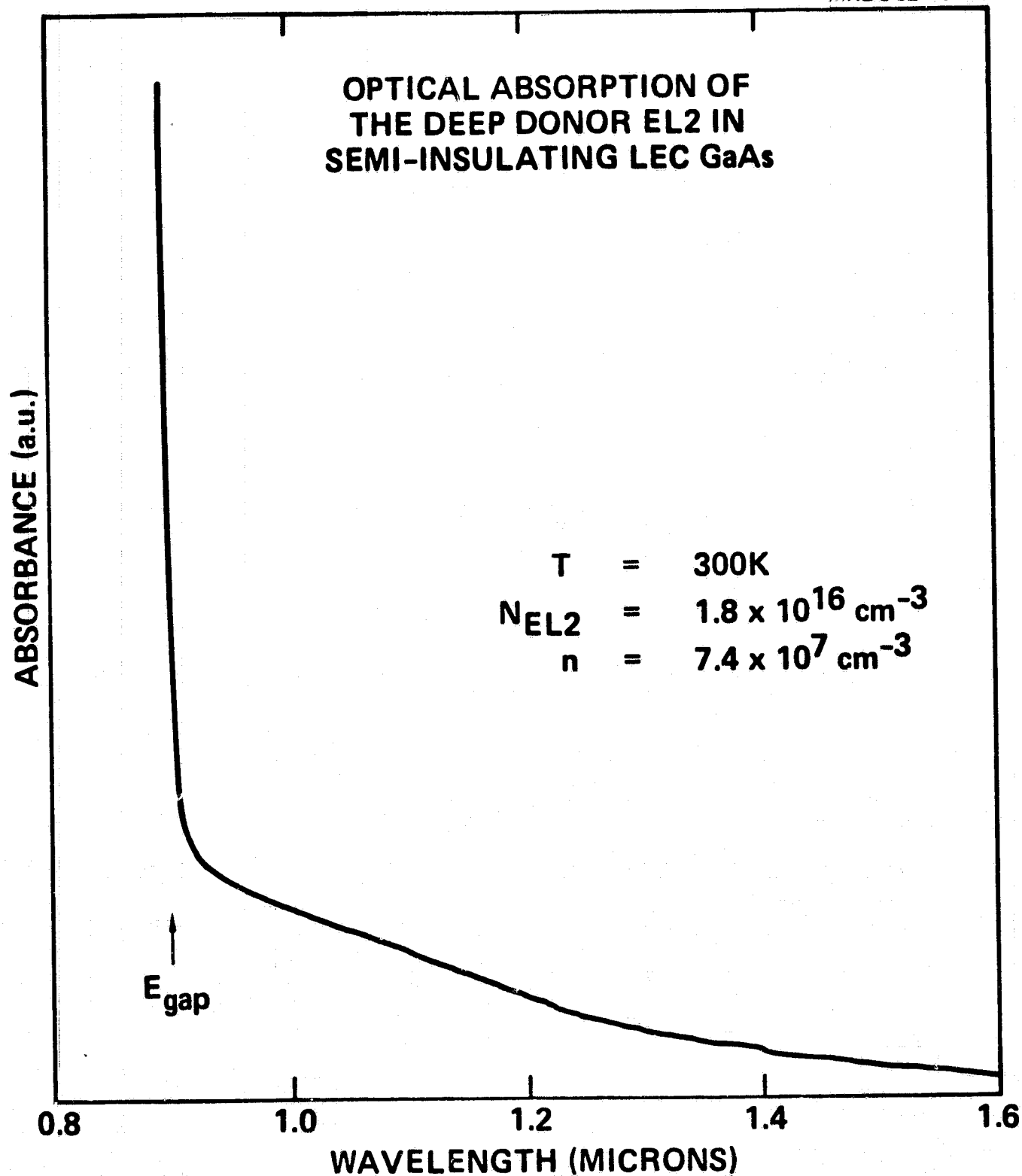


Fig. 6 Typical optical absorption spectrum of GaAs containing EL2.

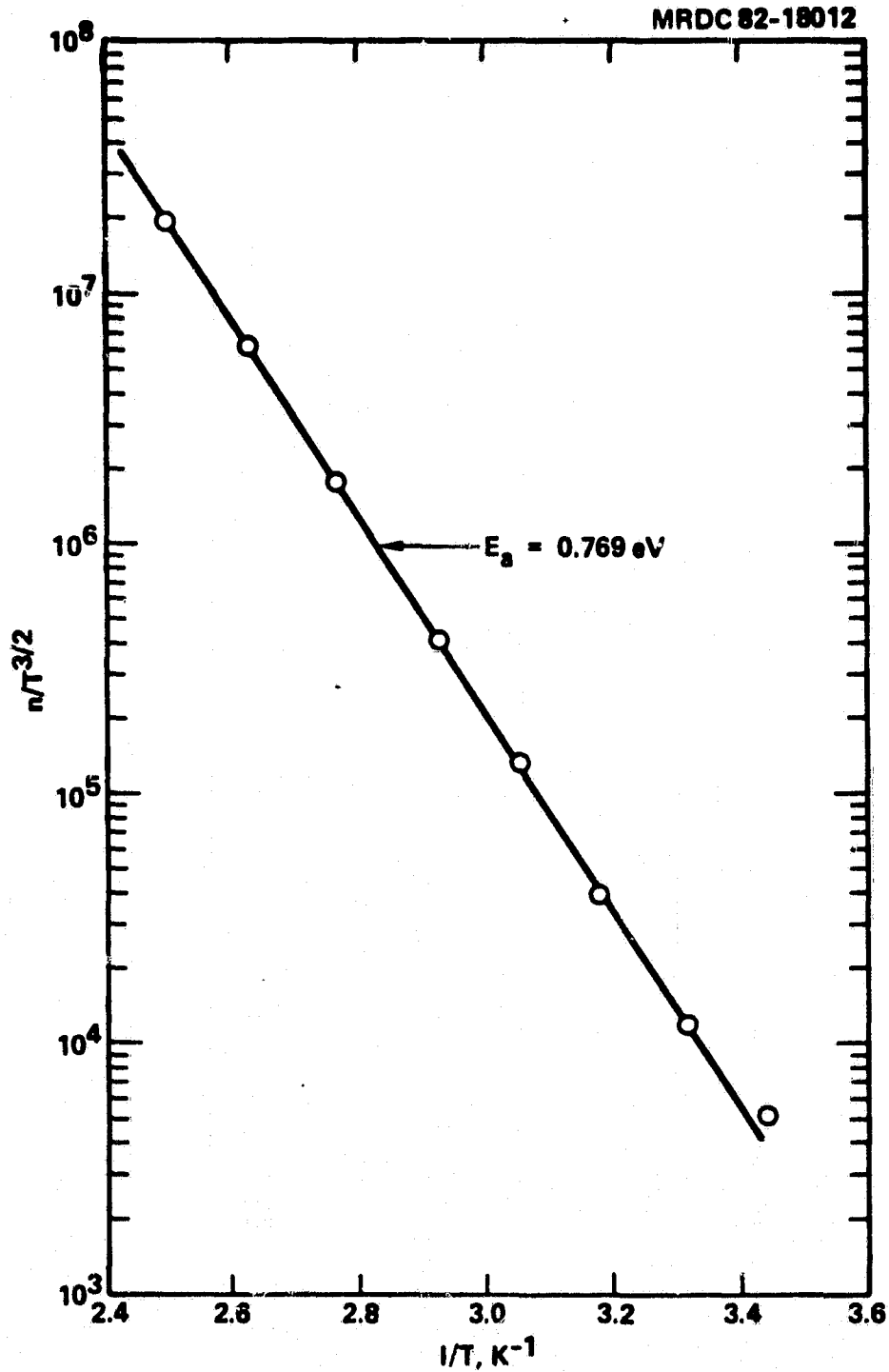


Fig. 7 Temperature-corrected electron concentration - temperature curve of undoped semi-insulating GaAs giving activation energy of the free carriers.



ORIGINAL PAGE IS  
OF POOR QUALITY

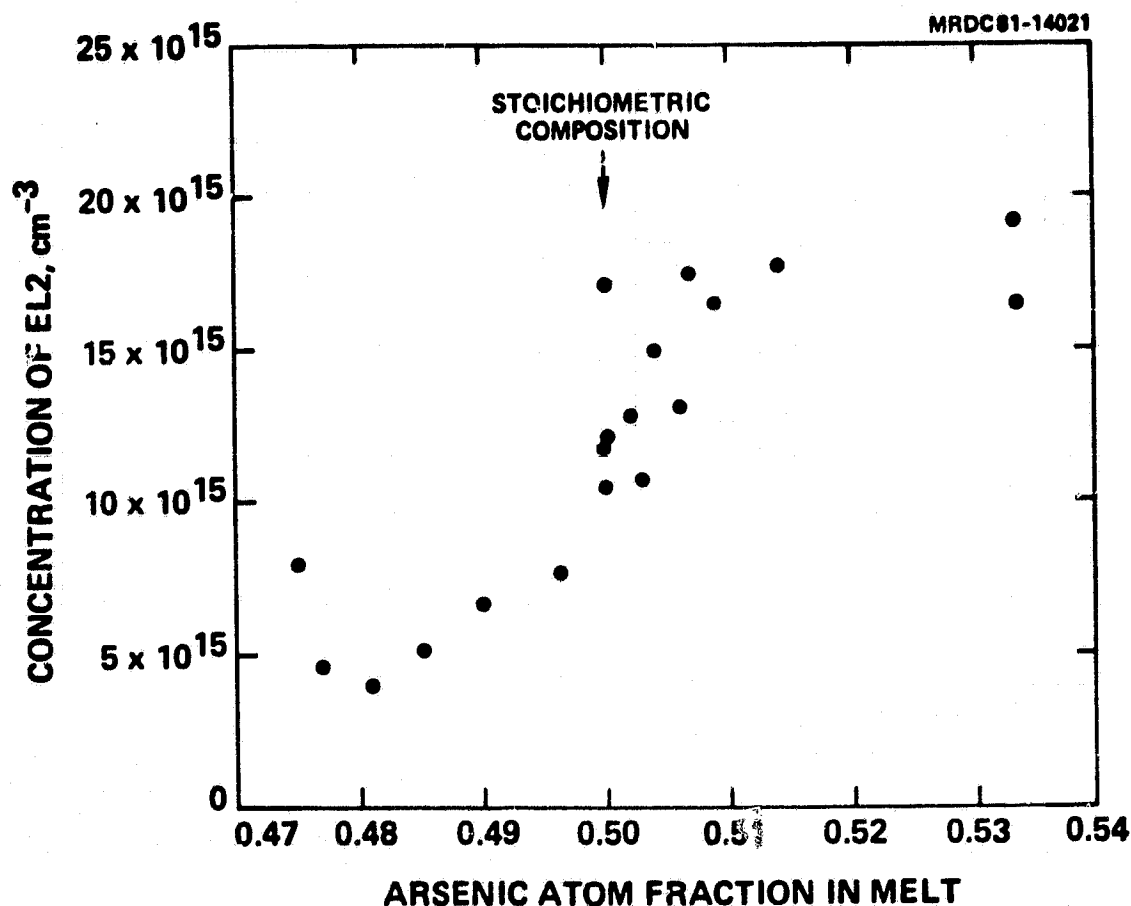


Fig. 8 Dependence of EL2 concentration as determined by optical absorption on the melt stoichiometry. The concentration of EL2 increases from  $5 \times 10^{15} \text{ cm}^{-3}$  to  $1.7 \times 10^{16} \text{ cm}^{-3}$  as the As atom fraction increases from about 0.48 to 0.51, and appears to saturate as the As concentration increases further to 0.53.

## 5.0 REDUCTION OF THE DISLOCATION DENSITY

The effects of several crystal growth parameters on the dislocation density were evaluated in the original NASA program. It was shown that reduced dislocation densities are favored by employing low dislocation seeds and Dash-type seed necking, by maintaining good diameter control, and by growing the crystal with a cone angle greater than about  $25^\circ$ . During the course of the NASA-Army Add-on program, the additional effects of ambient pressure, melt stoichiometry, and  $B_2O_3$  height were studied. More detailed investigations of the effect of the cone angle were also made. The results are discussed in the paper given in Appendix III. The pertinent results are summarized in this section, and the experimentally determined dislocation densities are shown in Table 8.

### 5.1 Cone Angle

In the previous program, it was reported that the dislocation density is virtually independent of the cone angle  $\theta$  for  $20^\circ < \theta < 70^\circ$ , and that unusually high densities occur in crystals grown with a "flat top" ( $0^\circ < \theta < 20^\circ$ ). During the Add-on program, R34 was grown with a  $0^\circ$  cone angle (which we had never done before), representing the ideal "flat-topped" crystal. This experiment was critical to our understanding of the origins of dislocations in LEC GaAs.

The etch pit density (EPD) in the front of R34 was unusually high (low  $10^5 \text{ cm}^{-2}$  range) compared to the other crystals. In addition, the longitudinal EPD (along the crystal) in the front of the crystal was inverted, first decreasing, and then increasing toward the tail. Also, during crystal growth, the crystal began to expand rapidly when the top of the crystal emerged from the  $B_2O_3$  encapsulating layer, leaving a bulge at the distance from the front of the crystal equal to the height of the  $B_2O_3$ .

These observations indicate that the top of the crystal was subjected to significant additional cooling as the crystal emerged from the  $B_2O_3$  layer. As a result, the flat-top crystal experienced "thermal shock" as it





Table 8. Dislocation Density and Distribution  
in NASA-Army Crystals

Sample No.	Dislocation Density, $\text{cm}^{-3}$						
	Front			Region	Tail		
	1	2	3		1	2	3
R21	2.3e4	3.3e4	3.0e5		1.0e5	1.0e5	2.4e5
R24	1.2e4	2.6e4	1.1e5		*	*	*
R30				Deliverable			
R33	6e3	1.8e4	9.6e4		**	**	**
R34***	1.1e5	2.4e5	2.7e5		1.3e5	2.3e5	1.6e5
R39				Deliverable			

\* Data not obtainable because the crystal twinned. The orientation of the wafers obtained from the tail of the crystal was not (100). Our preferential etch can be used only for (100) orientations.

\*\* Ga inclusions, which formed as a result of surface degradation under low pressure, led to extremely high EPD in tail uncharacteristic of as-grown material (see text).

\*\*\* Unusually high EPD in front resulted from flat-top growth (see text).

suddenly emerged from the  $B_2O_3$ . Presumably, the inverted dislocation density along the crystal resulted from the formation of a "secondary" distribution of dislocations, which formed after, and added to the grown-in distribution.

Detailed studies of longitudinal cross sections of crystal cones varying in cone angle from 20 to 65° further support the conclusion that additional dislocations form near the top of the crystal as the crystal emerges from the  $B_2O_3$ .

The radial EPD distribution (across wafers) is "W"-shaped (Fig. 9). In addition, the EPD at a particular position in the crystal body at a constant distance from the center increases toward the tail. However, the EPD in the cone region actually increases, and then decreases before the crystal reaches full diameter, resulting in a local maximum of the EPD. The EPD value at the maximum increases, and the position of the maximum is closer to the seed, as the cone angle decreases. This behavior is consistent with the results obtained on the flat-top crystal, R34. Indeed, R34 represents the limiting case of a 0° cone, in which the EPD value at the maximum is the highest observed in any of these crystals, and the position of the maximum within the crystal lies directly below the seed.

These results are important because they show that the convective heat transfer from the surface of the crystal to the high pressure Ar ambient is greater than the heat transfer to the liquid  $B_2O_3$  encapsulating layer. As a result, radial temperature-gradient-induced stress increases as the crystal emerges from the  $B_2O_3$ . Since the crystal above the encapsulating layer is hot enough to undergo plastic deformation, additional dislocations are created.

Two additional growth parameters were varied to reduce the heat losses through the ambient gas, the  $B_2O_3$  layer, and the ambient pressure.

## 5.2 $B_2O_3$ Thickness

The EPD in the front of the crystals was found to decrease as the thickness of the  $B_2O_3$  increases as shown in Table 9. In view of the discussion above concerning the relative heat loss to the ambient compared to the heat loss to the  $B_2O_3$ , the reduced EPDs brought about using thicker  $B_2O_3$  layers probably

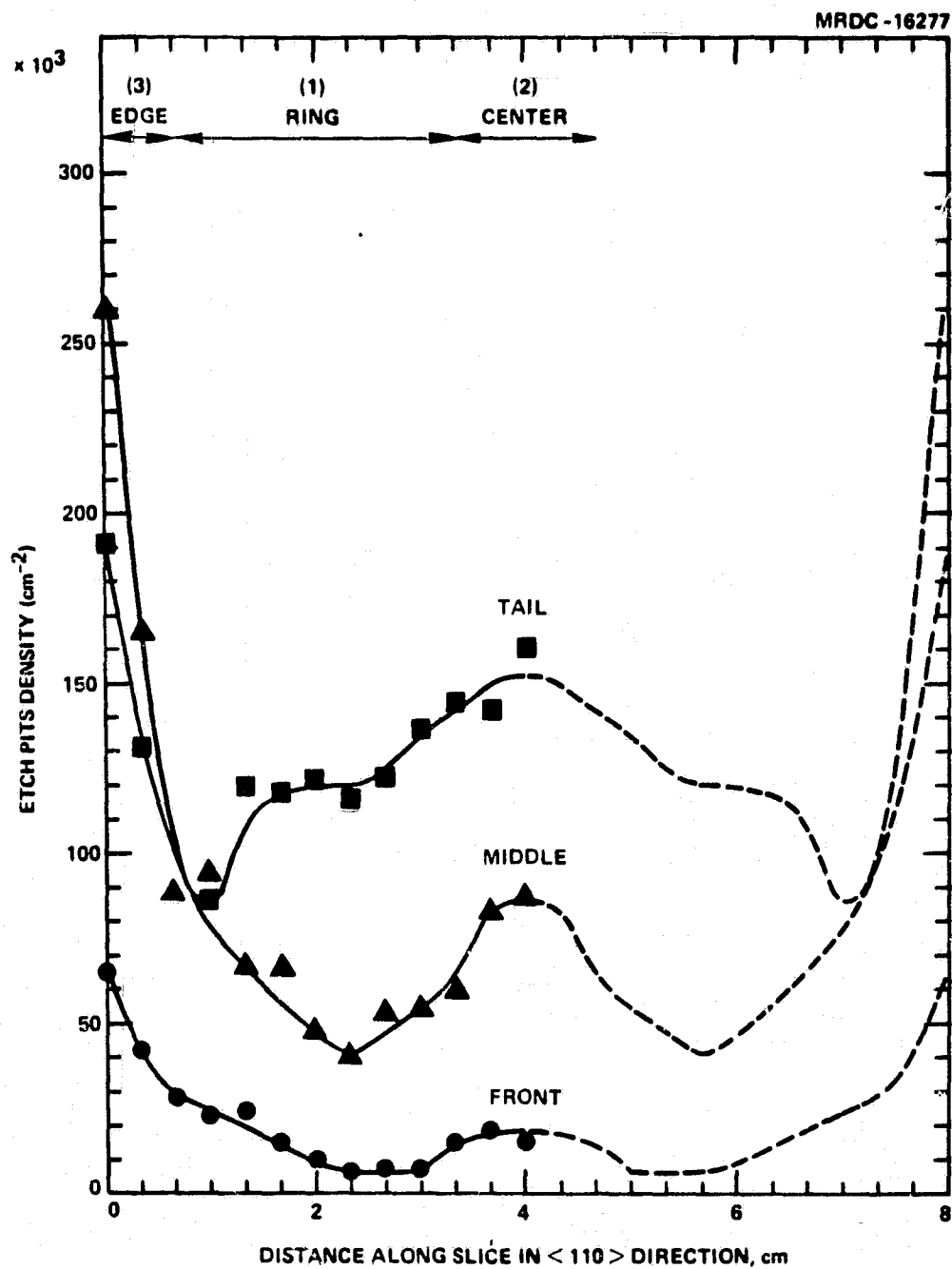


Fig. 9 Radial dislocation density profiles across wafers obtained from the front, middle, and tail of a crystal. The radial profiles are "W"-shaped and the average EPD increases from the front to the tail.

ORIGINAL PAGE IS  
OF POOR QUALITY

Table 9. Effect of  $B_2O_3$  Height on Dislocation Density

Ingot No.	Weight of <sup>+</sup> $B_2O_3$	EPD ( $cm^{-2}$ )	
		Front	Tail
R32	270 gm	1 $3.5 \times 10^4$	$8.0 \times 10^4$ *
		2 $1.0 \times 10^5$	$1.1 \times 10^5$ *
		3 $1.5 \times 10^5$	$2.0 \times 10^5$ *
R35**	390 gm	1 $1.3 \times 10^4$	$1.4 \times 10^5$
		2 $2.8 \times 10^4$	$2.2 \times 10^5$
		3 $1.7 \times 10^5$	$2.4 \times 10^5$
R29**	500 gm	1 $1.2 \times 10^4$	$9.0 \times 10^4$
		2 $1.7 \times 10^4$	$1.0 \times 10^5$
		3 $2.5 \times 10^5$	$2.2 \times 10^5$

+: Other growth parameters are similar.

\*:  $\sim 3/4$  ingot length area.

\*\* : Ingots grown under Rockwell IR&D program.

result from more effective thermal isolation between the hot region of the crystal and the Ar ambient due to an increase in the effective ambient temperature. These results suggest that further increases in  $B_2O_3$  layer thickness will lead to even lower EPDs.

### 5.3 Ambient Pressure

Crystal R33 was grown at an ambient pressure of 50 psi, which is low compared to the standard pressure of 300 psi. The EPD at the front of this crystal was compared to that of another crystal grown under very similar conditions, except that the ambient pressure was 300 psi. The results, shown in Table IV of Appendix III, show an average reduction in EPD of 45% in the crystal grown at low pressure. This behavior can be explained.

The heat transfer coefficient of the crystal-ambient surface is expected to increase as the square root of the ambient pressure. Therefore, we could expect a reduction in the heat transfer coefficient by a factor of about 2.5 by reducing the pressure from 300 to 50 psi. The experimental finding of a 50% reduction in EPD is consistent with the theoretical prediction.

Although further reductions in ambient pressure would lead to corresponding reductions in EPD, serious problems could arise due to thermal degradation (preferential As evaporation) of the surface of the crystal. In fact, significant surface degradation was observed on R33. Since As preferentially evaporates, liquid Ga remains on the surface which can migrate into the crystal yielding poor-quality crystals. Therefore, the ambient pressure cannot be reduced to too low a level in an effort to achieve low dislocation material without sacrificing the entire crystal. Further work is needed to identify the minimum acceptable ambient pressure in this system.

## 6.0 REDUCED INCIDENCE OF TWINNING

A major problem which had affected the yield of GaAs material suitable for device processing was the incidence of the twin formation. Twinning causes changes in the crystallographic orientation of the material and can lead to polycrystallinity and grain-boundary formation.

We have found that control over the melt stoichiometry is important to prevent twin formation, as described in Appendix IV. Twenty crystals were grown from stoichiometric and nonstoichiometric melts. The incidence of twinning was shown to be reduced significantly when crystals are grown under As-rich, near-stoichiometry conditions as indicated in Table 10. We are presently experiencing better than a 90% yield of single-crystalline material using this recipe.



ORIGINAL PAGE IS  
OF POOR QUALITY

Table 10. Incidence of Twinning in Large-Diameter (100) LEC GaAs Crystals<sup>†</sup>

Crystal No.	Crucible Material	Melt Stoichiometry	Melt Composition, Initial	As	Atom Fraction, Final	Result
R20	PBN	Ga-rich	0.462		0.445	Twin
R31	"	"	0.477		0.459	Twin
R23	"	"	0.486		0.439	Twin
R21 (NASA-Army)	"	"	0.488		0.434	Single
R17	"	"	0.489		0.439	Single
R24 (NASA-Army)	"	"	0.492		0.457	Twin
R18	"	"	-		-	Twin
R8	Quartz	"		**		Twin
R9	"	"		**		Single
R11	"	"		**		Twin
R14	"	"		**		Twin
R15	"	"		**		Single
R30 (NASA-Army)	PBN	As-rich	0.500		0.500	Single
R38	"	"	0.500		0.500	Single
R27	"	"	0.500		0.501	Single
R39 (NASA-Army)	"	"	0.501		0.508	Single
R40	"	"	0.502		0.512	Single
R34 (NASA-Army)	"	"	0.502		0.509	Single
R35	"	"	0.504		0.534	Twin
R28	"	"	0.506		0.536	Single

<sup>†</sup>160-500 ppm H<sub>2</sub>O in B<sub>2</sub>O<sub>3</sub> refers to a "flat-top" cone.

\*Calculated melt composition corresponding to the growth of the front (initial) and tail (final) of the crystal.

\*\*See Text.

<sup>†</sup>The angle between the wall of the cone and the horizontal e.g., a 0° cone



## 7.0 APPLICATION OF LEC GaAs IN FABRICATION

Several wafers obtained from the NASA-Army crystals were used in digital integrated circuit processing with excellent results. Both discrete devices such as FETs, as well as circuits, such as 9-stage ring oscillators and RAMs (random access memories) were fabricated. A micrograph of a RAM fabricated under our DARPA-supported RAM development program is shown in Fig. 10. We have also evaluated the uniformity of implanted layers activated directly in the material. Good uniformity is important to fabricate high performance circuits.

The uniformity of implanted layers in the NASA-Army material was evaluated by mapping the depletion-voltage of Schottky barriers across quarters of 3-inch wafers by C-V profiling, as shown in Fig. 11a-d. (The depletion voltage is analogous to the pinchoff voltage in an FET.) The average depletion voltage  $V$ , standard deviation of the depletion voltage  $\sigma_V$ , and the number of diodes tested are summarized in Table 11. We have also fabricated arrays of 1- $\mu$ m-gate FETs in our process line on several wafers obtained from R34. The standard chip size for processing is 1-inch squares. Maps of the actual pinchoff voltage  $V_p$  of four of these wafers are shown in Fig. 12a-d, and values of  $V$ ,  $\sigma_V$ , and  $n$  are given in Table 12.

Our experience at Rockwell in the GaAs IC technology indicates that the uniformity of  $V_p$  (and  $V_d$ ) in processed wafers reflects both the material and the processing. We typically see values of  $\sigma_V$  of about 50-70 meV in processed circuits, which is an acceptable tolerance for depletion-mode devices. An exceptionally low value of 25 meV was obtained on one of the R34 wafers CR34A (Fig. 11a, Table 12). In fact, to our knowledge, this is the best result ever achieved at any laboratory by direct ion implantation. This result illustrates the degree of uniformity achievable by direct implantation in undoped LEC GaAs. Although all four values of  $\sigma_V$  for R34 are excellent, the data could indicate a significant contribution of the device processing to the variability of  $\sigma_V$  in the circuits because these four wafers were processed together. The relatively high value of the standard deviation of the depletion voltage on the quadrant map of R34 (Fig. 11d) would also seem to be





ORIGINAL PAGE  
BLACK AND WHITE PHOTOGRAPH

MRDC82-18140

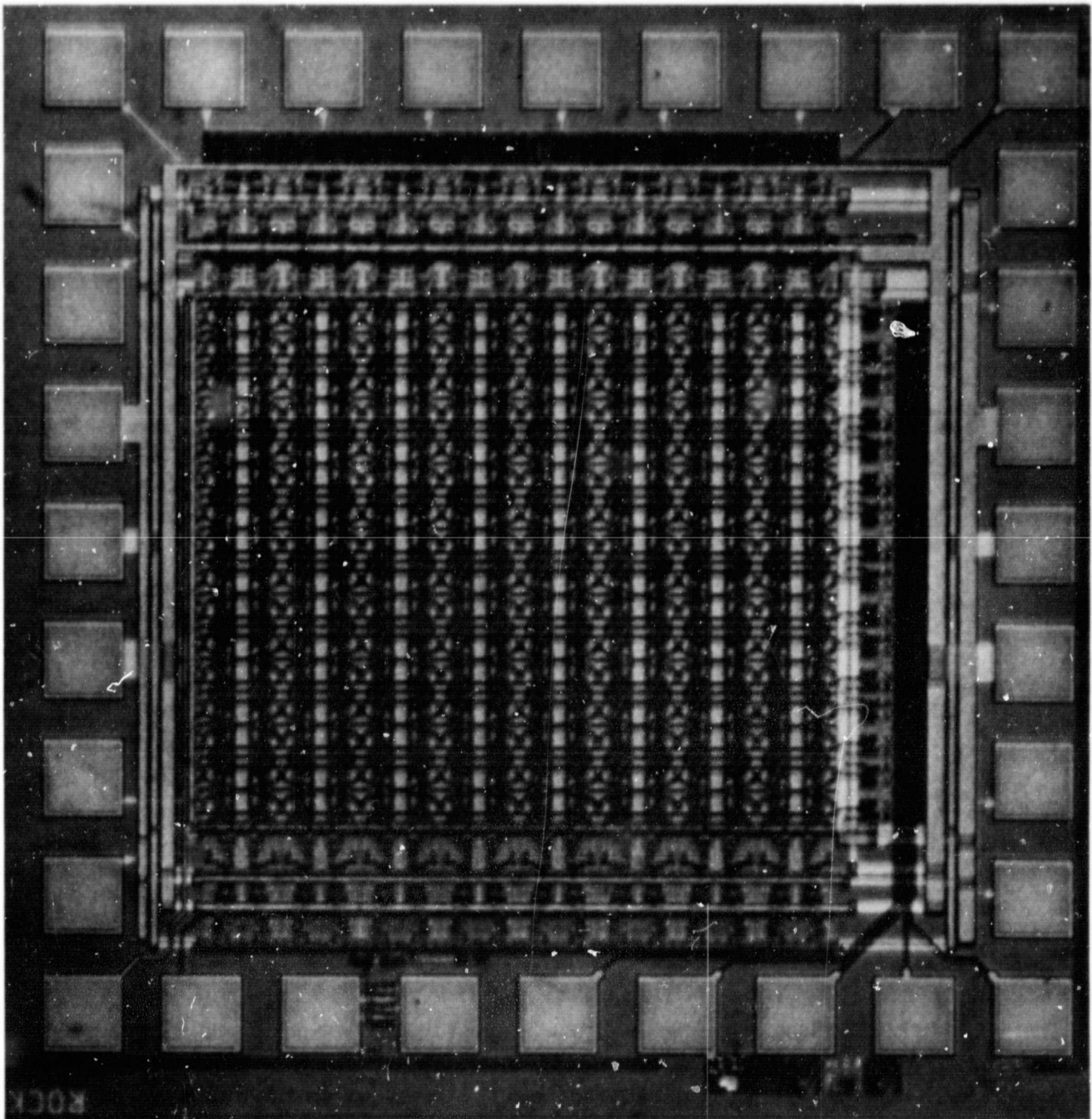


Fig. 10 Photograph of RAM processed on LEC GaAs.



ORIGINAL PAGE IS  
OF POOR QUALITY

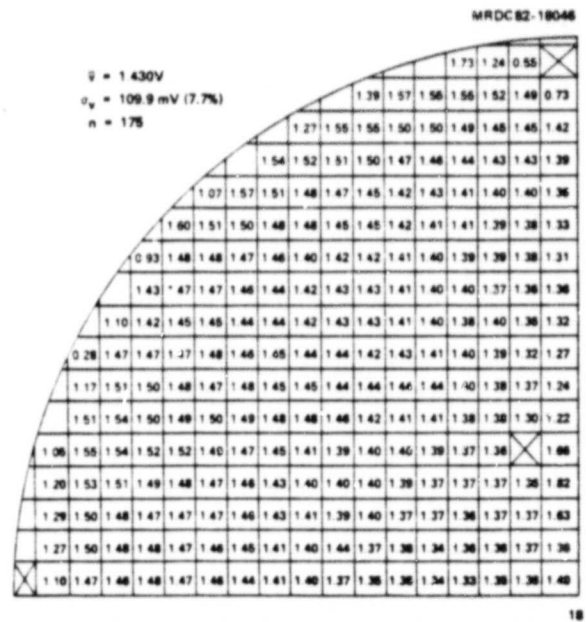
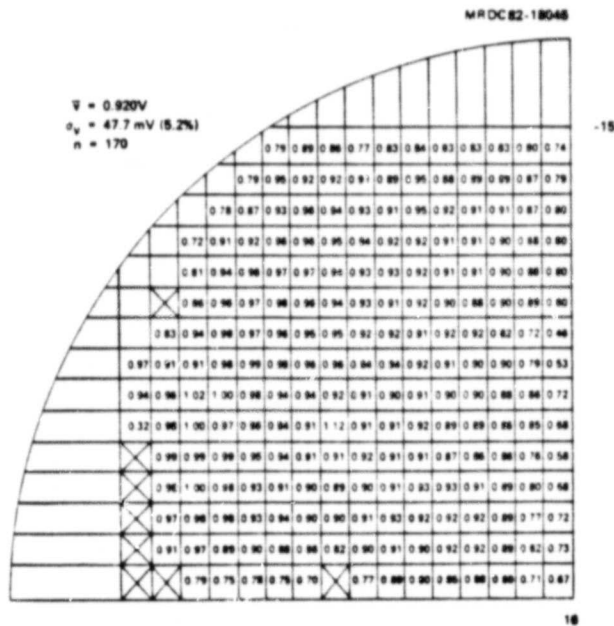
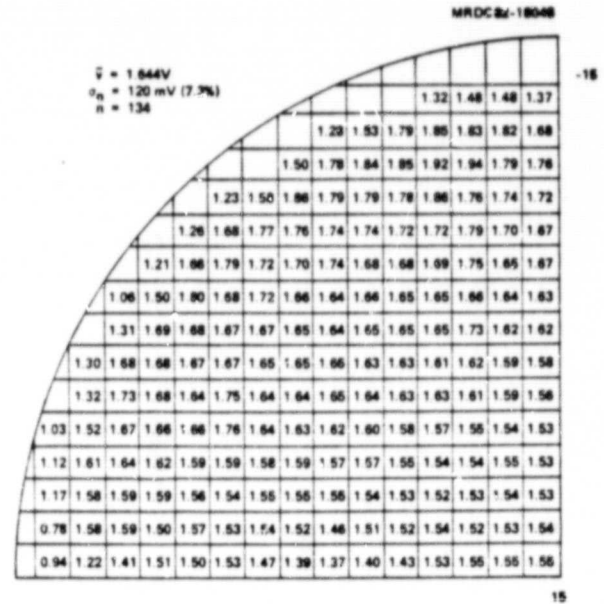
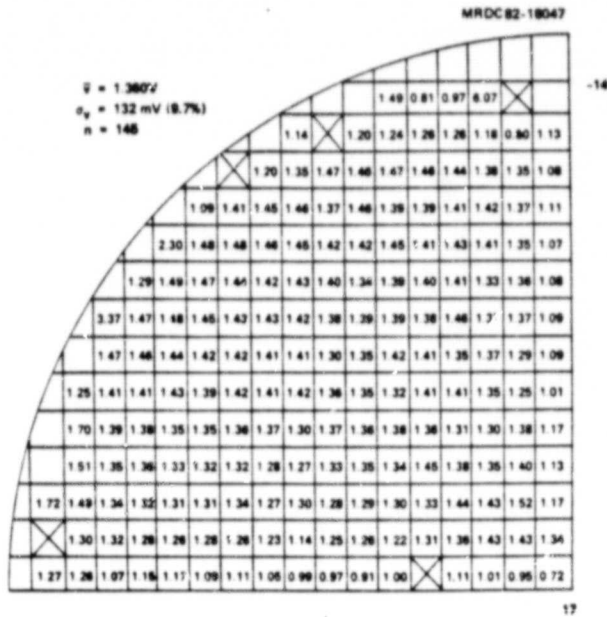


Fig. 11 (a-d) Depletion voltage maps of NASA-Army crystals for 320 keV Se implanted through 750Å Si<sub>3</sub>N<sub>4</sub> to a dose of 2.5 E12/cm<sup>2</sup>.

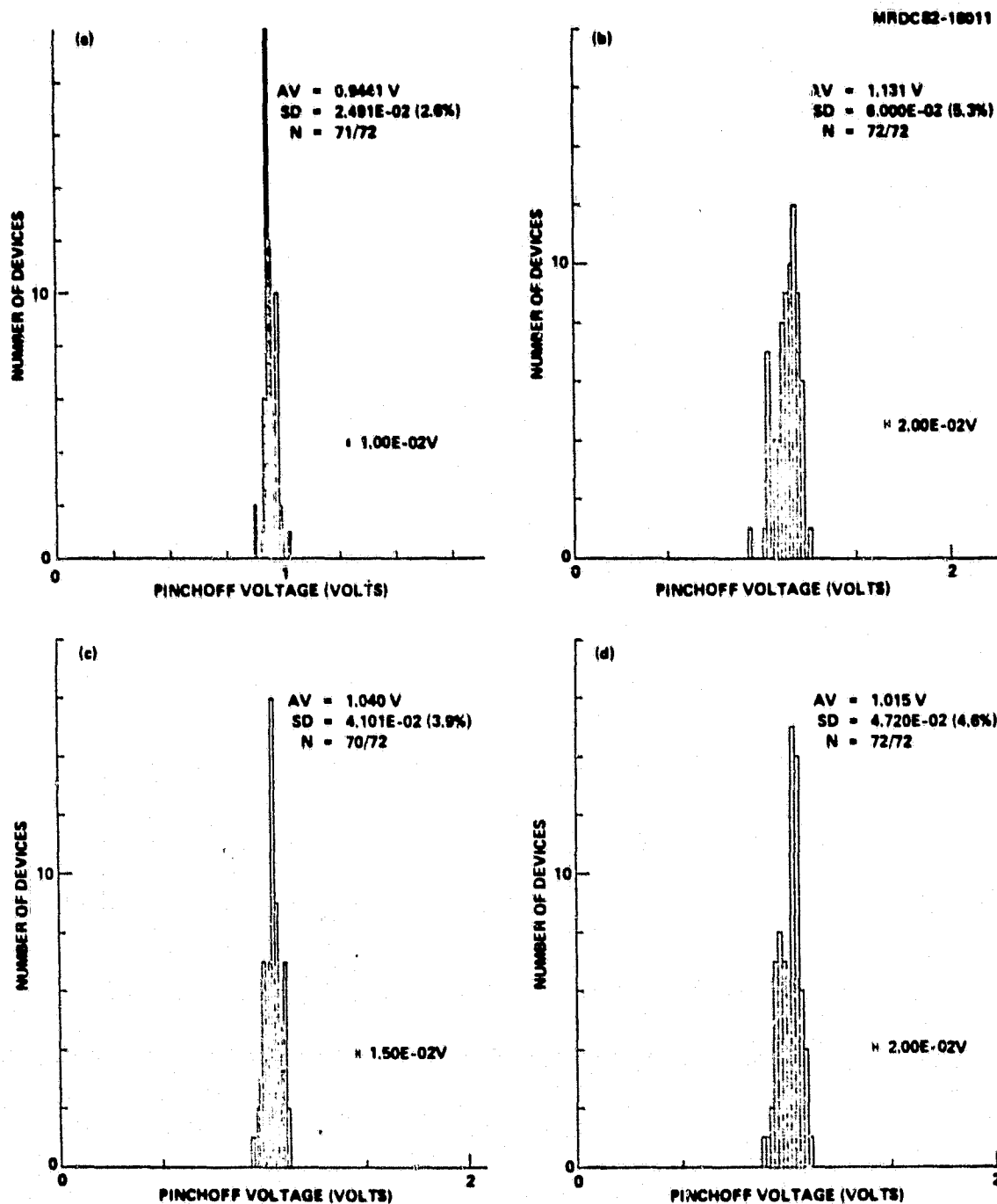


Fig. 12 Pinchoff voltage maps of FET arrays fabricated on NASA-Army crystal R34.



Table 11. Summary of Studies of Depletion Voltage  
Uniformity Across 3-Inch Wafers (C-V)

Crystal No.	Average Depletion Voltage, V $\bar{V}$	Standard Deviation of Depletion Voltage, mV $\sigma_V$	Number of Diodes Tested n
R21	1.360	132 (9.7%)	145
R24	1.644	120 (7.3%)	134
R33	0.920	47.7 (5.2%)	170
R34	1.430	109.9 (7.7%)	175

\*The variations of  $\bar{V}$  from sample to sample are due primarily to the fact that special processing was required to make these measurements. The top surface of the implanted wafers was inadvertently etched when the  $\text{Si}_3\text{N}_4$  cap was removed, leading to variations in the thickness of the implanted layer and corresponding variations in  $\bar{V}$ . This etching step could also have influenced the uniformity across each wafer.

Table 12. Pinchoff Voltage of FET Arrays on Simultaneously  
Processed 1-Inch Wafers from NASA-Army Crystal R34

Wafer No.	Pinchoff Voltage ( $V_p$ ) $V$	Standard Deviation of $V_p$ ( $\sigma_V$ ) mV	Number of FETS, Operating/Total
224	0.9441	24.9 (2.6%)	71/72
223	1.131	60.0 (5.3%)	72/72
222	1.040	41.0 (3.9%)	70/72
221	1.015	47.2 (4.6%)	72/72

inconsistent with the 25 meV standard deviation of  $V_p$  of the FET arrays fabricated from the wafers from the same crystal. The apparent inconsistency could also be an indication of process-induced variations.

The wafer quadrants used for  $V_d$  mapping studies (Fig. 11) could not be processed simultaneously because of their size and the fact that special processing was required. As a result, it is difficult to draw hard conclusions concerning possible substrate-related variations. Values of  $V_d$  are higher near the edge of all four samples in the  $\langle 100 \rangle$  direction compared to the center of the wafer. This trend correlates with the general trend of the dislocation density, the dislocation density also being higher near the edge in the  $\langle 100 \rangle$  direction. However, the opposite behavior has been observed in other quadrant mapping studies. We are now proceeding to relate the uniformity of device parameters across wafers to the properties of the material.

Finally, we note that very high yields of operating devices has been achieved using R34. The yields of operating FETs experienced in the pinchoff voltage mapping studies exceeded 97% (see Table 13). We have also fabricated five types of 9-stage ring oscillator circuits on R34 for the purpose of optimizing the circuit design. The yield exceeded 92% on each wafer, and the net yield (170/180 operational) was 94%, which is excellent. Although the yield factor may generally be more of an indication of "good" processing, these results do suggest that direct material-related device failure is probably not an important consideration at the present stage of development of ICs.

Table 13. Yield of Five 9-Stage Ring Oscillators  
Fabricated on NASA-Army Crystal R34

Circuit No.	Devices Operating/Total	Yield, %
1	35/36	97
2	35/36	97
3	34/36	94
4	33/36	92
5	33/36	92



## 8.0 SUMMARY

The add-on Army program resulted in substantial progress in the area of LEC growth of high purity, low dislocation undoped GaAs. The results from this program, combined with other findings, contributed to the development of a compensation model for undoped, semi-insulating GaAs. By investigating the effects of cone angle, boric oxide encapsulant thickness, and ambient pressure, we developed procedures for low dislocation density large diameter LEC GaAs. In addition, the incidence of twin formation was reduced by utilizing As-rich melts.

These developments in the LEC GaAs growth process have resulted in substrates with superior electrical and crystalline properties. The outstanding device yield and uniformity data on these substrates reflect these recent improvements.



**Rockwell International**

## **9.0 APPENDICES**



## **9.1 APPENDIX I**



# Stoichiometry-controlled compensation in liquid encapsulated Czochralski GaAs

D. E. Holmes, R. T. Chen, K. R. Elliott, and C. G. Kirkpatrick

Rockwell International Microelectronics Research and Development Center, Thousand Oaks, California 91360

(Received 13 August 1981; accepted for publication 9 October 1981)

We show that the electrical compensation of undoped GaAs grown by the liquid encapsulated Czochralski technique is controlled by the melt stoichiometry. The concentration of the deep donor EL2 in the crystal depends on the As concentration in the melt, increasing from about  $5 \times 10^{15} \text{ cm}^{-3}$  to  $1.7 \times 10^{16} \text{ cm}^{-3}$  as the As atom fraction increases from 0.48 to 0.51.

Furthermore, we show that the free-carrier concentration of semi-insulating GaAs is determined by the relative concentrations of EL2 and carbon acceptors. As a result, semi-insulating material can be obtained only above a critical As concentration (0.475-atom fraction in our material) where the concentration of EL2 is sufficient to compensate residual acceptors. Below the critical As concentration the material is *p* type due to excess acceptors.

PACS numbers: 72.80.Ey, 81.10.Fq, 78.50.Ge

Undoped semi-insulating GaAs grown by the liquid encapsulated Czochralski (LEC) technique is currently receiving attention for applications in integrated circuits<sup>1,2</sup> fabricated by direct ion implantation. An understanding of the electrical compensation mechanism is necessary to allow controlled and reproducible crystal growth. In the present investigation we have analyzed the electrical and optical properties of 12 LEC GaAs crystals grown from stoichiometric and nonstoichiometric melts. The results show that the stoichiometry of the melt controls the electrical compensation of the crystal through incorporation of EL2, a defect that has been implicated<sup>3</sup> as the compensation-controlling center.

The GaAs crystals used in the investigation were grown in the (100) direction from pyrolytic boron nitride (PBN) crucibles using a high pressure LEC crystal puller. The crystal diameter and weight ranged from 2–3 in. and 2.0–2.5 kg, respectively. Dry ( $< 500$ -ppm  $\text{H}_2\text{O}$ )  $\text{B}_2\text{O}_3$  encapsulant (Johnson-Matthey) was used for all growth experiments. The melt was prepared by *in-situ* synthesis, to achieve high purity, by starting with a charge of 6–9's As (Cominco) and 6–9's Ga (Kawecki). To make an accurate determination of the initial melt composition, it was necessary to take into account the loss of As from the charge during the heat-up cycle. We found that the As loss resulted from incomplete wetting of the  $\text{B}_2\text{O}_3$  to the PBN crucible before synthesis. This weight loss was determined by comparing the weight of the initial charge with the weight of the crystal and the charge remaining in the crucible after the growth process. The As concentration of the initial melt was effectively varied from 0.46 to 0.51-atom fraction. Samples for characterization were obtained along the length of each crystal. The melt composition for each of these samples was determined by adjusting the initial melt composition for the crystal weight at the time of growth. The crystal weight and length were recorded during growth as a function of time.

The material was characterized by secondary ion mass spectrometry<sup>4</sup> (SIMS), localized vibrational mode (LVM) far-infrared<sup>5</sup> absorption, room temperature and variable-

temperature (77–400 K) Van der Pauw Hall effect measurements, near-infrared optical absorption, and variable temperature photoconductivity. The predominant background impurity as determined by SIMS was boron ( $1 \times 10^{16} \text{ cm}^{-3}$ – $2 \times 10^{17} \text{ cm}^{-3}$ ) and by LVM carbon ( $3 \times 10^{15} \text{ cm}^{-3}$ – $1.5 \times 10^{16} \text{ cm}^{-3}$ ). The concentrations of other background impurities were typically  $\text{Si} < 2 \times 10^{15} \text{ cm}^{-3}$ ,  $\text{S} < 2 \times 10^{15} \text{ cm}^{-3}$ ,  $\text{Fe} < 3 \times 10^{15} \text{ cm}^{-3}$ , and  $\text{Mn} < 1 \times 10^{15} \text{ cm}^{-3}$ .

The electrical resistivity of the material was found to be a strong function of the melt stoichiometry, as shown in Fig. 1. These data were obtained from the front and tail of each of the 12 crystals and from detailed electrical profiles of 5 crystals. Semi-insulating material was obtained above, and *p*-type material below a critical As concentration of 0.475-atom fraction. The free-hole concentration and Hall mobility of the material grown from Ga-rich (As concentrations below 0.50) melts below the critical composition are in the

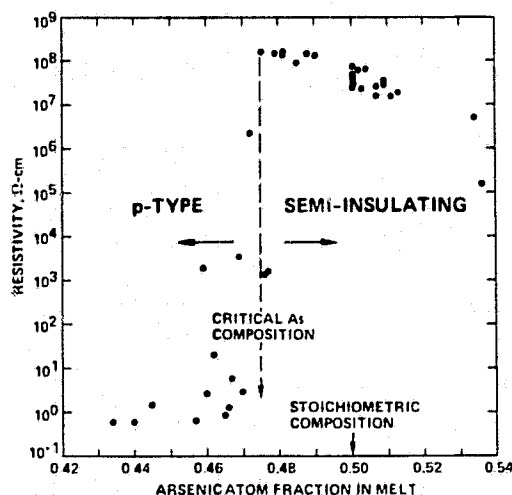


FIG. 1. Dependence of electrical resistivity of LEC GaAs on melt composition. Semi-insulating material is obtained above, and *p*-type material below a critical melt composition of 0.475 As atom fraction.

range of  $1-3 \times 10^{16} \text{ cm}^{-3}$  and  $215-330 \text{ cm}^2 \text{ V}^{-1} \text{ s}^{-1}$ , respectively. The resistivity of the semi-insulating material decreases gradually from about  $1.5 \times 10^8 \Omega \text{ cm}$  to about  $5 \times 10^6 \Omega \text{ cm}$  as the As concentration in the melt increases from 0.475 to about 0.535. The Hall mobility increases from about  $1500 \text{ cm}^2 \text{ V}^{-1} \text{ s}^{-1}$  to about  $6000 \text{ cm}^2 \text{ V}^{-1} \text{ s}^{-1}$ , and the free-electron concentration increases from about  $2 \times 10^7 \text{ cm}^{-3}$  to about  $2.5 \times 10^8 \text{ cm}^{-3}$  over the same melt composition range. The resistivity decreases sharply above about 0.535 As atom fraction as a result of an increase in the free-electron concentration.

Detailed resistivity profiles of crystals grown under As-rich and Ga-rich conditions, as shown in Fig. 2, further emphasize the importance of melt stoichiometry in controlling the electrical compensation. As-rich (Ga-rich) melts become progressively more As-rich<sup>6</sup> (Ga-rich) as the crystal is pulled from the melt. Crystals grown from As-rich melts are semi-insulating (*n*-type) uniformly from front to tail as long as the As atom fraction is less than about 0.535. On the other hand, crystals grown under Ga-rich conditions below the critical composition are invariably *p* type (Fig. 2). Furthermore, crystals grown from Ga-rich melts initially above the critical composition undergo a transition from semi-insulating to *p* type when As in the melt becomes depleted and the composition reaches the critical value. This behavior clearly shows that the semi-insulating to *p*-type transition is controlled by the melt stoichiometry and does not occur as a result of the normal segregation of background impurities in the melt. In addition, our analysis of the distribution of carbon along the crystals by LVM showed no correlation between carbon segregation and stoichiometry.

An absorption band between 1 and  $1.4 \mu\text{m}$  previously identified<sup>7</sup> with the EL2 center was observed in all of our semi-insulating material. The activation energy of the deep level as determined from variable-temperature Hall measurements<sup>3</sup> ( $\sim 0.76 \text{ eV}$ ), and the behavior of the photocon-

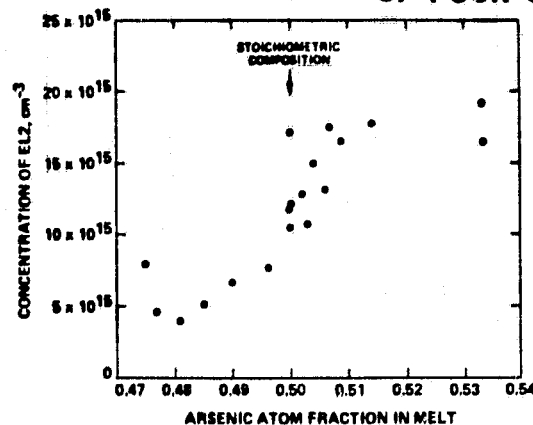


FIG. 3. Concentration of EL2 as determined by optical absorption measurements as a function of melt composition. The concentration of EL2 increases from  $5 \times 10^{15} \text{ cm}^{-3}$  to  $1.7 \times 10^{16} \text{ cm}^{-3}$  as the As atom fraction increases from 0.48 to 0.51 and appears to saturate as the As concentration increases further to 0.53.

ductivity<sup>8</sup> thresholds above and below 120 K were also found to be consistent with the presence of EL2. The concentration of EL2 was determined from the absorption using the cross section reported by Martin *et al.*<sup>9</sup> Absorption due to unoccupied EL2 centers was not observed, and the Hall measurements indicated that the centers were always more than 90% occupied. Consequently, the absorption was taken to be proportional to the total concentration of EL2. The concentration of EL2 was found to depend on the melt stoichiometry, as shown in Fig. 3, increasing from about  $5 \times 10^{15} \text{ cm}^{-3}$  to  $1.7 \times 10^{16} \text{ cm}^{-3}$  as the As atom fraction increased from 0.48 to 0.51. The concentration remained constant as the As fraction increased further to about 0.53. These results

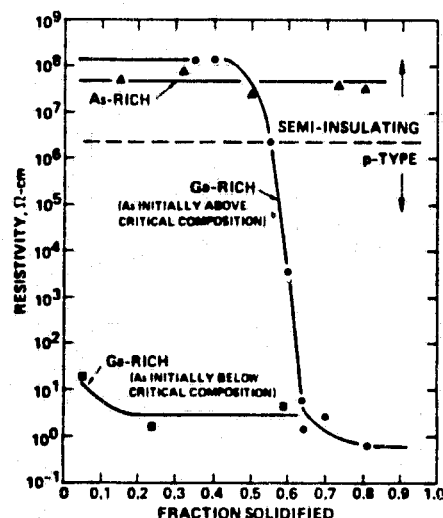


FIG. 2. Resistivity profiles of crystals grown under As- and Ga-rich conditions. The initial melt compositions for the As-rich, Ga-rich (As initially above critical composition), and Ga-rich (As initially below critical composition) crystals are 0.501, 0.481, and 0.462 As atom fraction, respectively.

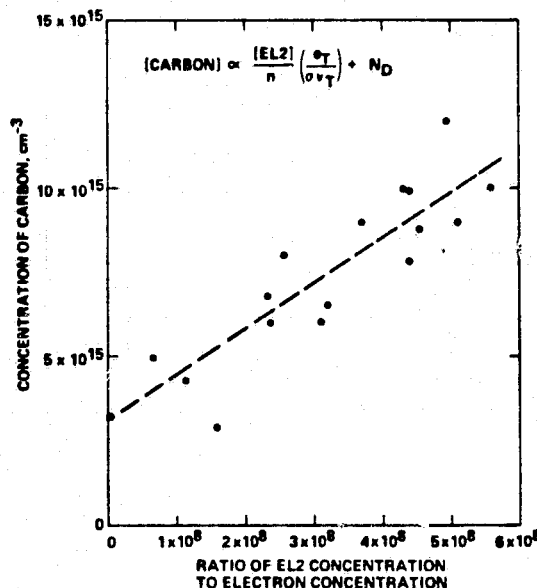


FIG. 4. Carbon concentration as a function of the ratio of the EL2 concentration to the electron concentration evaluated according to the expression given in the legend. The linear behavior indicates the dominant role of EL2 and carbon in controlling the electrical compensation.

are consistent with data obtained on *n*-type material grown by vapor phase epitaxy<sup>10</sup> and organometallic chemical vapor deposition.<sup>11</sup>

Using steady-state generation-recombination considerations we can obtain the expression  $N_A - N_D = N_u/n$  ( $e_T/\sigma v_T$ ), where  $N_A$  and  $N_D$  are the concentrations of acceptors and donors (other than EL2),  $N_u$  is the concentration of occupied deep donors,  $n$  is the free-carrier concentration,  $e_T$  (Ref. 12) is the thermal emission rate,  $\sigma$  (Ref. 13) is the capture cross section, and  $v_T$  is the thermal velocity. We evaluated our results accordingly by plotting  $N_A$  as a function of  $N_u/n$  taking  $N_A$ ,  $N_u$  and  $n$  as the concentration of carbon, occupied EL2 centers, and free-electrons, respectively. The concentrations of carbon (by LVM), EL2 and free-electrons were individually measured for each sample. The plot is linear, as shown in Fig. 4, clearly indicating the dominant role of EL2 and carbon in controlling the electrical compensation. The fluctuations in these data could be attributed to variations in the concentration of other background impurities. The slope of the curve in Fig. 4 is about a factor of 10 higher than the value calculated using published values of the cross section and emission rate for EL2. The discrepancy could be due to errors in the published values for the optical cross sections of carbon and EL2. Another possibility is that carbon behaves either as an amphoteric or inactive impurity in LEC material so that the activation of carbon acceptors is only a fraction of the total concentration.

In summary, we have shown that the melt stoichiometry controls the incorporation of the EL2 center in undoped LEC GaAs. The EL2 center, in turn, controls the semi-insulating properties of the material by compensating residual acceptors, which are principally carbon. The results suggest that the identity of EL2 is associated with an intrinsic (native) defect such as an arsenic interstitial or a vacant gallium site. However, we cannot rule out the possibility that the segregation of oxygen, an impurity that has been associated with high resistivity in GaAs,<sup>14,15</sup> depends strongly on

the stoichiometry. In practical terms, our results show that an essential element in achieving uniform, high resistivity crystals is the close control of the As atom fraction in the melt. A more detailed account of this work will be presented in a future paper.

The authors are grateful to Dr. Peter Asbeck for many helpful discussions during the course of this work. We also appreciate the assistance of Dr. Jane Yang in making the Hall measurements. We also wish to thank the National Aeronautics and Space Administration for partially supporting this work under contract No. NAS3-22224.

<sup>1</sup>R. D. Fairman, R. T. Chen, J. R. Oliver, and D. R. Ch'en, IEEE Trans. Electron Devices ED-28, 135 (1981).

<sup>2</sup>B. M. Welch and R. C. Eden, in 1977 Int. Electron Devices Meeting, Tech. Digest, Dec. 1977, pp. 205-208.

<sup>3</sup>G. M. Martin, J. P. Farges, G. Jacob, and J. P. Hallais, J. Appl. Phys. 51, 2840 (1980).

<sup>4</sup>Charles Evans and Associates, San Mateo, CA.

<sup>5</sup>M. R. Brozel, J. B. Clegg, and R. C. Newman, J. Phys. D 11, 1331 (1978).

<sup>6</sup>The small difference between the stoichiometric and congruent melting compositions has been neglected.

<sup>7</sup>G. M. Martin, *Semi-Insulating III-V Materials*, Nottingham, 1980, pp. 13-28.

<sup>8</sup>A. L. Lin, E. Omelianovski, and R. H. Bube, J. Appl. Phys. 47, 1852 (1976).

<sup>9</sup>G. M. Martin, G. Jacoby, A. Goltzene, and C. Schwab, Proceedings of the 11th Int. Conf. on defects and radiation effects in semiconductors, Oiso, Tokyo, Sept. 1980.

<sup>10</sup>M. D. Miller, G. H. Olsen, and M. Ettenberg, Appl. Phys. Lett. 32, 538 (1977).

<sup>11</sup>P. K. Bhattacharya, J. W. Ku, S. J. T. Owen, V. Aebi, C. B. Cooper, and R. L. Moony, Appl. Phys. Lett. 36, 304 (1980).

<sup>12</sup>K. Sakai and T. Ikoma, Appl. Phys. 5, 165 (1974).

<sup>13</sup>S. Makram-Ebeid, in *Defects in Semiconductors*, Proceedings of the Materials Research Society, Nov. 1980, edited by J. Narayan and T. Y. Tan (North-Holland, New York, 1981).

<sup>14</sup>N. G. Ainslie, S. E. Blum, and J. F. Woods, J. Appl. Phys. 33, 2391 (1962).

<sup>15</sup>A. M. Huber, N. T. Linh, M. Valladon, J. L. Debrun, G. M. Martin, A. Mitonneau, and A. Mircea, J. Appl. Phys. 50, 4022 (1979).

ORIGINAL PAGE IS  
OF POOR QUALITY



**Rockwell International**

## **9.2 APPENDIX II**

**To be published in IEEE Transactions -  
Special Issue on GaAs, June 1982**



COMPENSATION MECHANISM IN LIQUID ENCAPSULATED CZOCHRALSKI GaAs:  
IMPORTANCE OF MELT STOICHIOMETRY

D.E. Holmes, R.T. Chen, K.R. Elliott and C.G. Kirkpatrick  
Rockwell International  
Microelectronics Research and Development Center  
Thousand Oaks, CA 91360

and

P.W. Yu  
University Research Center  
Wright State University  
Dayton, Ohio 45435

ABSTRACT

It is shown that the key to reproducible growth of undoped semi-insulating GaAs by the liquid encapsulated Czochralski technique is the control over the melt stoichiometry. Twelve crystals were grown from stoichiometric and non-stoichiometric melts. The material was characterized by secondary ion mass spectrometry, localized vibrational mode far infrared spectroscopy, Hall effect measurements, optical absorption, and photoluminescence. A quantitative model for the compensation mechanism in the semi-insulating material was developed based on these measurements. The free carrier concentration is controlled by the balance between EL2 deep donors and carbon acceptors; furthermore, the incorporation of EL2 is controlled by the melt stoichiometry, increasing as the As atom fraction in the melt increases. As a result, semi-insulating material can be grown only from melts above a critical As composition. The practical significance of these results is discussed in terms of achieving high yield and reproducibility in the crystal growth process.

## I. INTRODUCTION

A major impediment to the development of GaAs integrated circuits and microwave devices has been the lack of a reliable supply of semi-insulating substrates with reproducible and thermally-stable [1] properties suitable for device fabrication. The liquid encapsulated Czochralski (LEC) technique is currently receiving considerable attention for the production of GaAs crystals because semi-insulating material can be grown without intentional [2] doping, and the technique offers the potential [3,4] for producing round, large-area substrates with uniform properties at a reasonable cost.

The main question surrounding semi-insulating LEC GaAs has concerned the compensation mechanism by which the undoped material is semi-insulating. The understanding of the compensation mechanism has two important practical consequences. First, knowledge of the cause-effect relationships between crystal growth and electrical characteristics of the material would greatly improve the yield of semi-insulating crystals in the growth process, as well as the crystal-to-crystal and wafer-to-wafer reproducibility. Second, this understanding would improve device performance. For example, backgating effects could possibly be diminished by adjusting [5] trap levels in material intended for integrated circuit processing.

It has been shown that the melt stoichiometry [6] is the key parameter which must be controlled to grow undoped semi-insulating LEC GaAs. This finding has led to the development of a quantitative model for the compensation mechanism. The purpose of this paper is to give a detailed account of these experimental results and interpretations. In the first section of the paper it is shown that the resistivity is controlled by the melt stoichiometry. The second section describes the identification of the predominant chemical impurities and electrically

active centers in the semi-insulating material. The compensation model is developed in the third section.

## II. APPARATUS AND PROCEDURES

The crystals used in this study were grown in the  $\langle 100 \rangle$  direction from pyrolytic boron nitride (PBN) crucibles using a "Melbourn" high pressure (Metals Research, Ltd.) crystal puller. The pressure of the argon ambient during growth was 300 psi. All of the crystals were undoped. The crystal weight and diameter were typically 2.5 Kg and 3 in., respectively. Nominally dry ( $< 500$  ppm  $H_2O$ )  $B_2O_3$  encapsulating material (Johnson Matthey) was used for all growth experiments. The melt was prepared by in situ [7] synthesis, to achieve high purity, starting with a charge of 6-9's As (Cominco) and 6-9's Ga (Kawecki). The composition of the melt was varied by changing the relative amounts of Ga and As in the initial charge. The composition of the initial melt was determined by adjusting the charge composition for the amount of As lost [6] during the heat-up cycle. The weight of lost As was determined by comparing the weight of the initial charge to the weight of the crystal and the charge remaining in the crucible after growth. The  $B_2O_3$  was carefully separated from the charge remaining in the crucible before weighing to eliminate possible errors introduced by  $B_2O_3$  evaporation. Samples for characterization were obtained from along the length of each crystal. The melt composition corresponding to the growth of each sample was determined by adjusting the initial melt composition for the crystal weight at the time of growth. The crystal weight and length were recorded during the growth as a function of time. After terminating the growth process, the crystals were cooled at between 30 and  $80^\circ C\ hr^{-1}$ .

The concentration of background transition metal and group III-VI impurities was determined by secondary ion mass spectrometry [8] (SIMS). The



concentration of carbon (acceptors) was determined by localized vibrational mode (LVM) far-infrared [9] spectroscopy. The LVM absorption band for  $^{12}\text{C}$  occurs at  $582\text{ cm}^{-1}$ . The integrated absorption is proportional to the  $^{12}\text{C}$  concentration. The carbon concentration of our material was determined by measuring the absorption at 77K and converting to concentration by using the optical cross-section given in Ref. [9]. The free carrier concentration, Hall mobility, and resistivity were determined by Van der Pauw-Hall effect measurements at room temperature and over a temperature range of from 298 to 400K. Optical absorption measurements in the near infrared were made at room temperature with a Perkin-Elmer Model 330 spectrometer. Photoluminescence measurements [10] were made at 4.2K by immersing samples in liquid helium.

### III. STOICHIOMETRY-CONTROLLED RESISTIVITY

The electrical characteristics of the crystals were evaluated by Hall-effect measurements using samples obtained from the fronts and tails of the twelve crystals, and from detailed resistivity profiles of five crystals. The resistivity was found to be a strong function of the melt stoichiometry, as shown in Fig. 1.

Figure 1 shows that the material is semi-insulating (n-type) above, and p-type (low resistivity) below a critical As concentration in the melt of about 0.475 As atom fraction. The resistivity peaks at the critical composition at a value of about  $1.5 \times 10^8\ \Omega\text{-cm}$  and decreases approximately 8 orders of magnitude below the critical composition. The resistivity also decreases very gradually as the As fraction increases from the critical composition.

The variation in resistivity across the melt composition range is explained in terms of the corresponding free carrier concentration and Hall mobility, as shown in Figs. 2 and 3. The semi-insulating material grown at the



critical composition is n-type with a carrier concentration and mobility of  $1-2 \times 10^7 \text{ cm}^{-3}$  and  $1-2 \times 10^3 \text{ cm}^2 \text{ V}^{-1} \text{ s}^{-1}$ , respectively. These Hall mobilities are low for n-type GaAs possibly indicating the presence of inhomogeneities in the material. As the As atom fraction increases from the critical composition to about 0.51, the mobility gradually increases to  $4-5 \times 10^3 \text{ cm}^2 \text{ V}^{-1} \text{ s}^{-1}$ , which is more typical of n-type material. The corresponding electron concentration gradually increases to  $6-8 \times 10^7 \text{ cm}^{-3}$ . The combined increase of both the mobility and carrier concentration lead to a reduction in resistivity of about one order of magnitude. A further change in the As fraction from 0.51 to about 0.54 brings about a more pronounced increase in free carrier concentration of about 2 orders of magnitude. The result is a corresponding decrease in resistivity to as low as  $1.5 \times 10^5 \Omega\text{-cm}$ .

The material becomes p-type below the critical composition. The free hole concentration rises approximately 9 orders of magnitude following a 1% reduction in As fraction in the melt from the critical composition. The hole concentration and Hall mobility of this material are in the range of  $1-3 \times 10^{16} \text{ cm}^{-3}$  and  $215-330 \text{ cm}^2 \text{ V}^{-1} \text{ s}^{-1}$ , respectively. Mobilities obtained from the p-type material grown in the transition region, corresponding to melt compositions within about 1% of the critical composition, were very low, between 1 and  $30 \text{ cm}^2 \text{ V}^{-1} \text{ s}^{-1}$ . The measured hole concentrations were between about  $1 \times 10^{10}$  and  $2 \times 10^{14} \text{ cm}^{-3}$ . These carrier concentrations are too high to explain the low mobilities in terms of mixed conduction. The low mobilities of material grown in the transition region could reflect inhomogeneities in the material. For instance, a striated pattern of regions of high and low resistivity could cause such behavior.

Detailed resistivity profiles of crystals grown from initially As- and Ga-rich melts further emphasize the role of the melt stoichiometry in controlling



the electrical compensation. It is important to note that unless the initial melt is precisely stoichiometric [11], As-rich (Ga-rich) melts become progressively more As-rich (Ga-rich) as the crystal is pulled from the melt. Crystals grown from As-rich melts were invariably semi-insulating from front to tail. Crystals grown from Ga-rich melts initially below the critical composition were p-type throughout. On the other hand, crystals grown from Ga-rich melts initially above the critical composition underwent a transition from semi-insulating to p-type at the point along the crystal where the corresponding melt composition reached the critical value. This behavior clearly indicates that the resistivity is controlled by the melt stoichiometry, and, that the semi-insulating-to-p-type transition is not related to the normal segregation of some common background impurity toward the tail of the crystal. Otherwise, the tail of As-rich-grown crystals would have become p-type as well.

#### IV. ANALYSIS OF CHEMICAL IMPURITIES AND ELECTRICALLY ACTIVE CENTERS

To establish a model for the compensation mechanism in undoped semi-insulating LEC GaAs, the chemical impurities and electrically active centers were evaluated. The chemical impurities, as determined by SIMS and LVM, are shown in Table I. These results represent an average of measurements obtained from the front and tail of each of the twelve crystals. A range of concentrations is reported for those elements which exhibited substantial concentration variations from crystal to crystal. Carbon, as determined by LVM, is the predominant, chemically identifiable, electrically active background impurity. The concentration of carbon ranged from  $2 \times 10^{15}$  to  $1.3 \times 10^{16} \text{ cm}^{-3}$ . The concentration of the other background impurities common to GaAs, such as S, Mg, Cr, Mn, and Fe, is very low. In particular, the Si concentration is consistently less than about  $1 \times 10^{15} \text{ cm}^{-3}$  as determined by SIMS measurements. Low Si contamination results



from crystal growth without a quartz crucible. Si levels in this material are more than one order of magnitude lower than in Bridgman material that was analyzed. Boron is present in a range from about  $1 \times 10^{16}$  to  $6 \times 10^{17} \text{ cm}^{-3}$ . The source of boron contamination is the  $\text{B}_2\text{O}_3$  encapsulant. The incorporation of boron has been shown [12] to depend on the water content of the encapsulant, decreasing as the water content increases. Although boron is the predominant chemical impurity, it is iso-electronic with Ga, and no evidence was found in this study indicating that boron is electrically active.

The evaluation of the electrical and optical properties of the semi-insulating material indicates that the deep donor, commonly referred to as EL2, is the predominant deep center. An optical absorption band between 1 and  $1.4 \mu\text{m}$  previously identified with the EL2 center [13] was observed in all of the semi-insulating material. In addition, the activation energy of the electron concentration, obtained from plots of the temperature-corrected free electron concentration as a function of the reciprocal of temperature, was  $0.75 \pm 0.02 \text{ eV}$ . This energy is consistent with published values [14] for the activation energy of EL2. The behavior of the photoconductivity thresholds [15] above and below 120K was also found to be consistent with the presence of EL2.

The concentration of EL2 was determined by optical absorption using the cross-section reported by Martin et al. [16]. Absorption due to unoccupied EL2 centers was not observed, and the Hall measurements indicated that the center was more than 90% occupied. Consequently, the absorption was taken to be proportional to the total EL2 concentration. The concentration of EL2 was found to depend on the melt stoichiometry, as shown in Fig. 4, increasing from about  $5 \times 10^{15}$  to  $1.7 \times 10^{16} \text{ cm}^{-3}$  as the As atom fraction increased from about 0.48 to 0.51. The concentration remained constant as the As fraction increased further to about 0.535.

Photoluminescence (PL) studies of the semi-insulating material are consistent with the measured dependence of EL2 on melt stoichiometry. Typical PL spectra of semi-insulating material grown from Ga- and As-rich melts, shown in Fig. 5, exhibit bands peaking at 0.68 and 0.77 eV. The 0.68 eV band has been attributed [10] to radiative-recombination between EL2 electron traps and the valence band, and the 0.77 eV band to recombination possibly associated [10] with a hole trap. The intensity of the 0.68 eV band in the semi-insulating GaAs grown from Ga-rich melts is substantially reduced by comparison with As-rich grown material. This behavior is consistent with the decrease of the EL2 concentration with decreasing As fraction (Fig. 4) as determined by optical absorption. Neither band was observed in the p-type material.

#### V. THE COMPENSATION MECHANISM

To develop a model for the electrical compensation in terms of the concentration of a predominant electrically active centers in the semi-insulating material, the concentration of shallow and deep centers were related through first-principle theoretical considerations. The ionization of EL2 produces an ionized center plus an electron in the conduction band;



According to the principle of detailed balance, the concentration of ionized centers  $N_I$ , the concentration of electrons  $n$ , and the concentration of unionized centers  $N_U$ , are related by the following equation;

$$\frac{N_I n}{N_U} = K \quad (2)$$

where  $K$  is a constant determined by the thermodynamics of the system.  $N_I$  is equal to the net acceptor concentration, given as the difference in concentration

between shallow acceptors,  $N_A$ , and shallow donors,  $N_D$ ;

$$N_I = N_A - N_D \quad . \quad (3)$$

The concentration of acceptors is given as the sum of the concentrations of carbon and other residual acceptors,  $N_A^R$ ;

$$N_A = [\text{carbon}] + N_A^R \quad . \quad (4)$$

The concentration of unionized centers is equal to the EL2 concentration as determined by optical absorption. That is, only EL2 centers which are occupied by electrons contribute to the optical absorption process;

$$N_U = \text{EL2} \quad . \quad (5)$$

By substituting Eqs. (3) through (5) into Eq. (2), the following expression for the free-electron concentration is obtained in terms of the predominant centers in the material;

$$n = K \frac{\text{EL2}}{([\text{carbon}] + N_A^R - N_D)} \quad . \quad (6)$$

This expression can be rewritten in the following form:

$$[\text{carbon}] = K \frac{\text{EL2}}{n} + N_D - N_A^R \quad . \quad (7)$$

Therefore, the carbon concentration is proportional to the ratio of the EL2 concentration to the electron concentration.

Semi-insulating material grown from melts ranging from 0.475 to 0.535 As atom fraction was evaluated according to Eq. (7) from measurements of the carbon concentration (by LVM), the EL2 concentration (by optical absorption), and the



electron concentration (by Hall effect measurements) for each sample. A plot of the carbon concentration as a function of the ratio of the EL2 concentration to the electron concentration, shown in Fig. 6, follows linear behavior, indicating that the electron concentration is indeed controlled by the balance between EL2 and carbon. This result is independent of possible errors in the published values of the optical cross-sections for carbon and EL2. It is important to note that if some other impurity were the predominant acceptor, such as Mn, Fe, Cu, or Zn, the linearity predicted on the basis of Eq. (7) would still necessarily hold. However, the linearity would not be distinguishable because the term [carbon] would be small compared to  $N_A^R$ ; the figure would be a scatter plot. In fact, the scatter in these data probably reflects actual fluctuations in the concentration of other background impurities rather than random error in the experimental measurements. The small value of the intercept ( $N_D - N_A^R$ ) of the least-squares fit to the data also indicates the predominance of carbon acceptors. Thus, EL2 deep donors and carbon acceptors control the electrical compensation in semi-insulating LEC GaAs grown from melts ranging from 0.475 to 0.535 As atom fraction.

The variation of the electrical characteristics of the semi-insulating material (Figs. 1-3) with melt stoichiometry can now be explained on the basis of the analysis above. The EL2 concentration must either exactly match or exceed the carbon concentration to produce semi-insulating properties. The EL2 concentration in material grown from Ga-rich melts below the critical composition is insufficient to compensate the carbon, leading to p-type conductivity. Semi-insulating material grown at the critical composition is closely compensated, leading to the maxima of the resistivity. As the As atom fraction in the melt increases from the critical composition to about 0.51, the EL2 concentration becomes progressively higher than the carbon concentration. As a result, thermal

ionization of (unionized) EL2 centers (see Eq. (1)) gives rise to a gradual increase in the electron concentration and a corresponding decrease in the resistivity (Figs. 1 and 2). Our model further shows that the relatively low resistivity of semi-insulating material grown from melts between 0.53 and 0.54 As atom fraction is due to exceptionally low concentrations of carbon acceptors.

## VI. SUMMARY AND CONCLUSIONS

It was shown that the melt stoichiometry controls the compensation in undoped GaAs grown by the liquid encapsulated Czochralski technique. The free carrier concentration of the semi-insulating material is controlled by the balance between EL2 donors and carbon acceptors. The incorporation of EL2 depends on the melt stoichiometry, increasing as the As melt concentration increases. As a result, semi-insulating material can be grown only above a critical As concentration.

From a fundamental standpoint, these results have provided the first direct evidence indicating that the identity of the EL2 center is associated with a native defect or native-defect complex in bulk GaAs: LEC GaAs is pure enough to reveal the contribution of native-defects in bulk material. The dependence of EL2 on melt stoichiometry is consistent with published work on GaAs grown by vapor phase epitaxy [17] and organometallic chemical vapor deposition [18]. Isolated native defects which would follow the stoichiometry dependence of EL2 (Fig. 4) include the gallium vacancy  $V_{Ga}$ , the arsenic interstitial  $As_i$ , and the antisite  $As_{Ga}$ . Since  $V_{Ga}$  would be expected to be an acceptor, EL2 would more likely be related to one of the latter two defects. There is evidence [10,19-24] supporting either defect, and we believe that further work on well characterized material is needed to make a definitive assignment of EL2.

In practical terms, these results show that semi-insulating GaAs can be grown by the LEC technique reproducibly and with high yield provided that the melt is As-rich. This condition ensures that the melt will not become Ga-rich during the growth process. Indeed, nine crystals grown during the course of this investigation from near-stoichiometric As-rich melts were semi-insulating from front to tail. In addition, the characteristics of Se active layers implanted directly into the substrates showed excellent uniformity [25] of the pinch-off voltage across each wafer. These results demonstrate that high yield and reproducibility can be achieved in both the growth of GaAs by the LEC technique and in the application of LEC GaAs to the integrated circuit technology.

#### ACKNOWLEDGMENT

The authors are grateful to Dr. Peter Asbeck for his advice and many helpful discussions during the course of this work. We are indebted to Mr. Jeff Dreon for his assistance in crystal growth and sample preparation. We also appreciate the assistance of Dr. Jane Yang in making the variable temperature Hall measurements. We wish to thank the National Aeronautics and Space Administration/Army for partially supporting this work under contract No. NAS3-22224. We also acknowledge the support of the Air Force in making the photoluminescence measurements under contract No. F33615-81-C-1406.





## REFERENCES

1. P.M. Asbeck, J. Tandon, B.W. Welch, C.A. Evans Jr., and V.R. Deline, IEEE Electron. Dev. Lett., EDL-1, p. 35, 1980.
2. E.M. Swiggard, S.H. Lee, and F.W. Von Batchelder, Inst. Phys. Conf. Ser. No. 33b, p. 23, 1977.
3. R.D. Fairman, R.T. Chen, J.R. Oliver, and D.R. Ch'en, IEEE Trans. Electron. Dev., ED-28, p. 135, 1981.
4. H.M. Hobgood, G.W. Eldridge, D.L. Barrett, and R.N. Thomas, IEEE Trans. Electron. Dev., ED-28, p. 140, 1981.
5. C. Kocot and C. Stolte, "Backgating in GaAs MESFETs," presented at the GaAs IC Symposium, San Diego, CA, 1981, unpublished.
6. D.E. Holmes, R.T. Chen, K.R. Elliott, and C.G. Kirkpatrick, Appl. Phys. Lett., vol 40, p. 46, 1982.
7. T.R. AuCoin, R.L. Ross, M.J. Wade, and R.D. Savage, Solid-State Technol., vol 22, p. 59, 1979.
8. Charles Evans and Associates, San Mateo, CA. Cu determined by SSMS.
9. M.R. Brozel, J.B. Clegg, and R.C. Newman, J. Phys. D. Appl. Phys., vol 11, p. 1331, 1978.
10. P.W. Yu, D.E. Holmes, and R.T. Chen, Int. Symp. on GaAs and Related Compounds, Oiso, Japan, 1981.
11. The small differences between the stoichiometric and congruent melting compositions is neglected.
12. J.R. Oliver, R.D. Fairman, and R.T. Chen, Electron. Lett., vol 17, p. 839, 1981.
13. G.M. Martin, "Semi-insulating III-V Materials," Nottingham, p. 13, 1980.



14. G.M. Martin, J.P. Farges, G. Jacob, and J.P. Hallais, J. Appl. Phys., vol 51, p. 2840, 1980.
15. A.L. Lin, E. Omelianovsk, and R.H. Bube, J. Appl. Phys., vol 47, p. 1852, 1976.
16. G.M. Martin, G. Jacobs, A. Goltzene, and C. Schwab (Proceedings of the 11th Int. Conf. on Defects and Radiation Effects in Semiconductors, Oiso, Japan, 1980).
17. M.D. Miller, G.H. Olsen, and M. Ettenberg, Appl. Phys. Lett., vol 32, p. 538, 1977.
18. P.K. Bhattacharya, J.W. Ku, S.J.T. Owen, V. Aebi, C.B. Cooper, and R.L. Moony, Appl. Phys. Lett., vol 36, 304, 1980.
19. H.C. Gatos, private communication.
20. V.T. Bublik, V.V. Karataev, R.S. Kulagin, M.G. Mil'vidski, V.B. Osvenski, O.G. Stolyarov, and L.P. Kholodnyi, Sov. Phys. Crystallogr., vol 18, p. 218, 1973.
21. A.F.W. Willoughby, C.M.H. Driscoll, and B.A. Bellamy, J. Mater. Sci., vol 6, p. 1389, 1971.
22. D.T.J. Hurle, J. Phys. Chem. Solids, vol 40, p. 613, 1979.
23. J.A. Van Vechten, J. Electrochem. Soc., vol 122, p. 419, 1975.
24. Ibid, p. 423.
25. P.M. Asbeck, C.G. Kirkpatrick, M.J. Sheets, E.J. Babcock, B.M. Welch, and R. Zucca, "Reproducibility of FET Channel Implants for GaAs Digital ICs," presented at the GaAs IC Symposium, San Diego, CA, 1981, unpublished.

FIGURE CAPTIONS

Fig. 1 Dependence of electrical resistivity of LEC GaAs on melt stoichiometry. Semi-insulating material is obtained above, and p-type (low-resistivity) material below a critical melt composition of about 0.475 As atom fraction.

Fig. 2 Dependence of free carrier concentration of LEC GaAs on melt stoichiometry. The semi-insulating material is n-type, and the free electron concentration increases gradually as the As concentration in the melt increases from the critical composition. The material becomes p-type below the critical composition. The free carrier concentration rises approximately 9 orders of magnitude following a 1% reduction in As fraction from the critical composition.

Fig. 3 Dependence of Hall mobility of LEC GaAs on melt stoichiometry. The mobility of the semi-insulating material varies from  $1-2 \times 10^3$  to  $4-5 \times 10^3 \text{ cm}^2 \text{ V}^{-1} \text{ s}^{-1}$  as the As atom fraction increases from the critical composition to about 0.535. The mobility of the p-type material grown in the transition region, within about 1% of the critical composition, is low, between  $1-30 \text{ cm}^2 \text{ V}^{-1} \text{ s}^{-1}$ . The mobility of the p-type material grown outside of the transition region ranges from 215 to 330  $\text{cm}^2 \text{ V}^{-1} \text{ s}^{-1}$ .



Fig. 4 Dependence of EL2 concentration as determined by optical absorption on the melt stoichiometry. The concentration of EL2 increases from  $5 \times 10^{15} \text{ cm}^{-3}$  to  $1.7 \times 10^{16} \text{ cm}^{-3}$  as the As atom fraction increases from about 0.48 to 0.51, and appears to saturate as the As concentration increases further to 0.53.

Fig. 5 Typical photoluminescence spectra of semi-insulating GaAs grown from (a) an As-rich melt (As atom fraction = 0.507,  $\rho = 1.8 \times 10^7 \text{ } \Omega\text{-cm}$ ) and (b) a Ga-rich melt (As atom fraction = 0.488,  $\rho = 1.4 \times 10^8 \text{ } \Omega\text{-cm}$ ). The intensity of the 0.68 eV band decreases as the As atom fraction decreases toward the critical composition consistent with the optical absorption measurements (Fig. 4).

Fig. 6 Dependence of the carbon concentration on the ratio of the EL2 concentration to the electron concentration. The concentration of carbon, EL2, and electrons was determined for each sample. The dashed line is a least-square fit to the data. The linearity of the data indicates the dominant roles played by EL2 deep donors and carbon acceptors in controlling the compensation (see text). The small value of the intercept ( $N_D - N_A^R$ ) also indicates the predominance of carbon acceptor.



**Rockwell International**

## **LIST OF TABLES**

**Table I. Chemical impurity analysis of 12 LEC GaAs crystals.**



ORIGINAL PAGE IS  
OF POOR QUALITY

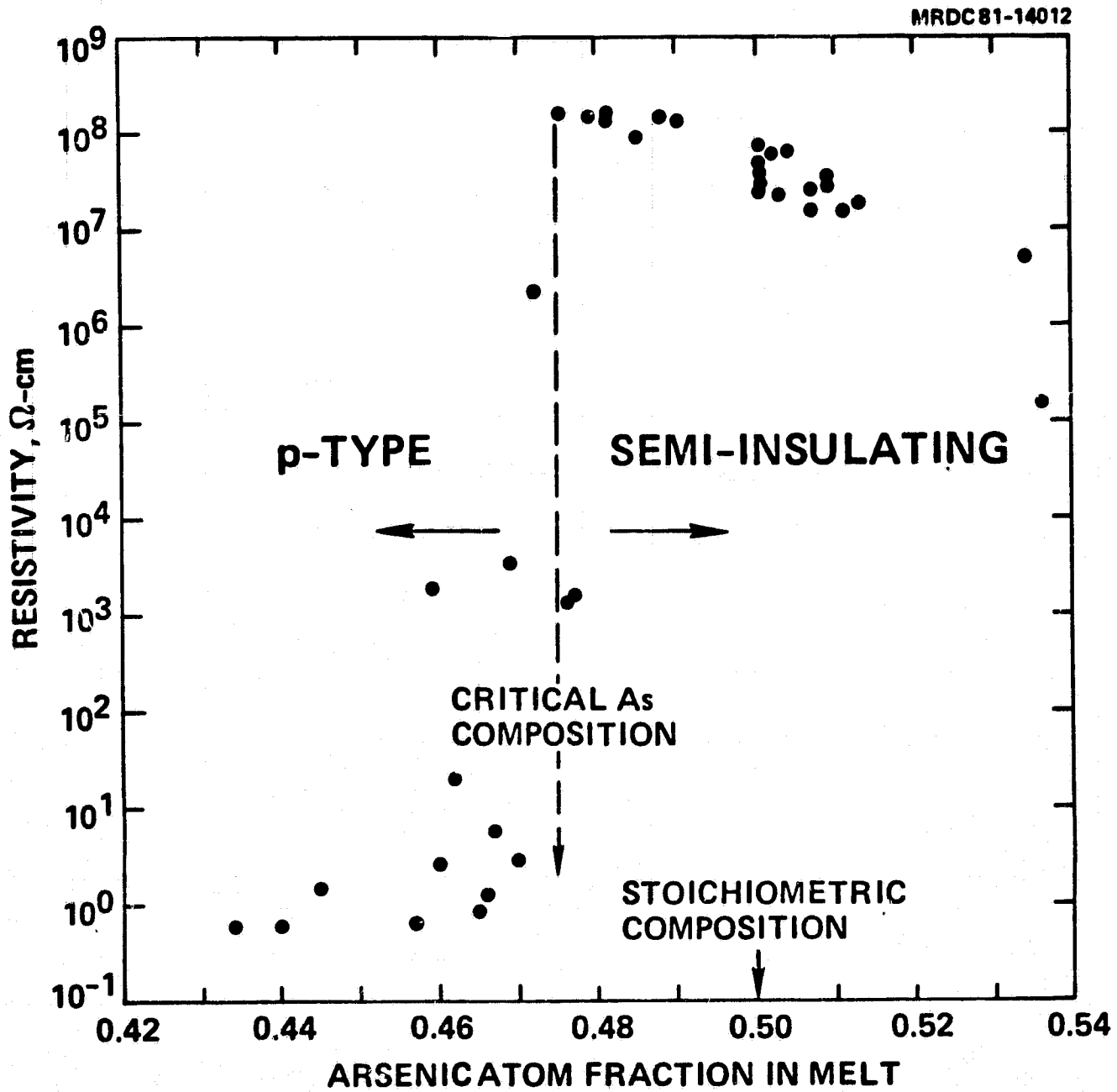


FIGURE 1



ORIGINAL PAGE IS  
OF POOR QUALITY.

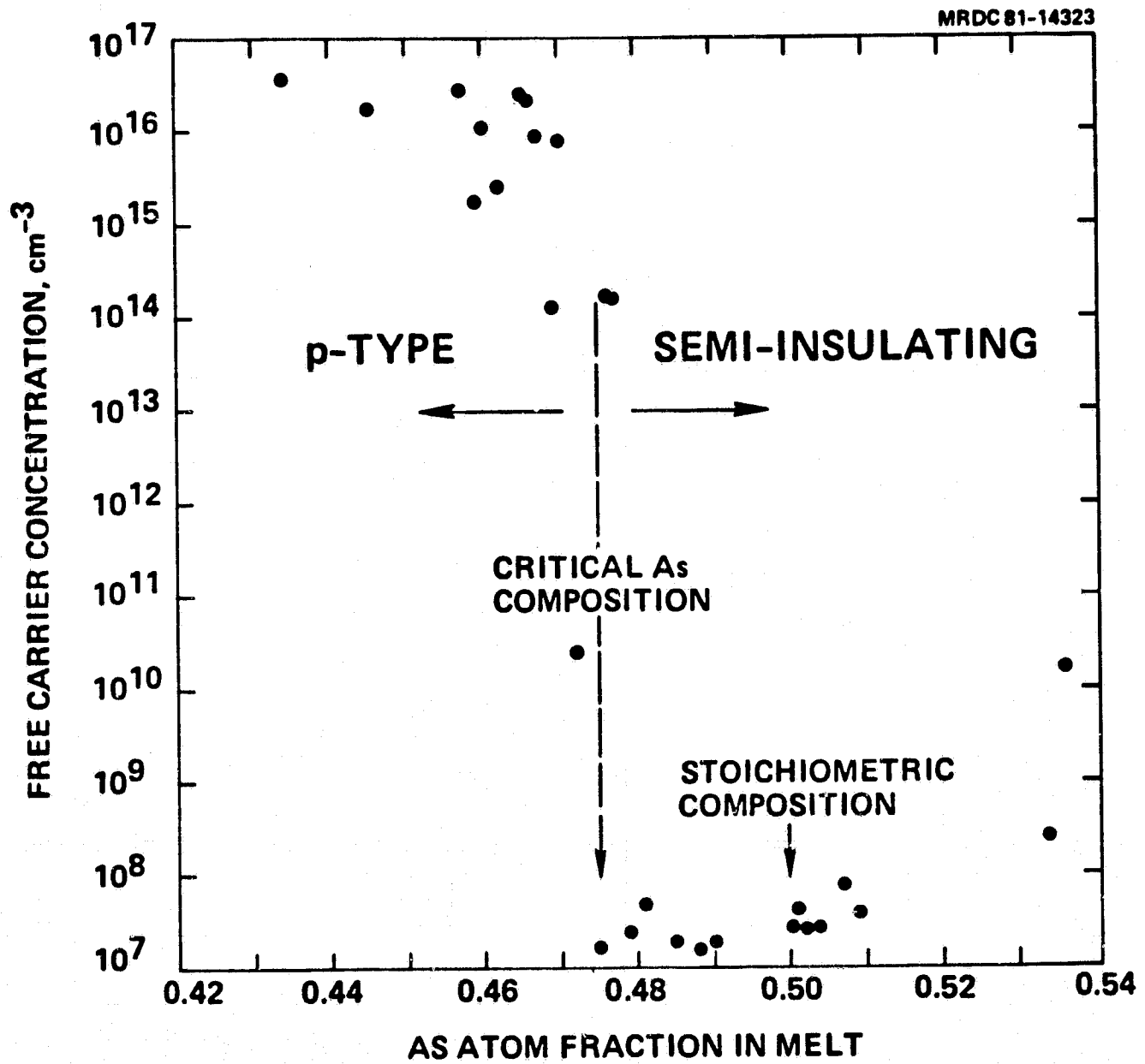


FIGURE 2



ORIGINAL PAGE IS  
OF POOR QUALITY

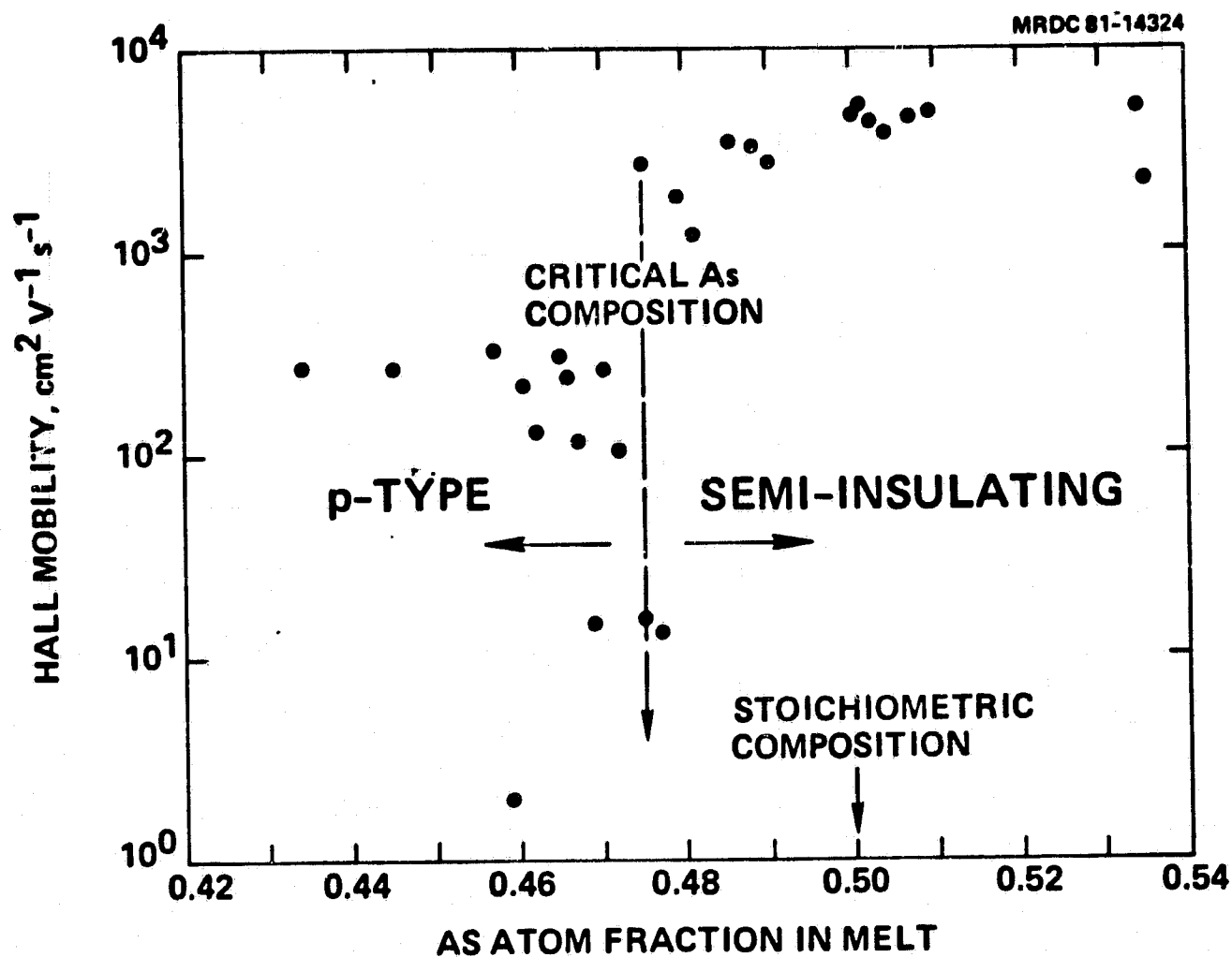


FIGURE 3





ORIGINAL PAGE IS  
OF POOR QUALITY

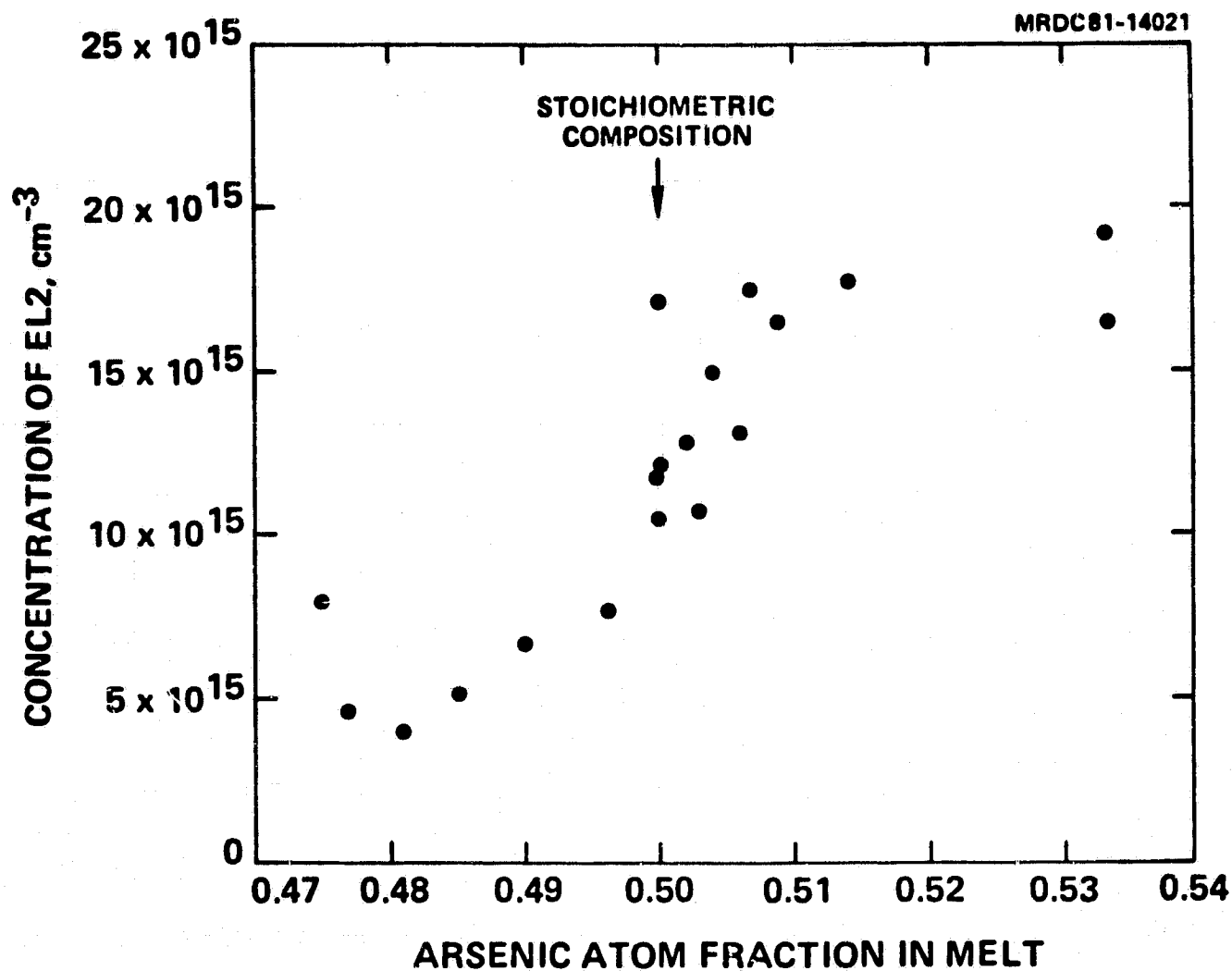


FIGURE 4



ORIGINAL PAGE IS  
OF POOR QUALITY

MRDC81-15715

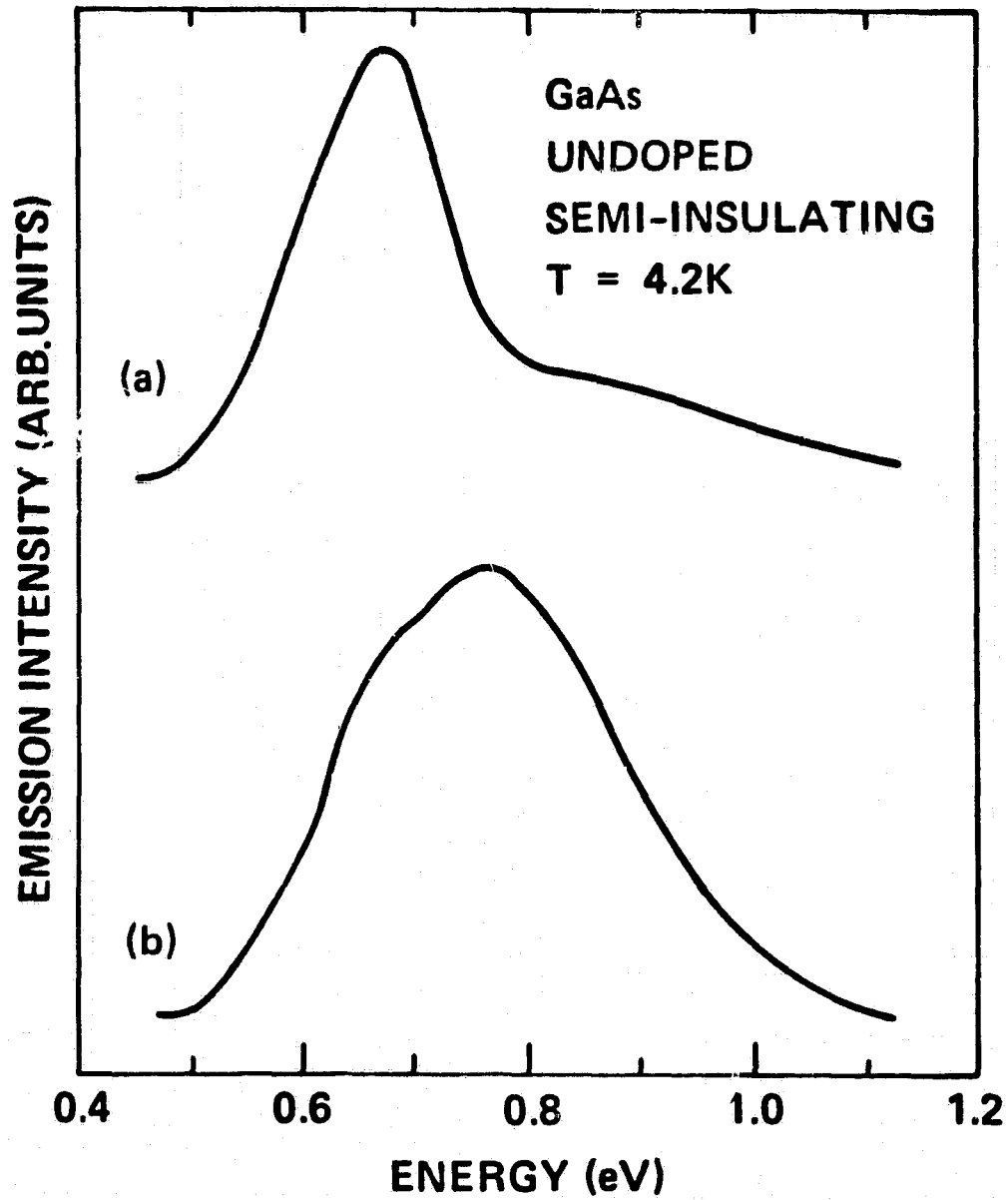


FIGURE 5



ORIGINAL PAGE IS  
OF POOR QUALITY

MRDC81-14023

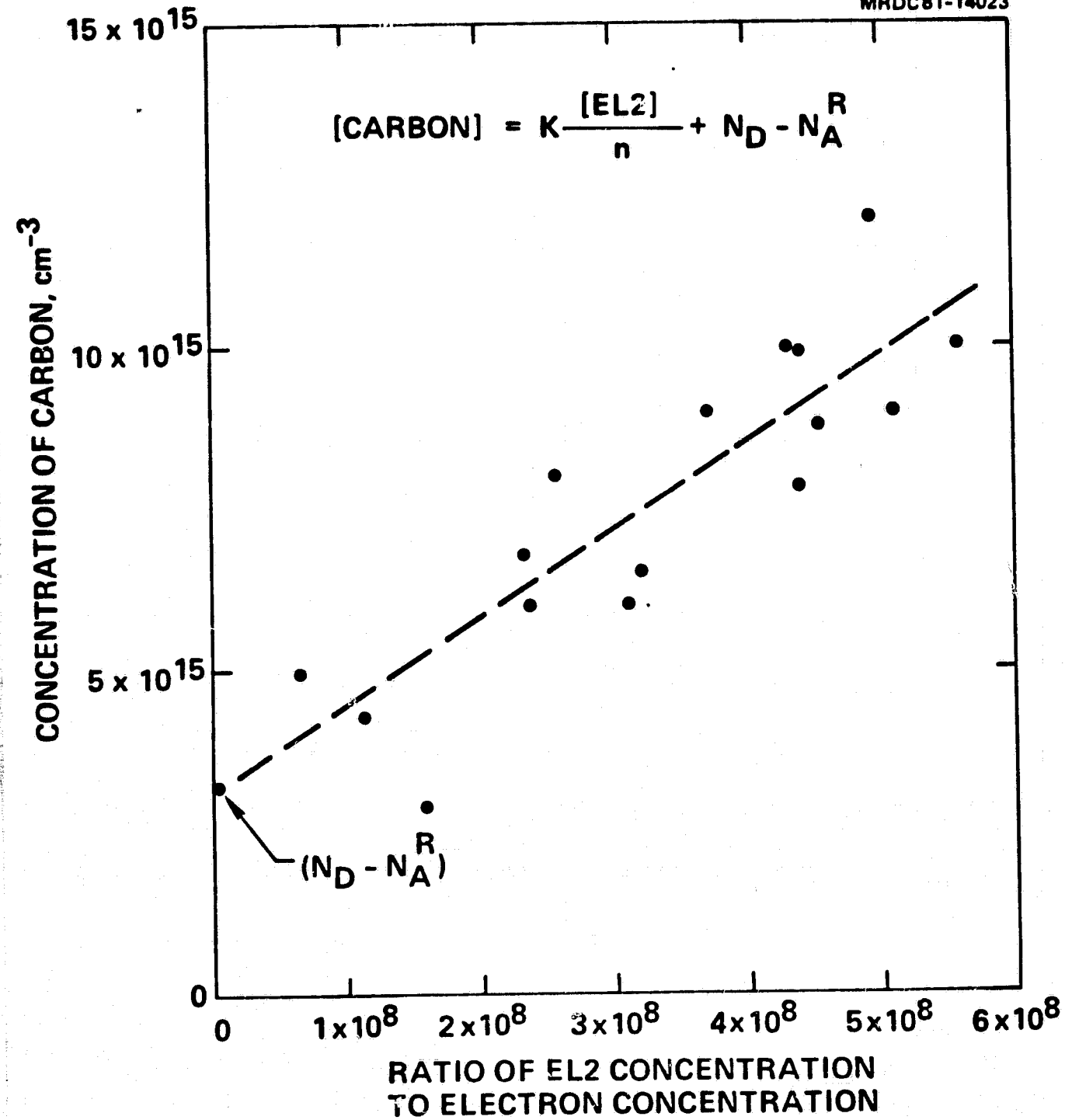


FIGURE 6

**Table I**  
**Chemical Impurity Analysis of LEC GaAs Crystals**

AVERAGE* CONCENTRATION (cm <sup>-3</sup> )	IMPURITY									
	S	Se	Te	Mg	Cr	Mn	Fe	Cu	Si	B
	1.1e15	<5e14	<5e13	2e14	<5e14	<1e15	<3e15	<9e14	<1e15	1-5e16
										2.1-12e15

\* 12 CRYSTALS ANALYZED

≠ CARBON DETERMINED BY LVM



### 9.3 APPENDIX III

To be published in J. of Crystal Growth



DISLOCATION STUDIES IN 3-INCH DIAMETER  
LIQUID ENCAPSULATED CZOCHRALSKI GaAs

R. T. Chen and D. E. Holmes

Rockwell International  
Microelectronics Research and Development Center  
Thousand Oaks, California 91360

ABSTRACT

We have characterized the density and distribution of dislocations in 3-inch diameter, undoped GaAs crystals grown by the liquid encapsulated Czochralski technique. The radial distribution across wafers follows a "W"-shaped profile indicating excessive thermal gradient-induced stress as the primary cause of dislocations. The density along the body of each crystal increases continuously from front to tail. In contrast, the longitudinal distribution in the cone region is inverted, first increasing, and then decreasing as the crystal expands from the neck to full diameter. Growth parameters favoring reduced dislocation densities include good diameter control, the use of thick  $B_2O_3$  encapsulating layers, slightly As-rich melts, and low ambient pressures. The dislocation density in the body of the crystal is practically independent of cone angle  $\theta$  for  $20^\circ < \theta < 70^\circ$ . However, high densities result for flat-top ( $0^\circ < \theta < 20^\circ$ ) crystals. Dash-type seed necking works to reduce the dislocation density only when high-density seeds ( $> 5000 \text{ cm}^{-2}$ ) are used. Dislocation densities below  $1 \times 10^4 \text{ cm}^{-2}$  can be achieved routinely in the front of a crystal through proper control of these parameters. The lowest measured dislocation density was  $6000 \text{ cm}^{-2}$ . Further, we show that convective heat transfer from the crystal to the high pressure ambient plays a dominant role in controlling the dislocation density.

## 1. INTRODUCTION

Current interest in large-diameter GaAs crystals grown by the liquid encapsulated Czochralski (LEC) technique [1,2] stems from the need for uniformly round substrates with stable, semi-insulating properties for digital and monolithic integrated circuits. As these circuits become larger and more complex, adverse effects of dislocations on device performance and reliability could appear. There have been virtually no systematic studies reported concerning the possible role of dislocations because of the early stage of development of GaAs integrated circuits. It is therefore important to characterize the density and distribution of dislocations across large-diameter substrates, and to establish how the density and distribution is controlled by the crystal growth process. This understanding is also important for the application of large-diameter LEC material to minority-carrier devices such as solar cells, where low dislocation densities are required to achieve high minority-carrier lifetimes and diffusion lengths.

A principal cause of dislocations in bulk GaAs crystals is stress induced by thermal gradients [3-6] during crystal growth. Radial gradients are of particular concern in Czochralski-type growth configurations (LEC, Grennelmaire). Most of the published dislocation studies on GaAs concern small-diameter (<0.5 inch-diameter) crystals grown by the LEC [7-9], Bridgman [10,11], and modified Grennelmaire [12] techniques. Since gradients generally decrease as the crystal diameter decreases, "effectively" dislocation-free, small-diameter GaAs crystals have been grown [7,9,11,12]. Growth parameters reported to reduce radial gradients in small-diameter LEC crystals include the

height of the  $B_2O_3$  encapsulating layer [7,13] and the cone angle [14]. Material properties which have been identified with the suppression of dislocations include the concentration of impurities [9,15,16] and melt stoichiometry [8,10,11]. To our knowledge, extensive dislocation studies of large-diameter LEC GaAs have not been published.

In this paper, we present and discuss results of dislocation studies involving undoped, 3-inch-diameter LEC GaAs crystals. We investigated the radial distribution across substrates, as well as the longitudinal distribution along the length of the crystals. The effects of cone angle,  $B_2O_3$  encapsulant thickness, ambient pressure, seed quality, Dash-type necking, diameter control, and melt stoichiometry were evaluated quantitatively. As a result of this effort, we showed that dislocation densities below  $10^4 \text{ cm}^{-2}$  can be achieved routinely through proper control of the crystal growth process. Dislocation densities as low as  $6000 \text{ cm}^{-2}$  are reported. Finally, techniques for possible further reductions in dislocation density are discussed.

## II. APPARATUS AND PROCEDURES

Eighteen undoped, 3-inch diameter GaAs crystals were grown during this study using a high pressure "Melbourn" (Metals Research Ltd.) puller. The crystals were grown in the  $\langle 100 \rangle$  direction from 6-inch-diameter quartz and pyrolytic boron nitride (PBN) crucibles. The  $B_2O_3$  encapsulant was obtained from Johnson-Matthey. The seeds were cut from Bridgman crystals and had dimensions of  $4 \text{ mm} \times 4 \text{ mm} \times 50 \text{ mm}$ . The GaAs melt was prepared by in situ synthesis [17] starting with a charge of high purity Ga (Kawecki) and As (Cominco) weighing 3 kg. The crystals weighed from 2.2 to 2.6 kg. The seed





and crucible were both rotated counter-clockwise at 6 and 15 rpm, respectively. The crystal pull rate was  $7 \text{ mm hr}^{-1}$ , and the crucible lift rate was  $1.4 \text{ mm hr}^{-1}$ . When the growth process was terminated, the crystal was positioned above the  $\text{B}_2\text{O}_3$  encapsulating layer, and the system was cooled at a constant rate of between 30 and  $80 \text{ }^\circ\text{C hr}^{-1}$ .

The diameter of the crystals was controlled manually by adjusting the temperature and cooling rate. Changes in temperature or cooling rate were made in response to variations of the differential weight of the crystal. The differential weight signal was provided by a "load cell," a weighing device on which the pull shaft was mounted. An increase or decrease of the differential weight indicated a corresponding expansion or contraction of the crystal. Growth was typically initiated by reducing the diameter of the crystal below that of the seed. This procedure is referred to as Dash-type seed necking [18]. The diameter was then allowed to expand controllably, forming the "cone." Expansion was terminated at the "shoulder," and the diameter of the crystal was held constant for the remainder of the growth process, forming the "body". Crucible lift was introduced during the growth of the shoulder.

The crystals were cut according to the diagram shown in Fig. 1. The samples were lapped and polished on both sides. Dislocation densities and distributions were evaluated by preferential etching (KOH for 25 min. at  $400^\circ\text{C}$ ). This etch attacks dislocations intersecting the surface of the sample, forming hexagonal etch pits. The etch pit density (EPD) corresponds directly to the dislocation density as confirmed by x-ray topography at our laboratory and elsewhere [19]. The EPD measurements were typically made from low-magnification (70X) micrographs by counting the pits over  $1.3 \times 1.0$ -millimeter



regions. However, higher magnification (either 140X or 280X) was required to resolve the pits when the EPD exceeded approximately  $1 \times 10^5 \text{ cm}^{-2}$ . The estimated error in counting the pits on each micrograph was less than 5%.

We investigated the effect of seven growth parameters on the dislocation density and distribution. These were: (1) cone angle, (2) seed quality, (3) seed necking, (4) diameter control, (5) melt stoichiometry, (6) height of the  $\text{B}_2\text{O}_3$  encapsulating layer, and (7) ambient pressure. The cone angle, defined as the angle between the wall of the cone and the horizontal, was varied from 0 to  $65^\circ$ . Crystals with a cone angle less than  $20^\circ$  are referred to as "flat-top" crystals. Referring to seed quality, the EPD of the seeds ranged from about  $1.5 \times 10^3$  to  $5 \times 10^5 \text{ cm}^{-2}$ . Crystals were grown with high and low EPD seeds with and without Dash-type necking. The neck diameter varied from 1.2 to 3 mm. Diameter control refers to the deviation of the diameter from the average value. We achieved our lowest diameter deviations ( $\pm 1.1 \text{ mm}$ ) by controlling the diameter with the cooling rate with minimal (direct) adjustments of the temperature. The initial melt stoichiometry was varied from 0.462 to 0.506 As atom fraction. Procedures necessary for making an accurate determination [20] of the melt composition have already been discussed. The height of the  $\text{B}_2\text{O}_3$  encapsulant above the melt was approximately 17 mm in the majority of the growth experiments, corresponding to 500 g of material. One experiment each was made with 170 and 390 g of  $\text{B}_2\text{O}_3$ , corresponding to 9 and 13 mm heights, respectively. The ambient pressure during growth was typically 300 psi. One experiment was conducted at a lower pressure of 50 psi.

### III. RESULTS AND DISCUSSION

#### 3.1 Radial Dislocation Distribution

The distribution of dislocations across wafers exhibited four-fold symmetry indicative of the  $\langle 100 \rangle$  crystallographic orientation, as shown in Fig. 2. A microscopic view of the dislocation distribution across wafers, as shown in Fig. 3, clearly shows large variations in EPD. The main features of the distribution are: (1) minimum EPD occurs over a large annulus between the center and edge (Region 1, or "ring" region); (2) intermediate EPD occurs in the center (Region 2, or "center" region); (3) maximum EPD occurs at the edge (Region 3, or "edge" region). In addition, the EPD in the ring and edge regions is greater along the  $\langle 100 \rangle$  than the  $\langle 110 \rangle$  direction (see Fig. 3). Measured EPD distributions across the full diameter of wafers typically followed a "W"-shaped profile, as shown in Fig. 4.

Our experimentally determined radial EPD distributions are consistent with theoretical thermoelastic analyses of Czochralski crystals of Penning [3] and Jordan et al. [5,6]. Jordan calculated the total stress in the crystal in terms of twelve  $(111) \langle 110 \rangle$  slip systems. The dislocation density is assumed to be proportional to the total stress within an additive constant. Since the periphery of the crystal is cooler than the center as the crystal is pulled from the melt, the periphery and center are under tension and compression, respectively. The calculated stress is highest at the periphery, consistent with the experimental finding that the maximum EPD occurs in the "edge" region of our crystals. The calculated stress is lowest in the transition between regions of tension and compression, consistent with the fact that the lowest

measured EPDs occur in the "ring" region. The relatively high EPD measured along  $\langle 100 \rangle$  compared to along  $\langle 110 \rangle$  is explained in terms of the theory by the fact that more slip systems contribute to the total stress along  $\langle 100 \rangle$ . The agreement between theory and experiment indicates that radial gradient-induced stress is the principal cause of dislocations in our crystals. Our results also agree with other experimental studies [5] of (100) GaAs.

Variations in the nature of the radial distribution from the front to the tail of the crystal are discussed in Section 3.3.

### 3.2 Dislocation Networks: Polygonization

An important morphological feature of the microscopic dislocation distribution is the formation of etch pit networks. Two types of morphologies are observed. The first is a cellular network, shown in Figs. 2 and 3, where the dislocations form an interconnected network of cells with few dislocations within each cell. The approximate diameter of the cells is  $500 \mu\text{m}$ , corresponding to an EPD of  $2 \times 10^4 \text{ cm}^{-2}$ . The cell diameter decreases as the EPD increases ( $100 \mu\text{m}$  diameter corresponds to an EPD of about  $1 \times 10^5 \text{ cm}^{-2}$ ). When the EPD is less than about  $2 \times 10^4 \text{ cm}^{-2}$ , the morphology of the network takes on a lineage structure, where the etch pits form visible wavy lines. These lines extend from a few millimeters to more than one centimeter, and are oriented along  $\langle 110 \rangle$ , as shown in Fig. 2.

We believe that these dislocation networks form as a result of the polygonization process [21], where the dislocations re-align after solidification to reduce the strain energy of the crystal. The re-alignment probably



occurs by both climb and glide processes. In general, dislocations in zinc blend materials can undergo alignment into walls defined by (110) planes perpendicular to (111) slip planes. These walls would intersect (100) planes along  $\langle 110 \rangle$  directions, consistent with our observations. The cellular network, in effect, constitutes a high packing density of lineage structures where one dislocation may interact with several dislocation lines, forming interconnected networks.

### 3.3 Longitudinal Dislocation Distribution

The longitudinal variation (along the growth direction) of the dislocation density was examined by comparing radial distributions of wafers obtained from the front, middle, and tail of the crystals, as shown in Fig. 4. The EPD invariably increased from front to tail in each of the three regions, as shown in Table I, while the radial profiles remained "W"-shaped, as shown in Fig. 4. This behavior could indicate that the overall level of stress increased along the crystal, or that the dislocations multiplied after growth, or both. The average EPD increased from front to tail (see Table I) by a factor of 8, 7, and 1.5 in the "ring," "center," and "edge" regions, respectively. Further, the ratio of the EPD in the "center" to that in the "ring" region decreased from front to tail in the majority of the crystals, as shown in the table. These results show that the radial EPD distribution becomes more uniform toward the tail of the crystals even though the "W"-shaped profile persists.

### 3.4 Parameters Affecting Dislocation Density

In this section, we present and discuss our results concerning the quantitative dependence of the dislocation density on cone angle,  $B_2O_3$  thickness, ambient pressure, seed quality and necking, diameter control, and melt stoichiometry. The effect of each growth parameter was evaluated by determining the change of the EPD across each substrate as that parameter was independently varied. Since the EPD density in the "ring," "center," and "edge" regions represented local limits of the entire EPD distribution, we were able to characterize the entire distribution with these three EPD values. Only when all three of these EPD values either increased or decreased were conclusions drawn concerning the effect of that particular growth parameter. We believe that the spatial resolution of our measurements in the center and ring regions (averaging over  $1.3 \times 1.0$  mm areas) was sufficient to reflect true variations in the average dislocation density across wafers while minimizing contributions due to microscopic fluctuations in density associated with polygonization. However, since higher magnifications were used to determine the EPD near the edge of the crystals, we estimate that these measurements probably represent the true average EPD to within 50%. Therefore, measurements obtained from the center and ring regions were more sensitive indicators of actual EPD variations from crystal to crystal than measurements from the edge. In effect, we weighed the center and ring regions more heavily. (Since the center and ring measurements encompassed approximately 80% of the area of a substrate, the heavier weighting of the center and ring measurements seems justifiable from a practical standpoint.) The EPD value reported in the tables is an average of at least two measurements.

### 3.4.1 Cone Angle

We evaluated the effect of the cone angle on the dislocation density by comparing the EPD of full-diameter wafers cut from the front of each crystal. Our results, shown in Table II, show no correlation between cone angle and EPD for cone angles greater than about 25°. For example, crystals No. 9 and No. 10 were grown under very similar conditions in terms of the other six parameters evaluated in this paper. The only difference is in the cone angles, which are 30° and 62° for crystals No. 10 and No. 9, respectively. The data shows virtually no difference between the EPD values in the center and ring regions.

On the other hand, the EPD in the front of the flat-top crystal (No. 15) is in the low  $10^5 \text{ cm}^{-2}$  range, which is high compared to the other crystals. In addition, the longitudinal distribution is inverted along approximately the first half of the crystal, first decreasing from the front toward the tail before increasing again as in all the other crystals. We also observed that the crystal began to expand rapidly when the top of the crystal emerged from the  $\text{B}_2\text{O}_3$  encapsulating layer, leaving a bulge at a distance from the front of the crystal equal to the height of the  $\text{B}_2\text{O}_3$  layer. This behavior shows that the crystal experienced significant additional cooling when emerging from the  $\text{B}_2\text{O}_3$ , indicating that the convective heat transfer from the crystal to the ambient was large compared to the heat transfer to the liquid encapsulating layer. The increased cooling presumably raised the level of stress near the top of the crystal leading to the unusually high dislocation density.

Dislocation maps of longitudinal cross sections of cones (see Fig. 5) were analyzed to follow the dislocation density distribution along the growth direction for various cone angles. The "W"-shaped radial distribution observed across wafers was clearly visible in these samples, as shown in Fig. 5. However, the longitudinal EPD increased after the neck, reached a maximum value, and then decreased before the crystal reached full diameter. (We had anticipated a continuous increase in EPD in the cone region because the diameter expands continuously, and radial gradients typically increase as the diameter increases.) We found that the maximum value of the EPD decreases as the cone angle increases, as indicated in Fig. 5. A high concentration of slip traces was also observed in the cone region in crystals grown with low-angle cones. In addition, the maximum of the longitudinal EPD distribution was located directly below the neck in low-angle cones, and closer to the center of the high-angle cones, as is evident in Fig. 5.

The variation with cone angle of both the EPD at the maximum and the position of the maximum within the cone as the cone angle decreased from 65° to 30° is consistent with the behavior of the flat-top crystal; i.e., the maximum EPD occurred at the top of the flat-top crystal, and the EPD at the maximum was the highest of all our crystals. We therefore believe that the same mechanism controlled the dislocation density and distribution at the top of all of the crystals, the flat-top crystal representing the limiting case of a 0° cone angle. In view of our discussion earlier in this section concerning the flat-top crystal, we further believe that the dislocation maximum formed as the cone emerged from the  $B_2O_3$  encapsulating layer as a result of increased convective heat transfer to the ambient. The dislocations associated with the





maximum represent a "secondary" distribution added to the primary ("grown-in") distribution, which formed at the solidification front.

Our study of the secondary dislocation distribution suggests the following model for the heat flow in the crystal at a position corresponding to the top surface of the encapsulating layer. The isotherm shape is determined by the relative vertical and radial components of heat flow. The vertical heat flow is relatively large when the crystal is thin (as the neck emerges from the  $B_2O_3$ ), and the isotherm shape is relatively flat. When the cone begins to emerge from the  $B_2O_3$ , radial heat flow becomes more important; the isotherm shape becomes more concave with respect to the solid as the radial gradient increases. The radial gradient increases as the cone angle decreases, leading to more pronounced EPD maximums for low-angle cones. As the vertical wall of the crystal begins to emerge from the encapsulating layer, the curvature of the isotherms and the radial gradients decrease.

#### 3.4.2 $B_2O_3$ Height

We evaluated the effect of the height of the  $B_2O_3$  encapsulating layer on the EPD by varying the height from 9 to 17 mm. The results in Table III show that the EPD decreases as the height of the layer increases. The effect is more pronounced at the front of the crystals. In addition, the nature of the secondary dislocation distribution in the cone region was independent of  $B_2O_3$  height. This behavior indicates that the radial gradients near the crystal-melt interface decrease as a direct result of the presence of a thicker  $B_2O_3$  layer. In view of the results of the previous section, which showed that the heat transfer from the crystal to the ambient (above the  $B_2O_3$ )



is greater than the heat transfer to the  $B_2O_3$  liquid, we believe that the reduction of the radial gradient in the crystal attributed to thicker  $B_2O_3$  layers results from more effective thermal isolation between the region of the crystal near the melt interface and the Ar ambient. This finding disagrees with theory [5], which predicts that the radial gradient would decrease as the  $B_2O_3$  height decreases.

### 3.4.3 Ambient Pressure

One crystal (No. 14) was grown at low pressure (50 psi). EPD measurements obtained from the front of the crystal are shown in Table IV. Excessive thermal degradation took place at the surface of the crystal due to the low ambient pressure. As a result, Ga droplets, which formed at the cone, thermally migrated through the crystal to the tail. The presence of the Ga in the crystal prevented the measurement of the EPD in the tail. The degradation, and subsequent loss of As from the crystal during growth, also prevented making an accurate determination of the melt stoichiometry. However, the electrical characteristics of the material indicated that both the initial and final melt compositions were within the As-rich range [20] similar to crystal No. 16. A comparison of the EPDs of the crystal grown at low pressure (No. 14) and crystal No. 16 shows that the EPD of crystal No. 14 was lower, as shown in Table IV, indicating that the use of lower ambient pressures is effective in reducing the EPD. In fact, the EPD of  $6000 \text{ cm}^{-2}$  in the ring region was the lowest value observed in this study.

The results reported in Sections 3.4.1 and 3.4.2 of this paper indicate the importance of convective heat transfer via the ambient in controlling the

dislocation density. The heat transfer coefficient of the crystal-ambient surface is expected to increase as the square root of the pressure according to Jordan [5,6]. Therefore, we could have expected a reduction in heat transfer coefficient by no more than a factor of 2.5 by reducing the pressure from 300 to 50 psi. Our experimental finding of a 50% reduction in EPD is consistent with the theoretical prediction.

#### 3.4.4 Seed Quality and Necking

We determined the effectiveness of the seed quality and the Dash-type necking procedure in reducing the EPD by growing crystals from high-and-low EPD seeds with and without thin necks. The crystals were evaluated by comparing the EPDs in the front of each crystal at full diameter. The results, given in Table V, show that low-EPD crystals ( $\text{EPD} < 2.5 \times 10^4 \text{ cm}^{-2}$ ) can be grown by employing low-EPD seeds with and without necking as well as by employing high-EPD seeds with necking.

To understand the effect of seed necking, we studied longitudinal cross sections of crystals in the neck region. We could not directly observe the grown-in EPD in this region with neck diameters of less than about 2.5 mm because the neck region apparently deformed under the weight of the crystal, as shown in Fig. 6(a). However, dramatic reductions in EPD were observed for necks between about 2.5 and 3.5 mm in diameter, as shown in Fig. 6(b). These results indicate that the Dash-type necking procedure indeed works to reduce the dislocation density independent of the EPD of the seeds. Yet, the effect was registered in the first full-diameter wafer only for high EPD seeds. We interpreted this behavior to mean that dislocations can be transmitted from



the seed to the crystal, and the transmission is reduced by necking. However, the effect of necking is limited; dislocations will be generated in the crystal even if the seed were perfectly dislocation free.

#### 3.4.5 Diameter Control

The effect of diameter control was evaluated by comparing the EPD of crystal tails. Our results, shown in Table VI, indicate that improved diameter control generally reduces the dislocation density. For example, crystals No. 6 and No. 9 were grown under very similar conditions, except that the diameter deviation was smaller in No. 6. The EPDs in the front of No. 6 are higher than in the front of No. 9, whereas the EPDs in the tail are lower. We attributed the lower EPD in the tail of No. 6 to the improved diameter control. We note that the effect of diameter control is much less pronounced compared to that of cone angle, seed quality, and seed necking. We believe that crystals with more unstable diameter control were subjected to greater transient gradient-induced stress, which resulted in higher EPDs.

#### 3.4.6 Melt Stoichiometry

We studied the effect of melt stoichiometry on the dislocation density by growing crystals from stoichiometric and non-stoichiometric melts. We found no correlation between EPD and melt stoichiometry for Ga- or As-rich melts with compositions less than 0.503 As atom fraction, as shown in Table VI. However, we note that the growth conditions and physical parameters of crystals No. 11 and No. 12 are nearly identical except for the melt composition. Yet, the EPD values in the front of crystal No. 11 are signifi-

cantly lower compared to crystal No. 12. The reduced EPD values in the front of the crystal would indicate that the As-rich melt favors reduced dislocation densities for melt compositions greater than about 0.505 As atom fraction. No significant improvement is apparent in the tail of No. 11, suggesting that a small range of melt compositions between 0.505 and 0.535 provides for optimal EPD reductions.

#### IV. SUMMARY AND CONCLUSIONS

We have characterized the density and distribution of dislocations in 3-inch diameter LEC GaAs crystals. The radial distribution across wafers is "W"-shaped, indicating excessive thermal gradient-induced stress as the primary cause of dislocations as predicted on the basis of the models of Penning [3] and Jordan et al. [5,6]. The dislocation density along the crystals increases from front to tail at full diameter, indicating that the level of stress in crystals grown in our current configuration increases as the crystal is pulled from the melt, or that the dislocations multiply after growth. The radial EPD distribution becomes more uniform toward the tail of the crystals even though the "W"-shaped distribution prevails. Jordan et al. [5] noted that a more "diffuse" radial dislocation distribution could result from the movement of 60-degree dislocations out of their slip planes into the next-to-grow layer of the crystal, adding to the glide dislocations at the solidification front. This explanation would seem to be a reasonable basis for modelling the observed behavior. However, such a model would have to take into account the fact that the increased uniformity of the dislocation density across 3-inch substrates is a very long-range process.



We have also evaluated the dependence of the dislocation density on seven crystal growth parameters. The EPD at full-diameter crystal is virtually independent of the cone angle  $\theta$  for  $20^\circ < \theta < 70^\circ$ . However, the EPD increases significantly for  $0^\circ < \theta < 20^\circ$ . Our analysis of the longitudinal dislocation distribution within the cone region further shows that the EPD inverts for  $20^\circ < \theta < 70^\circ$ , first increasing, and then decreasing from front to tail before the crystal expands to full diameter. We explained these findings in terms of the dominant role played by convective heat transfer from the crystal to the ambient gas as the crystal emerges from the  $B_2O_3$ . In practical terms, these results show that crystals can be grown with a minimum dislocation density using a cone angle of about  $30^\circ$ . The use of a  $30^\circ$  cone angle maximizes the number of low-dislocation wafers that can be obtained from crystals while minimizing the time required to grow the cone.

The dislocation density in the front of the crystals was found to be a relatively strong function of the height of the encapsulating layer, decreasing as the layer height increases. We showed that this effect is probably a direct result of reduced radial gradients in the crystal within the  $B_2O_3$  layer due to more effective insulation from the ambient gas.

We showed that the Dash-type seed necking procedure is effective in reducing the dislocation density only when the EPD of the seed is high ( $> 5000 \text{ cm}^{-2}$ ); low dislocation crystals were grown with poor quality seeds with necking, and with high quality seeds with and without necking. These results indicate that dislocations indeed transmit from the seed to the crystal, and necking greatly reduces this effect. However, the mechanism can have only a limited effect, as dislocations are generated in the crystal even

if the seeds were perfectly dislocation-free. We would expect that further reductions in the dislocation density in our crystals (achieved by altering the present thermal configuration) will require higher quality seeds if the necking procedure were to be eliminated from the growth process. The elimination of necking through careful selection of seeds would be advantageous from the practical standpoint of minimizing the time required to grow a crystal.

We have also found that good diameter control and the use of slightly As-rich melts favor reduced dislocation densities. However, these effects are small compared to those of the cone angle,  $B_2O_3$  height, seed quality and necking. Further work is needed to understand the effect of the melt stoichiometry.

Finally, the experimental results presented concerning the effect of cone angle,  $B_2O_3$  height, and ambient pressure indicate the importance of relatively high convective heat transfer at the crystal-ambient surface compared to the crystal- $B_2O_3$  surface. This finding disagrees with theoretical predictions of the relative heat transfer coefficients. The reconciliation of this discrepancy should be pursued to bring about a better understanding of the LEC crystal growth process and further reductions of the dislocation density.

## ACKNOWLEDGEMENTS

The authors are grateful to the National Aeronautics and Space Administration and the Army for partial support of this work under Contract No. NAS3-22224. The authors would also like to thank J. K. Dreon for this help in crystal growth and sample preparation, and to Dr. C. G. Kirkpatrick for her encouragement during the course of this study.

## REFERENCES

- [1] R. D. Fairman, R. T. Chen, J. R. Oliver and D. R. Ch'en, IEEE Trans. Electron Dev., ED-28 (1981) 135.
- [2] R. N. Thomas, H. M. Hobgood, G. W. Eldridge, D. L. Barrett and T. T. Braggins, Solid-State Electronics, 24 (1981) 387.
- [3] P. Penning, Philips Res. Repts., 13 (1958) 79.
- [4] M. G. Mil'vidskii and E. P. Bochkarev, J. Cryst. Growth, 44 (1978) 61.
- [5] A. S. Jordan, R. Caruso and A. R. Van Neida, Bell Syst. Tech. J., 59 (1980) 593.
- [6] A. S. Jordan, J. Cryst. Growth, 49 (1980) 631.
- [7] B. C. Grabmaier and J. G. Grabmaier, J. Cryst. Growth, 13/14 (1972) 635.
- [8] J. C. Brice, J. Cryst. Growth, 7 (1970) 9.
- [9] Yasuo Seki, Hisao Watanab and Junjii Matsui, J. Appl. Phys., 49 (1978) 822.
- [10] J. C. Brice and G. D. King, Nature, 209 (1966) 1346.



- [11] J. Parsey, Y. Namiski, J. Lagowski and H. C. Gatos, J. Electrochem. Soc., 128 (1981) 936.
- [12] A. Steinemann and U. Zimmerli, Proc. Int. Conf. Cryst. Growth, Boston, 1966 (Pergamon Press, New York, 1967) p. 81.
- [13] Seiji Shinoyama, Chika Uemura, Akio Yamamoto and Shun-ichi Tokno, Jap. J. Appl. Phys., 19 (1980) L331.
- [14] P. J. Roksnoer, J. M. P. L. Huijbregts, W. M. Van De Wijgert and A. J. R. De Kock, J. Cryst. Growth, 40 (1977) 6.
- [15] T. Suzuki, S. Akai, K. Kohe, Y. Nishida, K. Fujita and N. Kito, Sumitomo Electric Tech. Rev., 18 (1978) 105.
- [16] M. G. Mil'vidsky, V. B. Osvensky and S. S. Shifrin, J. Cryst. Growth, 52 (1981) 396.
- [17] T. R. Aucoin, R. L. Ross, M. J. Wade, and R. D. Savage, Solid-State Technol., 22 (1979) 59.
- [18] W. D. Dash, J. Appl. Phys., 28 (1957) 882.
- [19] J. Angilello, R. M. Potenski and G. R. Woolhouse, J. Appl. Phys., 46 (1975) 2315.
- [20] D. E. Holmes, R. T. Chen, K. R. Elliott, and C. G. Kirkpatrick, Appl. Phys. Lett., 40 (1982) 46.
- [21] R. E. Reed-Hill, Physical Metallurgy Principles (Van Nostrand, N.J. 2nd Edition, 1973) 274.

Table I. Summary of EPD Measurements on LEC Ingots

Ingot No.	Wafer Location	EPD (cm <sup>-2</sup> )			EPD Ratio (Center to Ring)
		(1) Ring	(2) Center	(3) Edge	
1 <sup>+</sup>	F	$7.6 \times 10^4$	$4.6 \times 10^4$	$3.0 \times 10^5$	0.6
	T	$6.1 \times 10^5$	$6.1 \times 10^5$	$1.1 \times 10^6$	1.0
2	F	$2.2 \times 10^4$	$5.0 \times 10^4$	$2.3 \times 10^5$	2.3
	M	$3.2 \times 10^4$	$7.3 \times 10^4$	$2.5 \times 10^5$	2.3
3	F	$4.0 \times 10^4$	$8.0 \times 10^4$	$2.9 \times 10^5$	2.0
	T	N/A	N/A	N/A	-
4 <sup>++</sup>	F	$4.0 \times 10^4$	$1.4 \times 10^5$	$4.0 \times 10^5$	3.5
	M	$3.0 \times 10^4$	$1.0 \times 10^5$	N/A	3.3
5	F	$1.5 \times 10^4$	$3.4 \times 10^4$	$1.7 \times 10^5$	2.3
	T	$1.2 \times 10^5$	$1.4 \times 10^5$	$2.1 \times 10^5$	1.2
6	F	$1.8 \times 10^4$	$2.6 \times 10^4$	$8.0 \times 10^4$	1.4
	T	$8.6 \times 10^4$	$7.7 \times 10^4$	$2.0 \times 10^5$	0.9
7	F	$1.0 \times 10^4$	$2.5 \times 10^4$	$5.6 \times 10^4$	2.5
	M	$2.5 \times 10^4$	$3.9 \times 10^4$	$7.8 \times 10^4$	1.6
8	F	$1.4 \times 10^4$	$3.7 \times 10^4$	$1.0 \times 10^5$	2.6
	T	N/A	N/A	N/A	-
9	F	$1.4 \times 10^4$	$2.0 \times 10^4$	$2.5 \times 10^5$	1.4
	T	$1.0 \times 10^5$	$1.0 \times 10^5$	$2.4 \times 10^5$	1.0



Table I (Continued)

Ingot No.	Wafer Location	EPD ( $\text{cm}^{-2}$ )			EPD Ratio (Center to Ring)
		(1) Ring	(2) Center	(3) Edge	
10	F	$1.0 \times 10^4$	$2.1 \times 10^4$	$1.1 \times 10^5$	1.9
	T	N/A	N/A	N/A	-
11	F	$7.5 \times 10^3$	$1.3 \times 10^4$	$1.9 \times 10^5$	1.7
	T	$8.1 \times 10^4$	$1.8 \times 10^5$	$1.8 \times 10^5$	2.2
12	F	$1.2 \times 10^4$	$1.7 \times 10^4$	$2.5 \times 10^5$	1.4
	T	$9.0 \times 10^4$	$1.0 \times 10^5$	$2.2 \times 10^5$	1.1
13	F	$3.5 \times 10^4$	$1.0 \times 10^5$	$1.5 \times 10^5$	2.9
	T*	$8.0 \times 10^4$	$1.1 \times 10^5$	$2.0 \times 10^5$	1.1
14	F	$6.0 \times 10^3$	$1.8 \times 10^4$	$9.6 \times 10^4$	3.0
	T	N/A	N/A	N/A	-
15 <sup>++</sup>	F	$1.1 \times 10^5$	$2.4 \times 10^5$	$2.7 \times 10^5$	2.2
	T	$1.3 \times 10^5$	$2.3 \times 10^5$	$1.6 \times 10^5$	1.8
16	F	$1.3 \times 10^4$	$2.8 \times 10^4$	$1.7 \times 10^5$	2.2
	T	$1.4 \times 10^5$	$2.2 \times 10^5$	$2.4 \times 10^5$	1.6
17	F	$1.1 \times 10^4$	$2.0 \times 10^4$	$1.1 \times 10^5$	1.8
	T	$1.5 \times 10^5$	$2.5 \times 10^5$	$1.7 \times 10^5$	1.7
18	F	$8.5 \times 10^3$	$1.6 \times 10^4$	$1.2 \times 10^5$	1.9
	T	$9.7 \times 10^4$	$1.3 \times 10^5$	$2.4 \times 10^5$	1.3

+: High EPD seed used

++: Flat-top growth

\*: ~3/4 ingot length area

F: front, M: middle, T: tail

Table II. Effect of Cone Angle on Dislocation Density

Ingot No.	Cone Angle*	EPD (cm <sup>-2</sup> )	
		Front	
15	0°	1	$2.4 \times 10^5$
		2	$1.1 \times 10^5$
		3	$2.7 \times 10^5$
4	10°	1	$4.0 \times 10^4$
		2	$1.4 \times 10^5$
		3	$4.0 \times 10^5$
17	25°	1	$1.1 \times 10^4$
		2	$2.0 \times 10^4$
		3	$1.1 \times 10^5$
10	30°	1	$1.1 \times 10^4$
		2	$2.1 \times 10^4$
		3	$1.1 \times 10^5$
6	50°	1	$1.8 \times 10^4$
		2	$2.6 \times 10^4$
		3	$8.0 \times 10^4$
9	62°	1	$1.4 \times 10^4$
		2	$2.0 \times 10^4$
		3	$2.5 \times 10^5$
8	65°	1	$1.4 \times 10^4$
		2	$3.7 \times 10^4$
		3	$1.0 \times 10^5$

\*: Other growth parameters are similar.



Table III. Effect of  $B_2O_3$  Height on Dislocation Density

Ingot No.	Weight of <sup>+</sup> $B_2O_3$	EPD ( $cm^{-2}$ )	
		Front	Tail
13	270 gm	1 $3.5 \times 10^4$	$8.0 \times 10^4$ *
		2 $1.0 \times 10^5$	$1.1 \times 10^5$ *
		3 $1.5 \times 10^5$	$2.0 \times 10^5$ *
16	390 gm	1 $1.3 \times 10^4$	$1.4 \times 10^5$
		2 $2.8 \times 10^4$	$2.2 \times 10^5$
		3 $1.7 \times 10^5$	$2.4 \times 10^5$
12	500 gm	1 $1.2 \times 10^4$	$9.0 \times 10^4$
		2 $1.7 \times 10^4$	$1.0 \times 10^5$
		3 $2.5 \times 10^5$	$2.2 \times 10^5$

+: Other growth parameters are similar.

\*:  $\sim 3/4$  ingot length area.

Table IV. Effect of Ambient Pressure on Dislocation Density

Ingot No.	Ambient* Pressure	EPD (cm <sup>-2</sup> )	
		Front	Tail
14	50 psi Ar	1 $6.0 \times 10^3$	N/A <sup>+</sup>
		2 $1.8 \times 10^4$	
		3 $9.6 \times 10^4$	
16	300 psi Ar	1 $1.3 \times 10^4$	$1.4 \times 10^5$
		2 $2.8 \times 10^4$	$2.2 \times 10^5$
		3 $1.7 \times 10^5$	$2.4 \times 10^5$

\*: Other growth parameters are similar.

+: See text.



Table V. Effects of Seed Quality and Necking on Dislocation Density

Ingot No.	Necking*	Seed	EPD ( $\text{cm}^{-2}$ )		Tail
1	No	High ( $5 \times 10^4$ )	1	$7.6 \times 10^4$	
			2	$4.6 \times 10^4$	
			3	$3.0 \times 10^5$	
5	Yes	High ( $5 \times 10^5$ )	1	$1.5 \times 10^4$	
			2	$3.0 \times 10^4$	
			3	$1.7 \times 10^5$	
9	Yes	Low ( $3.3 \times 10^3$ )	1	$1.4 \times 10^4$	
			2	$2.0 \times 10^4$	
			3	$2.5 \times 10^5$	
16	No	Low ( $4.5 \times 10^3$ )	1	$1.3 \times 10^4$	
			2	$2.8 \times 10^4$	
			3	$1.7 \times 10^5$	

\*: All cone angles  $>25^\circ$  and other growth parameters are similar.

C-2



Table VI. Effects of Melt Stoichiometry and Diameter Control on Dislocation Density

Ingot No.	Initial Melt* Composition	Diameter Variation (mm)	EPD ( $\text{cm}^{-2}$ )	
			Front	Tail
8	53.0% Ga	$\pm 4.0$	1 $1.4 \times 10^4$	N/A
			2 $3.7 \times 10^4$	
			3 $1.0 \times 10^5$	
6	51.5% Ga	$\pm 3.0$	1 $1.8 \times 10^4$	$8.6 \times 10^4$
			2 $2.6 \times 10^4$	$7.7 \times 10^4$
			3 $8.0 \times 10^4$	$2.2 \times 10^5$
9	51.5% Ga	$\pm 7.1$	1 $1.4 \times 10^4$	$1.0 \times 10^5$
			2 $2.0 \times 10^4$	$1.0 \times 10^5$
			3 $2.5 \times 10^5$	$2.4 \times 10^5$
10	50.7% Ga	$\pm 4.5$	1 $1.1 \times 10^4$	N/A
			2 $2.1 \times 10^4$	
			3 $1.1 \times 10^5$	
5	Stoichiometric	$\pm 8.5$	1 $1.5 \times 10^4$	$1.2 \times 10^5$
			2 $3.0 \times 10^4$	$1.4 \times 10^5$
			3 $1.7 \times 10^5$	$2.1 \times 10^5$
12	50.1% As	$\pm 1.6$	1 $1.2 \times 10^4$	$9.0 \times 10^4$
			2 $1.7 \times 10^4$	$1.0 \times 10^5$
			3 $2.5 \times 10^5$	$2.2 \times 10^5$
16	50.3% As	$\pm 1.5$	1 $1.3 \times 10^4$	$1.4 \times 10^5$
			2 $2.8 \times 10^4$	$2.2 \times 10^5$
			3 $1.7 \times 10^5$	$2.4 \times 10^5$
11	50.6% As	$\pm 1.5$	1 $7.5 \times 10^3$	$8.1 \times 10^4$
			2 $1.3 \times 10^4$	$1.8 \times 10^5$
			3 $1.9 \times 10^5$	$1.8 \times 10^5$

\*: All cone angles  $>25^\circ$  and other growth parameters are similar.

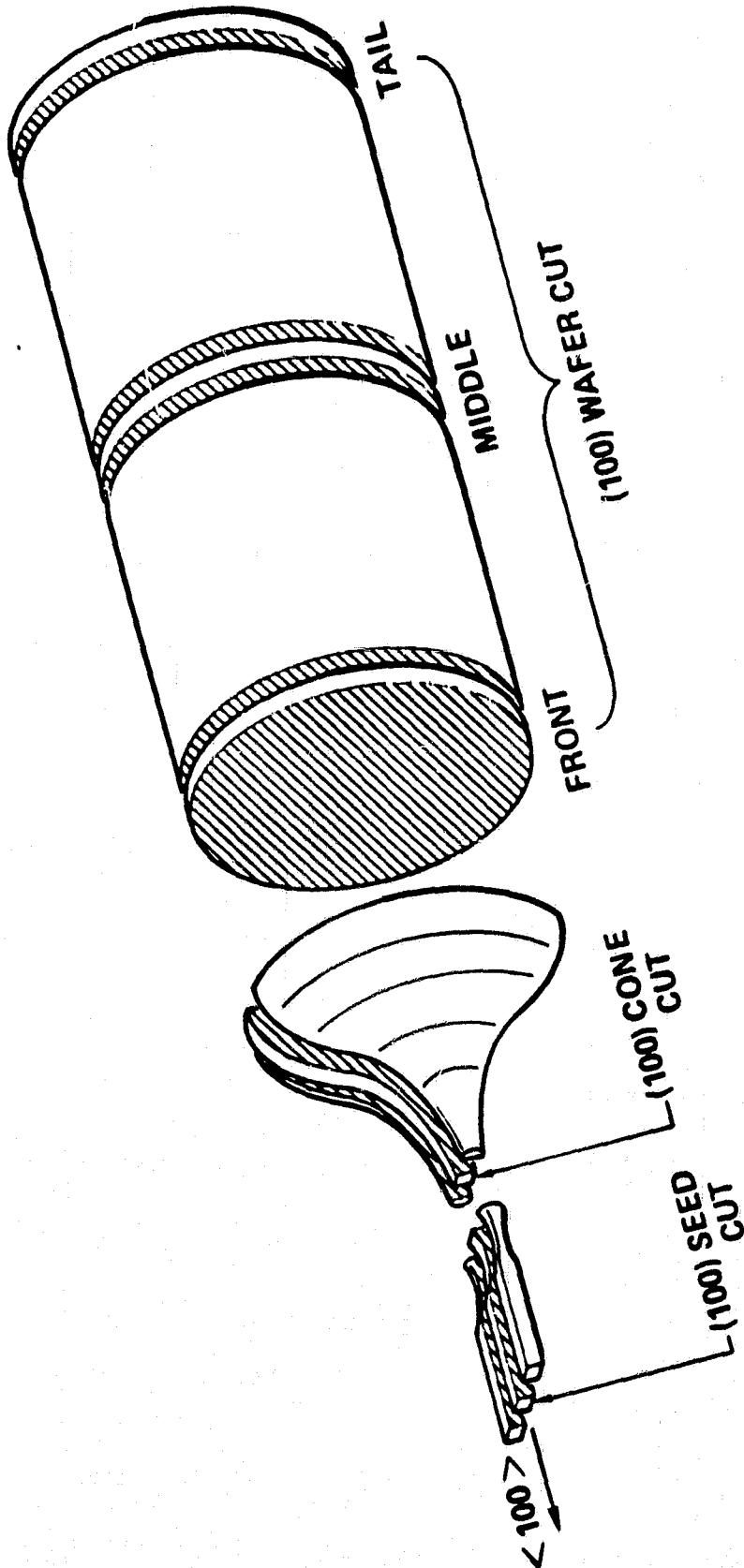




### FIGURE CAPTIONS

- Fig. 1** Slicing diagram for (100) LEC GaAs crystals.
- Fig. 2** Photograph of a KOH-etched (100) GaAs wafer showing the "ring" (Region 1), "center" (Region 2), and "edge" (Region 3) regions, which have the lowest, intermediate, and highest EPD, respectively. The dislocation density has fourfold symmetry indicative of the  $\langle 100 \rangle$  orientation. Also note the lineage polygonization networks along  $\langle 110 \rangle$ , which also have fourfold symmetry.
- Fig. 3** Photomicrograph of KOH-etched wafer quadrant showing microscopic view of dislocation density in regions 1-3. The EPDs in the edge and ring regions are lower along  $\langle 110 \rangle$  than along  $\langle 100 \rangle$ .
- Fig. 4** Radial dislocation density profiles across wafers obtained from the front, middle, and tail of a crystal. The radial profiles are "W"-shaped, and the average EPD increases from the front to the tail.
- Fig. 5** Dislocation maps of longitudinal cross sections of cones with varying cone angles.
- Fig. 6** Dislocation maps of longitudinal cross sections of neck regions with varying neck-diameters: (a) 1.6 mm-diameter neck showing severe deformation; (b) 3 mm-diameter neck showing dramatic EPD reduction.

MRDC81-13004A





ORIGINAL PAGE  
BLACK AND WHITE PHOTOGRAPH

MRDC81-13820A

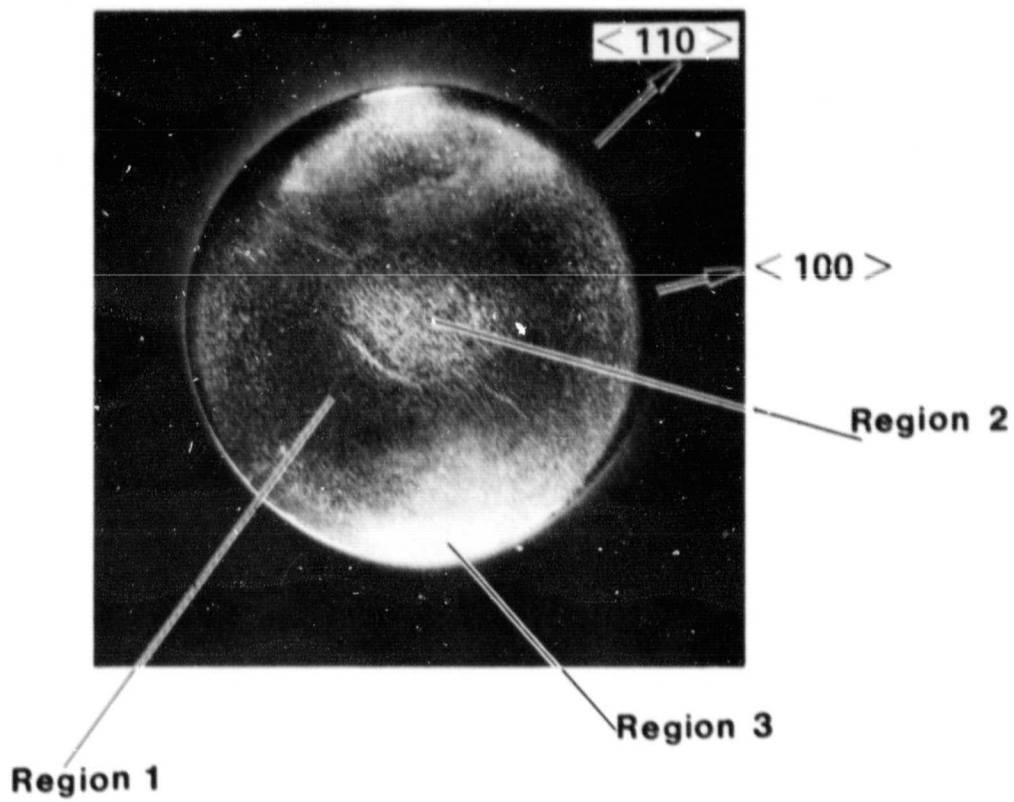


Fig. 2



MRDC82-16276

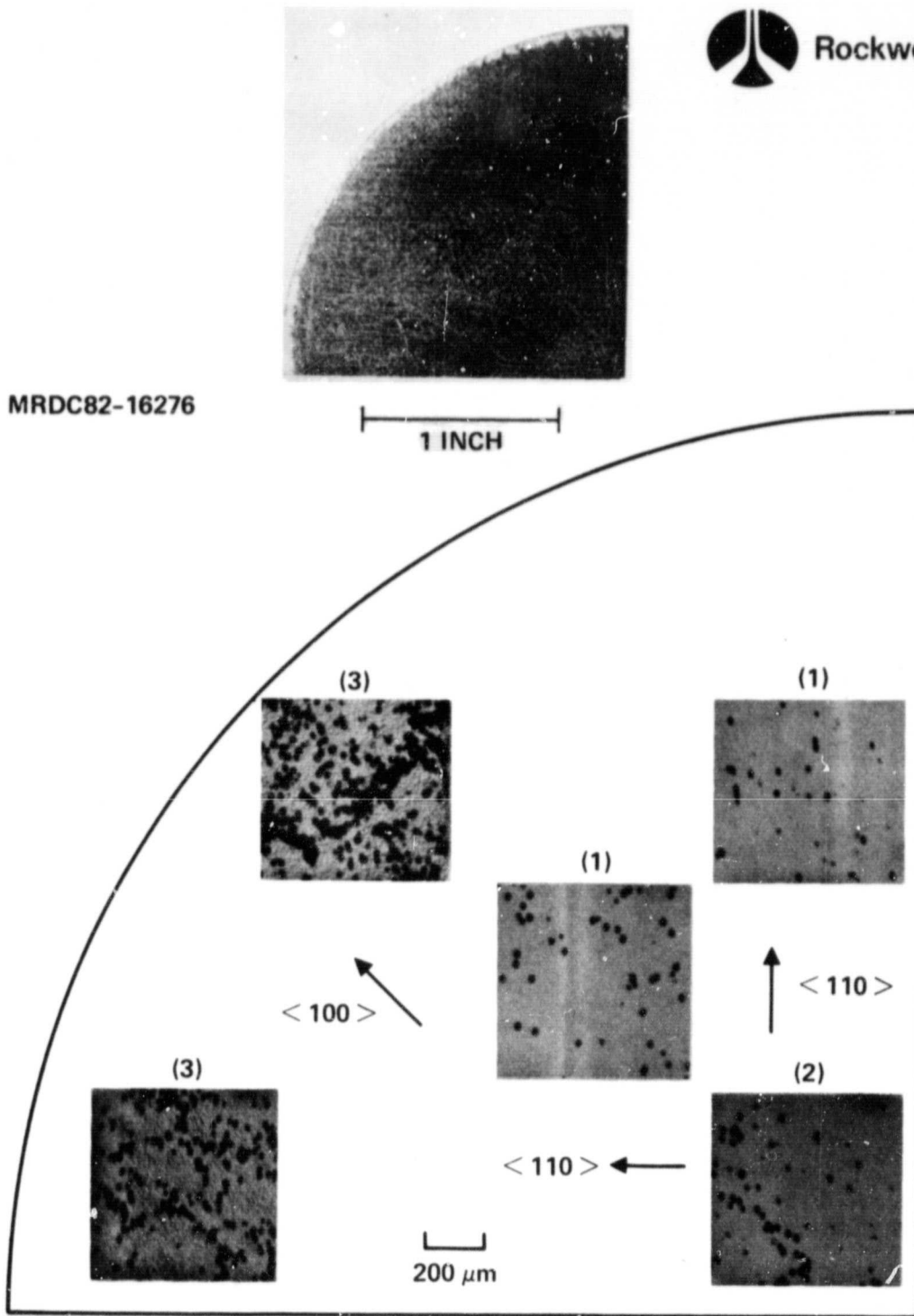
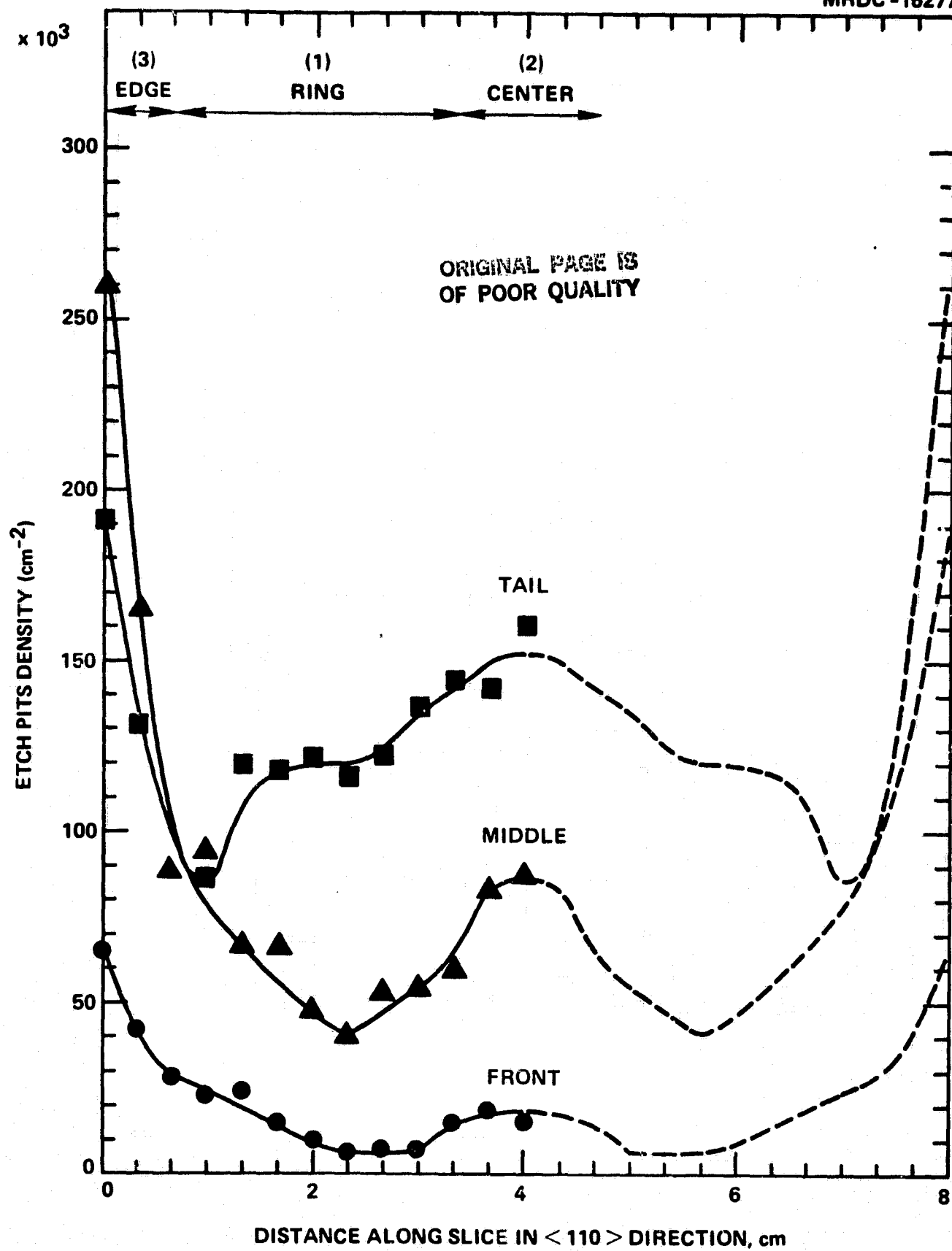


Fig. 3

ORIGINAL PAGE  
BLACK AND WHITE PHOTOGRAPH



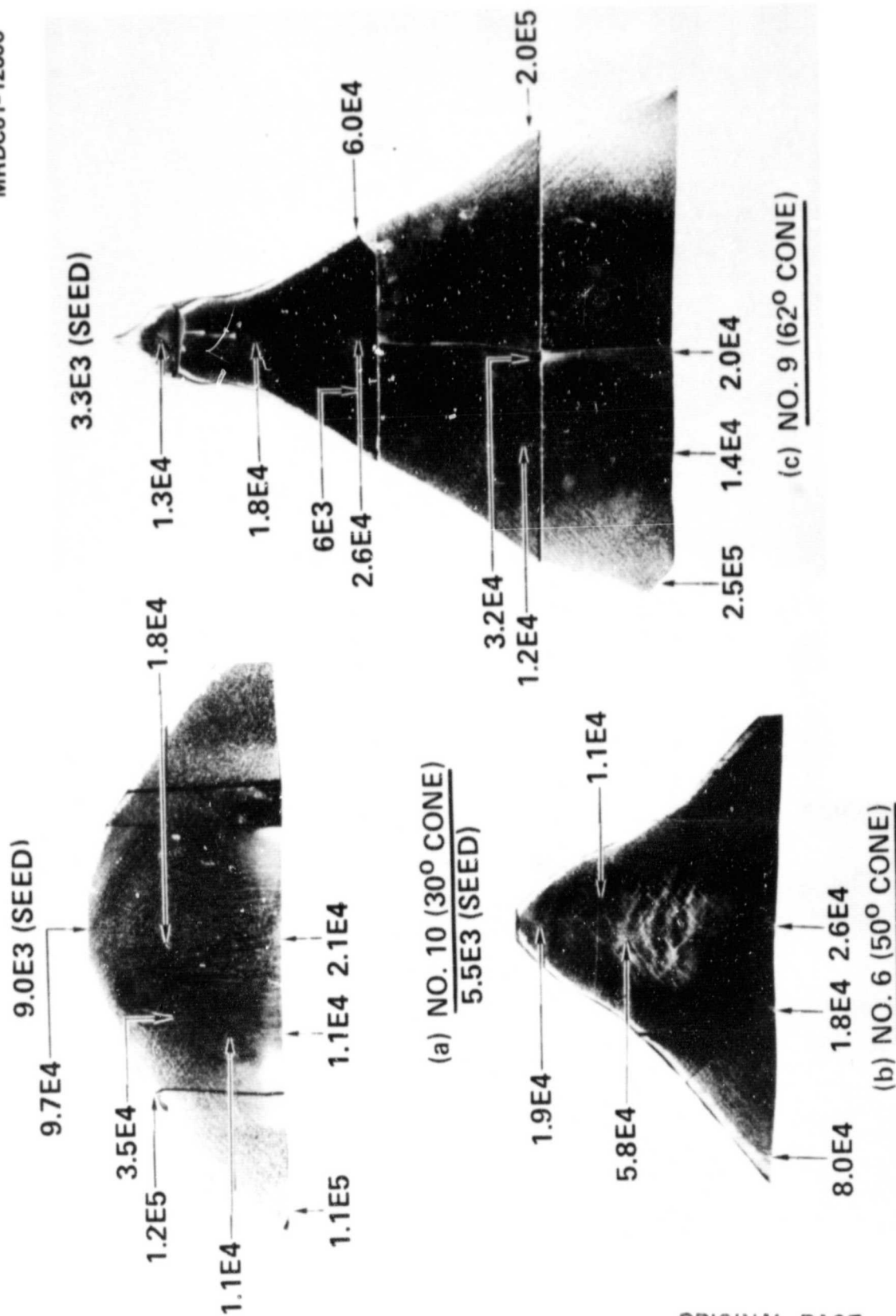


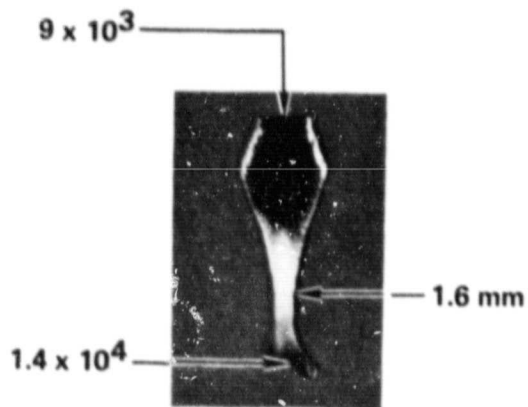
Fig. 5



ORIGINAL PAGE  
BLACK AND WHITE PHOTOGRAPH

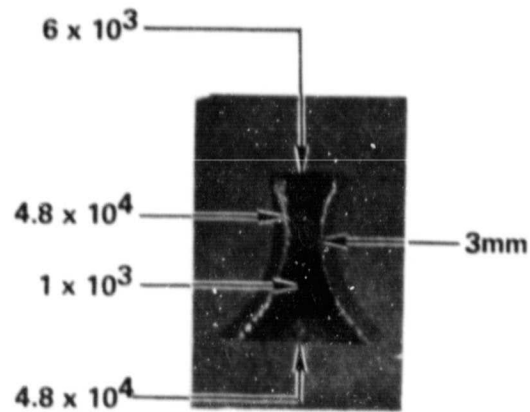
MRDC81-13807A

E.P.D. ( $\text{cm}^{-2}$ )



(a) NO. 10

E.P.D. ( $\text{cm}^{-2}$ )



(b) NO. 12

Fig. 6



**Rockwell International**

#### **9.4 APPENDIX IV**

**To be published in J. of Electrochemical Society**



## EFFECT OF MELT STOICHIOMETRY ON TWIN FORMATION IN LEC GaAs

R. T. Chen and D. E. Holmes

Rockwell International

Microelectronics Research and Development Center

Thousand Oaks, CA 91360

We have found that control over the melt stoichiometry is important to prevent twin formation in large-diameter, undoped,  $\langle 100 \rangle$  GaAs crystals grown by the liquid encapsulated Czochralski (LEC) technique. Twenty GaAs crystals were grown from stoichiometric and non-stoichiometric melts. The incidence of twinning is reduced significantly when crystals are grown under As-rich, near-stoichiometric conditions.

The undoped GaAs crystals used in this study were grown in a high pressure LEC growth apparatus. The pressure of the argon atmosphere during growth was 300 psi. The crystals were grown from pyrolytic boron nitride (PBN) and quartz crucibles. The growth direction was  $\langle 100 \rangle$ . The water content of the  $B_2O_3$  encapsulant (Johnson Matthey) material ranged from 160 to 500 ppm. The weight and diameter of the crystals were typically about 2.4 Kg and 3 in., respectively. The crystals were grown with cone angles varying from 0 to 70°. The cone angle is defined as the angle between the wall of the cone and the horizontal; a crystal with a 0° cone angle is flat-topped.

**Key Words:** *liquid encapsulated Czochralski growth, twinning, melt stoichiometry, gallium arsenide.*



The GaAs melt was prepared by in-situ synthesis (1) starting with a 3 Kg charge of high purity As (Cominco) and Ga (Kawecki). The stoichiometry of each melt was changed by varying the composition of the initial charge. To make an accurate determination of the initial melt composition for crystals grown from PBN crucibles, it was necessary to take into account the loss of As from the charge during the heat-up cycle. We found that the loss of arsenic, which varied from about 10 to 90 g, resulted from incomplete wetting of the  $B_2O_3$  to the PBN crucible before synthesis. The weight loss was determined by comparing the weight of the initial charge with the weight of the crystal and the charge remaining in the crucible after growth. It is important to note that the  $B_2O_3$  was separated from the remaining charge before determining the weight loss. This technique eliminated possible errors associated with the evaporation of  $B_2O_3$  during growth. We emphasize that the presence of excess Ga(or As) in the remaining charge always correlated with the melt stoichiometry calculated on the basis of the weight loss measurements. The composition of the melt at the beginning of growth was effectively varied from 0.46 to 0.51 As atom fraction. The melt composition at the termination of growth was determined by adjusting the initial melt composition for the crystal weight.

We did not determine the stoichiometry of melts synthesized in quartz crucibles. However, in subsequent experiments we found that only from 5 to 20 g of As is typically lost from a stoichiometric 3 Kg charge contained in a quartz crucible during heat-up. Again,  $B_2O_3$  was separated from the GaAs residual charge for these weight loss measurements. In addition, when quartz crucibles were used, we observed relatively small amounts of As deposited on the walls of the growth chamber compared to growth with PBN crucibles, and no

ORIGINAL PAGE IS  
OF POOR QUALITY

excess Ga in the remaining charge. Since stoichiometric charges were always used with quartz crucibles in the present study, we took the initial melt stoichiometry to be slightly Ga-rich with an estimated composition of 0.498 As atom fraction.

The results of our study, summarized in Table 1, show that the incidence of twinning is significantly reduced when crystals are grown from As-rich melts. Only 4 of 12 (33%) crystals grown from Ga-rich melts were single. On the other hand, 7 of 8 (88%) crystals grown from As-rich melts were single. Furthermore, the incidence of twinning could not be correlated with other growth parameters, such as the wetness of the  $B_2O_3(1)$ , the cone angle (see Table 1), or fluctuations in the diameter of the crystal. The results indicate a sharp increase in twinning probability on the Ga-rich side of the stoichiometric composition.

Previous studies (2,3) have shown that the incidence of twinning in small-diameter GaAs crystals can be reduced by growing with gradual cones; i.e., large cone angles. Our results show no correlation between the incidence of twinning and cone angle in large-diameter crystals. Moreover, the significantly reduced incidence of twin formation experienced using As-rich melts in the present study was achieved with small cone angles ranging from 0 to 35°.

Growth experiments employing quartz crucibles were not conducted with As-rich, undoped melts to compare with the results obtained with the Ga-rich melts. However, we have recently grown several crystals doped with Se, Si, and Zn from As-rich melts using quartz crucibles. The incidence of twin formation was very low in this series of experiments (8 out of 9 crystals were single). Our combined results therefore indicate that twin formation is independent of the crucible material.

The twinned crystals were categorized according to the twin morphology. One group was characterized as having only one longitudinal twin, which nucleated at the surface of the crystal and cut the crystal obliquely on a (111) plane. The twinned region of one such crystal was found by x-ray analysis (4) to be oriented with the  $\langle 112 \rangle$  direction parallel to the growth direction. The second group of crystals contained multiple twins. Twins in all crystals invariably nucleated at one of the four peripheral facets that run axially along the crystals. (The peripheral facets result from the intersection of (111) As and (111) Ga facet planes with the edge of the crystal along  $\langle 110 \rangle$  directions that are perpendicular to the  $\langle 100 \rangle$  growth axis). No preference was observed for either As or Ga peripheral facets as nucleation sites for twins.

The reduced incidence of twin formation in As-rich melts has been reported for GaAs grown by the Bridgman (5) and modified Gremmelmaier (2) techniques. The consistent effect of melt stoichiometry on twin formation in GaAs grown by three different techniques may therefore reflect fundamental behavior of the material. The dramatic variation in the incidence of twinning over a relatively small range of melt compositions observed in the present study suggests that the stoichiometry of the solid at the growth interface could play an important role. Thus, the variable resistance of the crystal to twin formation could be related to different solidification kinetics depending on whether vacancies, interstitials, or antisite defects incorporate into the solid.

In summary, we have shown that the incidence of twin formation in large-diameter, undoped,  $\langle 100 \rangle$  LEC GaAs is reduced when the melt composition is slightly As-rich. In view of the potential for the loss of As from the charge



when using in-situ synthesis, the yield of single  $\langle 100 \rangle$  crystals will depend on close control of the melt composition. Finally, the results suggest that the barrier to twin formation is related to the stoichiometry of the solid at the solidification front.

#### ACKNOWLEDGEMENTS

The authors are grateful to the National Aeronautics and Space Administration and the Army for partial financial support of this work under Contract NAS3-22224. The authors would also like to thank J. K. Dreon for his help in growing the crystals and to Dr. C. G. Kirkpatrick for her encouragement during the course of this study.

#### REFERENCES

1. T. R. AuCoin, R. L. Ross, M. J. Wade and R. O. Savage, Solid State Technology, 22, 59 (1979).
2. A. Steinemann and V. Zimmerli, Solid-State Electron. 6, 597 (1963).
3. W. A. Bonner, Mat. Res. Bull. 16, 63 (1980).
4. M. D. Lind, private communication.
5. L. R. Weisberg, J. Blanc and E. J. Stofko, J. Electrochem. Soc. 109, 642 (1962).



Table 1  
Incidence of Twinning in Large-Diameter (100)  
LEC GaAs Crystals\*

Crystal No.	Crucible Material	Melt Stoichiometry	Melt Composition, As Initial	Atom Fraction* Final	Result	Cone Angle†	Twin Morphology††
1	PBN	Ga-rich	0.462	0.445	Twin	65°	M
2	"	"	0.477	0.459	Twin	30°	M
3	"	"	0.486	0.439	Twin	60°	M
4	"	"	0.488	0.434	Single	60°	
5	"	"	0.489	0.439	Single	50°	
6	"	"	0.492	0.457	Twin	30°	1L
7	"	"	-	-	Twin	40°	M
8	Quartz	"		**	Twin	20°	M
9	"	"		**	Single	70°	
10	"	"		**	Twin	10°	M
11	"	"		**	Twin	50°	M
12	"	"		**	Single	65°	
13	PBN	As-rich	0.500	0.500	Single	30°	
14	"	"	0.500	0.500	Single	25°	
15	"	"	0.500	0.501	Single	30°	
16	"	"	0.501	0.508	Single	30°	
17	"	"	0.502	0.512	Single	30°	
18	"	"	0.502	0.509	Single	0°	
19	"	"	0.504	0.534	Twin	35°	1L
20	"	"	0.506	0.536	Single	30°	

\*160-500 ppm H<sub>2</sub>O in B<sub>2</sub>O<sub>3</sub>

†The angle between the wall of the cone and the horizontal, e.g., a 0° cone refers to a "flat-top" cone.

††M-multiple twins, 1L - one longitudinal twin.  
\*Calculated melt composition corresponding to the growth of the front (initial) and tail (final) of the crystal.

\*\*See text.